Molecular Self-Assembly and Chiral Recognition of Malic Acid on a Cu(110) Surface

---

Dissertation

zur

Erlangung der naturwissenschaftlichen Doktorwürde
(Dr. sc. nat.)

vorgelegt der

Mathematisch-naturwissenschaftlichen Fakultät

der

Universität Zürich

von

Christian A. Roth

von

Fahrni BE

Promotionskomitee

Prof. Dr. Karl-Heinz Ernst (Vorsitz)

Prof. Dr. Kim K. Baldrige

Prof. Dr. Jürg Osterwalder

Prof. Dr. Jay S. Siegel

Zürich, 2011

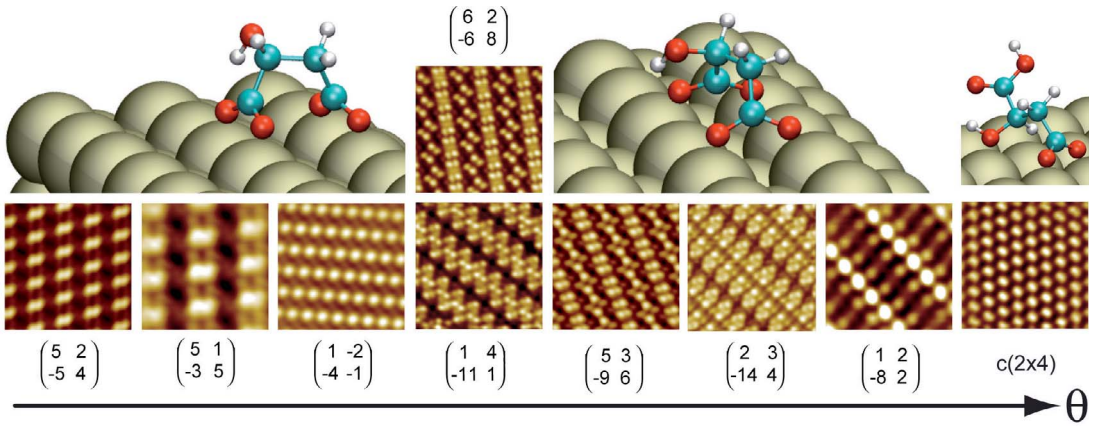
(6 2 / -6 8)
(5 2 / -5 4)
(5 1 / -3 5)
(1 -2 / -4 -1)
(1 4 / -11 1)
(5 3 / -9 6)
(2 3 / -14 4)
(1 2 / -8 2)
c(2x4)
θ

Acknowledgement

First, I want to thank Prof. Karl-Heinz Ernst for giving me the opportunity to do my dissertation in a very interesting field and in a really nice group. I also want to thank Dr. Manfred Parschau for advising on questions concerning the work under UHV conditions. Tobias Bauert, Quang Thai and Dr. Andrew Norris were extremely agreeable office-mates. I think we had a great and funny time. Next, I want to express my gratitude to Günther Hobi for electronic, electrical and IT support.

The set-up of the UHV-RAIRS chamber would not have been possible without drawings made by Sasa Vranjkovic. Thank you very much for this drawings and also for help during the assembly of the chamber. Sigfried Roos ordered a lot of parts for the RAIRS system. Thus I did not have to fight with SAP. I and also my nerves want to thank him for this. But a lot of components within this system have also been constructed in the awesome Empa workshop. Representative for the workshop I would like to thank Erwin Pieper for all the parts created to make the RAIRS chamber working.

Dr. Davide Ferri helped me a lot in analyzing RAIRS spectra. I am indebted to him for his great ideas and suggestions concerning the system malic acid on Cu(110).

I want to thank Dr. Daniele Passerone for theoretical support in explaining molecular recognition between malic acid and tartaric acid, as well as for the structure calculations of single malic acid molecules on Cu(110).

Francisco Alvarez is always busy with keeping the rotary and membrane pumps alive and sometimes he even has to reanimate them. For this important work I want to express my gratitude.

A general thank goes to the complete Abt. 125. I had a great time in this very nice department.

Last, but certainly not least, I want to express my deepest gratitude to my family and friends for all the help and support.

Contents

Summary

The adsorption and two-dimensional self assembly of enantiopure and racemic malic acid (MA) on Cu(110) has been studied in ultra-high vacuum (UHV) with temperature programmed desorption (TPD), low energy electron diffraction (LEED), UV- and X-ray photoelectron spectroscopy (UPS, XPS), as well as scanning tunneling microscopy (STM). In order to get detailed informations on the chemical structure of the adsorbate complex, the first UHV surface infrared spectrometer (reflection-absorption infrared spectroscopy, RAIRS) in Switzerland has been installed. Depending on the coverage and the deposition conditions, eleven ordered structures of (*R*)- and (*S*)-MA were observed with LEED and STM. As previously reported for tartaric acid on this surface, MA shows two adsorbate modes in which either one (monomalate) or both carboxyl groups (bimalate) react with the surface under deprotonation. The high-coverage monolayer shows "surface explosion", a rapid decomposition phenomenon observed in TPD. As observed in STM the two-dimensionally ordered bimalate structures show features which are interpreted as reconstruction of the underlying Cu surface. This is the first direct STM observation of adsorption-induced reconstruction on Cu(110) for butanedioic acids and suggests that a pronounced chirality transfer via the substrate, rather than by intermolecular hydrogen bonding, occurs.

Racemic MA shows ordered structures that have not been observed for the pure enantiomers. Our structure models consider therefore heterochiral pairs as building blocks. Surface reconstructions have been observed directly. Only at full monolayer coverage a well ordered c(2×4) phase covers the entire crystal surface. All other structures are only observed in small patches. The racemic c(2×4) shows an even better order than the enantiopure counterpart, indicating again a heterochiral arrangement of monomalate molecules.

We also investigated the effect of chiral conflict, that is, mixing of tartaric acid (TA) and malic acid (MA). Racemic TA shows a superposition of the two enantiomorphs in LEED that are observed for the pure TA enantiomers. Adding one enantiomer of MA at a concentration of 25-75% suppresses formation of one enantiomorph. (*R*)-MA allows thereby only the formation of the structure known for pure (*R,R*)-TA, while (*S*)-MA leads to the (*S,S*)-enantiomorph. The suppressed enantiomorph forms quasi-racemic semi-ordered phases. Among other structure motifs, triplets of molecules have been identified in these regions. DFT calculations showed the most stable triplet to be formed from two MA molecules and one TA molecule. As driving force, strong lateral interactions via hydrogen bonding has been identified.

The reverse mixing experiment, namely, *rac.*-MA mixed with enantiopure TA shows again induction of single enantiomorphism. A prolonged annealing time at elevated temperature needed to observe this effect is an indication for a large mass transport. This amplification effect is explained by breaking the balance of heterochiral trimer formation in *rac.*-MA.

Zusammenfassung

Die Adsorption und die zwei-dimensionale Selbstanordnung von enantioreiner und razemischer Äpfelsäure auf Cu(110) wurde im Ultrahochvakuum mittels Temperatur-Programmierter Desorption, Niederenergie-Elektronenbeugung, Ultraviolett- und Röntgen-Photoelektronen Spektroskopie, sowie Rastertunnelmikroskopie untersucht. Um detaillierte Informationen bezüglich der chemischem Struktur von Adsorbaten zu erlangen, wurde ein ans Ultrahochvakuum angepasstes Oberflächen Infrarot Spektrometer aufgebaut. In Abhängigkeit von der Bedeckung und den Aufdampfbedingungen konnten für die beiden Enantiomere der Äpfelsäure insgesamt elf geordnete Strukturen mittels Niederenergie-Elektronenbeugung und Rastertunnelmikroskopie beobachtet werden. Wie schon für Weinsäure auf Cu(110) berichtet, gibt es auch für Äpfelsäure zwei Möglichkeiten zur Adsorption: Entweder reagiert nur eine oder beide Carboxylgruppe(n) unter Abspaltung eines Wasserstoffatoms mit der Oberfläche. Bei hoher Bedeckung findet in der Temperatur-Programmierten Desorption ein schneller Zersetzungsprozess ("Oberflächenexplosion") statt. Mit dem Rastertunnelmikroskop konnten für die zweifach deprotonierte Äpfelsäure Merkmale einer Rekonstruktion der Kupferoberfläche festgestellt werden. Das ist das erste Mal, dass für Bicarbonsäuren eine solche Adsorbat-induzierte Rekonstruktion der Cu(110) Oberfläche beobachtet wurde. Demnach erfolgt der Chiralitätstransfer eher durch das Substrat, als durch zwischenmolekulare Wasserstoffbrückenbindungen.

Razemische Äpfelsäure ordnet sich in Strukturen, welche für das enantioreine Molekül nicht beobachtet wurden. Deshalb werden in den Strukturmodellen heterochirale Paare als Baustein angenommen. Oberflächenrekonstruktionen konnten auch für das Razemat direkt festgestellt werden. Bei voller Monolage bedeckt eine gut geordnete c(2×4) Phase die gesamte Kristalloberfläche. Alle anderen Strukturen erscheinen in eher kleinen Domänen. Die razemische c(2×4) Struktur ist besser geordnet als das enantioreine Gegenstück, weshalb auch hier eine heterochirale Anordnung der einfach deprotonierten Äpfelsäure Moleküle vermutet wird.

Der Effekt des chiralen Konflikts wurde im Mischungsexperiment mit Weinsäure und Äpfelsäure untersucht. Razemische Weinsäure zeigt in der Niederenergie-Elektronenbeugung eine Struktur, welche der Superposition der für die beiden enantioreinen Weinsäuren detektierten Strukturen entspricht. Wird ein Äpfelsäureenantiomer mit einer Konzentration von 25-75% zugegeben, so kann sich eine der Weinsäurestrukturen nicht mehr formieren. Rechtshändige Äpfelsäure erlaubt nur die Ausbildung der Struktur von rechtshändiger Weinsäure, wohingegen linkshändige Äpfelsäure nur die Formierung der Struktur linkshändiger Weinsäure zulässt. Das unterdrückte Enantiomorph bildet eine quasi-razemische, halb-geordnete Phase. Zusammen mit anderen Strukturmotiven wurden in diesen Regionen Tripletts von Molekülen identifiziert. Berechnungen mittels Dichtefunktionaltheorie ergaben, dass das stabilste Triplett aus zwei Äpfelsäuremolekülen und einem Weinsäuremolekül besteht. Starke laterale Wechselwirkungen via Wasserstoffbrückenbindungen sind für die Ausbildung dieser Tripletts verantwortlich.

Das umgekehrte Mischexperiment mit razemischer Äpfelsäure und enantioreiner Weinsäure resultiert ebenfalls in der Ausbildung nur eines Enantiomorphs. Für diesen verstärkten Effekt war ein zeitlich ausgedehntes Heizen bei hoher Temperatur notwendig, was als Indiz für einen ausgeprägten Transport von Masse angesehen werden kann. Eine Zerstörung des Bildungs-

gleichgewichts von heterochiralen Trimeren in racemischer Äpfelsäure wird zur Erklärung herangezogen.

Chapter 1

Introduction

1.1 Chirality

The term chirality was introduced in 1884 by Lord Kelvin and stems from the Greek word for hand, $\chi\epsilon\iota\rho$ (cheir), since hands are chiral. Lord Kelvin stated in his lectures in Baltimore on Molecular Dynamics and the Wave Theory of Light: "I call any geometrical figure, or group of points, chiral, and say it has chirality, if its image in a plane mirror, ideally realized, can not be brought to coincide with itself" [1]. The first time chirality came on stage was in 1848 when L. Pasteur separated left- and right-handed ammonium sodium tartrate crystals manually and observed opposite optical activity for their aqueous solutions [2]. In 1874 J. H. van 't Hoff [3] and J. A. Le Bel [4] suggested the tetrahedral arrangement of atoms bound to carbon. Whenever a molecule has a carbon atom with four different substitutes, then this carbon atom is a chiral center and the molecule itself is chiral as depicted in figure 1.1 for alanine. Original and mirrored molecules are called enantiomers. They are optical isomers since plane polarized light is rotated in opposite directions. Apart from the interaction with plane polarized light, opposite enantiomers do not differ in any physical property, i.e. they have the same boiling points, melting points and densities. On the other hand they may have different chemical behaviours and different aroma and flavors. However, the probably most important difference between enantiomers is due to biological activity. A good example is penicillamine. *D*-penicillamine is used as a medicine for rheumatism. The opposite handed *L*-enantiomer is poisonous. Hence, the enantiomeric purity of a chiral compound in pharmaceutical products is of paramount importance. Opposite enantiomers are distinguished by means of the rules stated by Cahn, Ingold and Prelog [5], which allow to label the absolute configuration of a chiral center as *R* (for rectus) or *S* (for sinister).

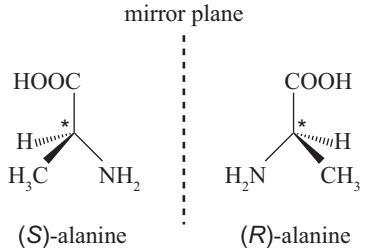

Figure 1.1: The chiral centers of the alanine enantiomers are indicated by an asterisk.

Chirality is a general phenomenon in natural sciences: All proteins are for instance constructed from *L*-amino acids and DNA contains only *D*-sugars. This is called biomolecular homochirality [6–8]. Another interesting aspect of chirality in biology is chiral biomineralization, causing achiral

minerals to adopt chiral shapes [9,10]. In nuclear physics, the neutral and charged currents in the weak interaction have been shown to break parity, as the neutrino is only left-handed [11]. The absolute spatial arrangement of atoms in molecules is the manifestation of stereochemistry, and enantioselective synthesis with chiral catalysts is of paramount importance for the production of a chiral compound with enantiomeric purity.

1.2 Enantioselective catalysis

A growing demand for enantiomerically pure products in pharmacy, agrochemical industry and in the field of fragrances and flavors directed interest towards enantioselective catalysis. This increased importance is reflected in the Nobel Prize for chemistry in 2001, awarded to Knowles, Noyori and Sharpless for "their work on chirally catalyzed reactions" [12]. The importance of catalysis in general and the approach to study model systems is underlined by the Nobel Prize for chemistry in 2007, which was awarded to Gerhard Ertl for "his studies of chemical processes on solid surfaces" [13]. In a model system the active catalyst is replaced by a single crystal surface, and the molecules are adsorbed on these surfaces under ultra high vacuum conditions (UHV, pressure in chamber $\leq 10^{-9} mbar$). At this low pressure a freshly prepared sample will stay clean for at least one hour. At higher pressures the contamination of the sample would occur at a higher rate and thus not allow a thorough characterization.

Enantiopure products for pharmaceutical industry are mainly produced by means of homogeneous catalysts [14]. However, enantioselective heterogeneous catalysis has been successfully applied for the hydrogenation of α- and β-ketoesters. Heterogeneous catalysts are sustainable due to ease of separation, handling, recovery and higher potential for regeneration and re-use.

Modification is the crucial step in conferring enantioselectivity onto a catalyst. Basically two heterogeneous catalytic systems are in use. The Ni-based catalyst modified with tartaric acid (TA) has been proven to be enantioselective for hydrogenation of β-ketoesters [15, 16]. This is shown for methylacetoacetate (MAA) in figure 1.2.

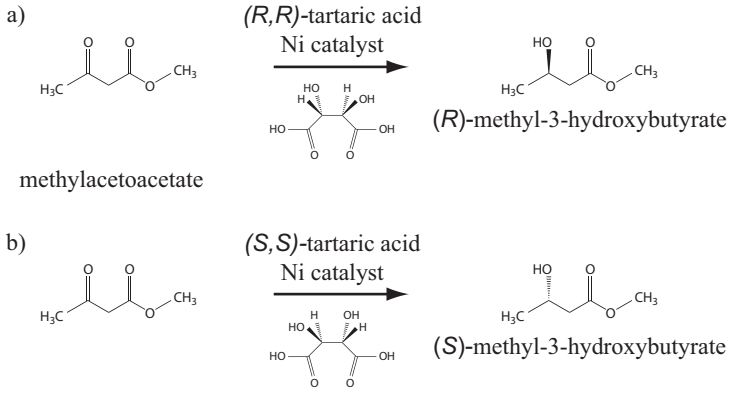

Figure 1.2: Methylacetoacetate is enantioselectively hydrogenated over Ni modified with tartaric acid.

For the enantioselective hydrogenation of α-ketoester to α-hydroxyester over Pt catalysts the cinchona alkaloids cinchonidine and cinchonine are used as modifiers (Figure 1.3). Under optimized conditions an enantiomeric excess of 95% can be reached [17].

Although cinchonidine and cinchonine are not enantiomers of each other, the hydrogenated products have opposite handedness. Thus the hydrogenation of methyl pyruvate results in (R)-methyl lactate if cinchonidine is taken as modifier, but (S)-methyl lactate is formed with cin-

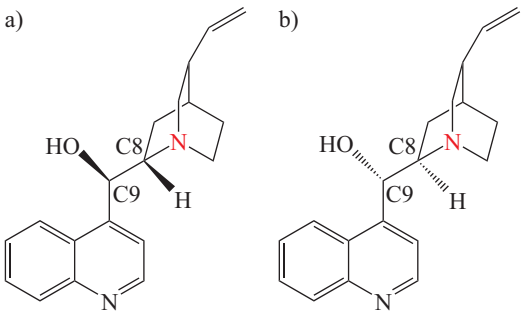

Figure 1.3: The cinchona alkaloids cinchonidine in a) and cinchonine (b) are shown. The nitrogen atom in the quinuclidine ring (red) plays an important role in the enantio-differentiation.

chonine (Figure 1.4) [18, 19]. In addition, modification with the alkaloid enhances the reaction rate [16, 17, 20, 21].

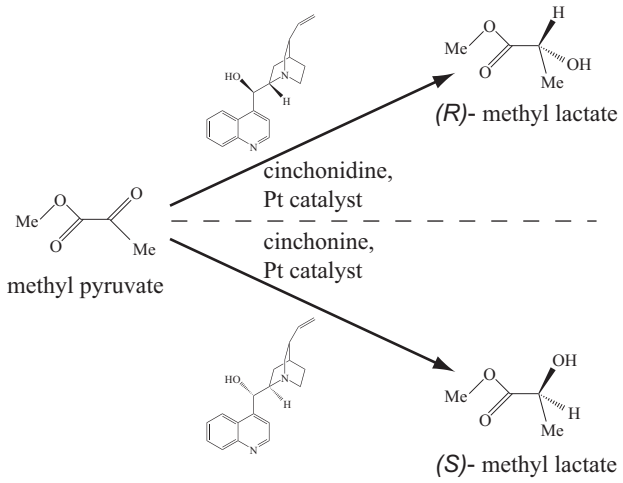

Figure 1.4: Cinchonidine as modifier gives (R)-methyl lactate, cinchonine gives the (S)-enantiomer.

Several models try to explain the observed effects [16, 18, 22, 23]. The template model is based on the assumption that the chiral modifier forms a 2D chiral array on the catalyst surface. Thereby 2D chiral channels are also constituted, in which the prochiral reactant molecules can adsorb and where the hydrogenation should take place. Since these channels are chiral the reactant molecules must dock in a specific way to the modifier molecules and thus the chirality of the product is determined. A modifier with opposite handedness would result in channels into opposite direction and hence the product molecules would have opposite chirality.

The organo-metallic complex model proposed by Sachtler et al. [22] assumes that both a Ni-tartrate complex and the Ni metal are essential for the hydrogenation. The Ni atom in the complex is the enantioselective site. This model is supported by the fact that Ni is leached out during the modification process.

In the 1:1 interaction model a modifier molecule and a reactant molecule interact directly to result in a hydrogenated product with specific chirality. Crucial for the product handedness in the hydrogenation of α-ketoester is the chirality of the stereogenic region (C8 and C9 in figure 1.3) of the cinchona alkaloids. The enantioselectivity is lost when the quinuclidine nitrogen is alkylated.

Therefore it must be involved in the interaction complex that leads to enantio-differentiation [24].

An interesting suggestion by Attard also explains the enantioselective hydrogenation. He pointed out that a real catalyst should more correctly be referred to as a racemate containing equal numbers of R and S kink sites. A preferential adsorption of the modifier changes the proportion of R and S kinks and thus explains enantioselectivity [25].

Up to date the mechanism of heterogeneous enantioselective catalysis is not known.

1.3 Chiral surfaces

1.3.1 Naturally occurring chiral surfaces

Some naturally occurring materials such as quartz, silk or wool are chiral. Consequently also the surfaces of such materials should be chiral and sometimes the chirality finds its expression even in the macroscopic morphology (Figure 1.5).

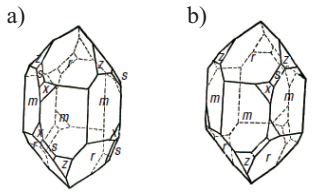

Figure 1.5: Left- and right-handed quartz crystals are shown in a) or b) respectively. The handedness depends on the orientation of structural helices and is also expressed in the external morphology [26].

The adsorption of (*D*)- and (*L*)-alanine was found to be asymmetric on quartz. *d*-quartz preferentially adsorbed (*D*)-alanine and *l*-quartz preferentially adsorbed (*L*)-alanine [27]. Naturally chiral materials can act as support in enantioselective catalysis. Cu, Ni and Pt as active catalyst together with optically active quartz showed to a small extent enantiospecific dehydration and oxidation of racemic secondary butyl alcohol [28, 29]. Jiang et al. used a wool-Pd complex for the asymmetric hydrogenation of diacetone alcohol to (*R*)-2-methyl-2,4-pentanediol and 3-methyl-2-butanone to (*R*)-3-methyl-2-butanol at only 303K. The optical yield was fairly high (73% and 100%) [30].

1.3.2 Chiral metal surfaces

McFadden et al. were the first ones to point out that an intrinsically chiral surface can be produced just by cutting a single crystal [29, 31]. Thus a surface exposing a high Miller index plain can be created. Such a surface consists of chiral kinks and low Miller index terraces. Later it was noted that any fcc(hkl) surface with no zero indices ($h \cdot k \cdot l \neq 0$) and no equal indices ($h \neq k$, $h \neq l$, $l \neq k$) is intrinsically chiral [32] (Figure 1.6).

The interaction of the chiral alcohols (*R*)-2-butanol and (*S*)-2-butanol with Ag(643) and Ag($\overline{643}$) was studied in temperature programed desorption experiments (TPD). However, no enantiospecific difference could be observed [31]. This result was attributed to the experimental resolution. Sholl et al. simulated the adsorption of chiral hydrocarbons on chiral Pt surfaces. They could show that the system chiral adsorbate/chiral surface must be chosen carefully in order to achieve enantiospecific adsorption [32]. Indeed, a diastereomeric effect in molecular desorption of a chiral molecule from a naturally chiral single crystal surface could be shown by adsorbing (*R*)- and (*S*)-propylene oxide on Cu(643) and Cu($\overline{643}$), as well as in the system (*R*)-3-methylcyclohexanone adsorbed on Cu(643) and Cu($\overline{643}$) [33–35].

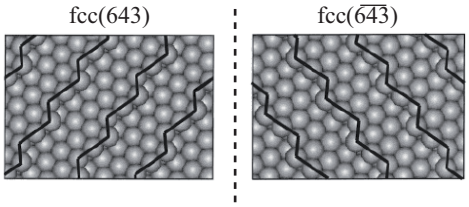

Figure 1.6: A fcc(643) and the mirrored surface fcc($\overline{643}$). Both surfaces consist of low Miller index (111) terraces and chiral kinks with opposite handedness [32].

Attard et al. investigated the electro-oxidation of (*D*)- and (*L*)-glucose using the chiral electrode Pt(643) and its enantiomorph Pt($\overline{643}$). Cyclic voltammetry revealed an enantiospecificity ascribed to the chiral kinks on the Pt electrodes. On the other hand no difference could be detected for oxidation on the achiral Pt(211) and Pt(332) electrodes. Comparison with electro-oxidation on Pt(531) showed chiral discrimination to scale with the surface density of kink sites [36]. In a later study the electro-oxidation of (*D*)- and (*L*)-glucose on Pt(431) and Pt($\overline{431}$) was investigated. Apart from this, voltammograms were also recorded for both enantiomers of mannose on Pt(321) and Pt($\overline{321}$) as well as for (*D*)- and (*L*)-arabinose on both Pt(643) electrodes. All of these systems showed enantiospecificity [25].

1.3.3 Chiral surfaces by adsorption of chiral molecules

Achiral surfaces can be endowed with chirality simply by adsorbing chiral molecules. Chirality in general can be expressed either as point chirality (point groups) or as organizational chirality (space groups in 3D or plane groups in 2D respectively). In 2D there exist the five chiral point groups and five chiral plane groups represented in figure 1.7 [37]. A chiral molecule adsorbs on an achiral surface always only in a single-handed motif. The chiral motif with opposite handedness can not be observed and consequently chiral chains, clusters and arrays also exist only in one chiral form. The situation is different when the adsorbed molecule is prochiral, i.e. forms a chiral adsobate only due to confinement at the surface.. In this case a molecule will adsorb with equal probability in either of the two possible chiral configurations. In that case left- and right-handed structures are formed always with equal probability and the global structure is achiral (Figure 1.8).

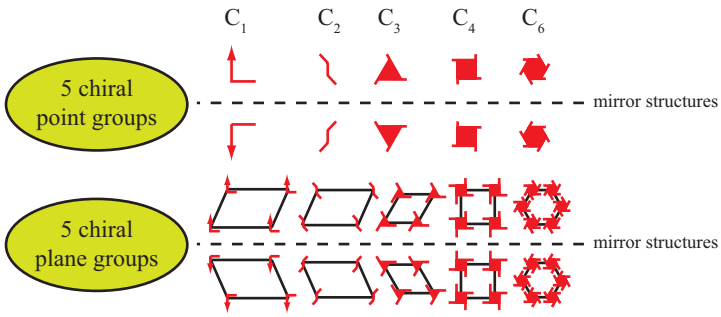

Figure 1.7: The five 2D chiral point and plane groups are shown. The rotation symmetry is indicated, e.g. C_2 is equal to a 180° symmetry.

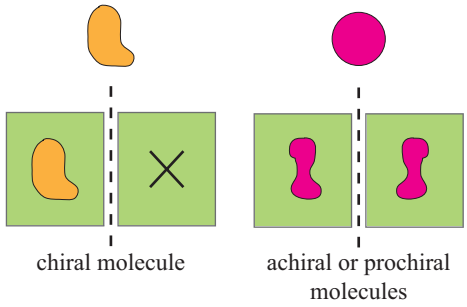

Figure 1.8: A chiral molecule is still chiral after adsorption on an achiral surface and the chirality is expressed in a certain adsorption motif. The adsorption motif with opposite handedness is not formed. A prochiral molecule forms both mirror adsorption motifs.

1.4 Butanedioic acids on Cu(110)

Chiral surface science is a vastly growing field nowadays and we introduce here only butanedioic acids on Cu(110) in detail. For other systems review articles are recommended [37–42].

1.4.1 Notation of overlayer structures

For the classification of overlayer structures either the Wood or the matrix notation is used [43]. The Wood notation gives the relation between the overlayer lattice structure (basis $\vec{b}_1$ and $\vec{b}_2$) and the substrate lattice (basis $\vec{a}_1$ and $\vec{a}_2$) by the ratios of the lengths of the basis vectors plus any angle of rotation ϑ between these two lattices. The Wood notation fails whenever overlayer and substrate structure have no common periodicity.

In the matrix notation the substrate unit cell vectors $\vec{a}_1$ and $\vec{a}_2$ and the unit cell vectors of the overlayer $\vec{b}_1$ and $\vec{b}_2$ are related by a matrix M as follows (Figure 1.9):

$$\vec{b}_1 = m_{11}\vec{a}_1 + m_{12}\vec{a}_2$$
$$\vec{b}_2 = m_{21}\vec{a}_1 + m_{22}\vec{a}_2$$

Thus the matrix M is given by

$$\begin{pmatrix} m_{11} & m_{12} \\ m_{21} & m_{22} \end{pmatrix}$$

Matrix M can also be written as (m_{11} m_{12}; m_{21} m_{22}). The choice of the unit cells of substrate and adsorbate lattice has been somewhat ambiguous until recently new strict rules were established [44].

1.4.2 Adsorption on Cu(110)

The adsorption of butanedioic acids like tartaric acid (TA), *meso*-tartaric acid ((*S*,*R*)-TA) and succinic acid (SU) (Figure 1.10) on Cu(110) was previously investigated and we will compare briefly the results.

1.4.3 TA on Cu(110)

All butanedioic acids adsorb on Cu(110) basically in two different adsorbate modes. Either only one carboxyl group is deprotonated (monocarboxylate) or both carboxyl groups are deprotonated

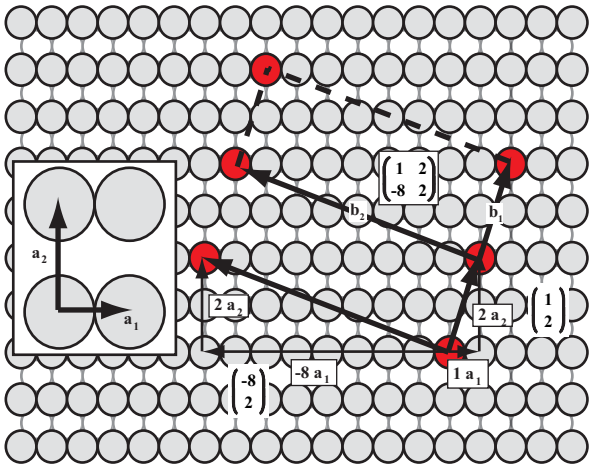

Figure 1.9: Sketch for finding the matrix that connects the overlayer periodicity (red atoms) with the substrate periodicity. In the inset the choice of the substrate vectors is shown.

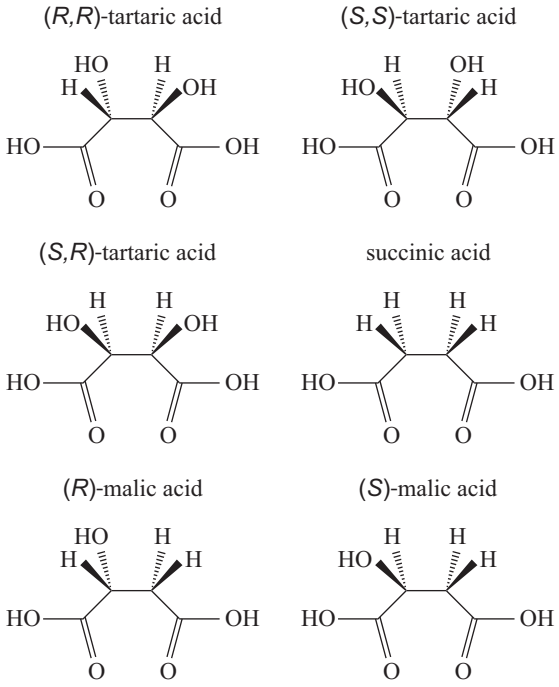

Figure 1.10: Structural formulas of various butanedioic acids. Chiral (*R*,*R*)-TA, (*S*,*S*)-TA as well as (*R*)-MA, (*S*)-MA, achiral (*S*,*R*)-TA and SU.

(bicarboxylate, Figure 1.11). A complicated phase diagram has also been reported for the enantiopure TA/Cu(110) system [45–47]. In the various ordered overlayers adsorbate modes and orientation vary with coverage and temperature. The most prominent structures observed for (*R,R*)-TA on Cu(110) are the chiral (9 0, 1 2) ((*S,S*)-TA forms a opposite handed (9 0, −1 2), [48]) and the achiral (4 0, 2 1) (c(2 × 4) in Wood notation) structures represented in figure 1.12. We call an ordered overlayer chiral, when there is no mirror plane in the lattice, no matter if the basis is chiral or not. Consequently, an achiral or symmetric structure coincides with its mirror structure. The (9 0, 1 2) is formed at a temperature of ∼405K and a coverage of θ ∼0.16. Hence in this structure one TA molecule is adsorbed on six Cu atoms. At a coverage of θ ∼0.25 (one TA molecule on four Cu atoms) the c(2 × 4) is built at temperatures between 300K and 405K. Reflection Adsorption Infrared Spectroscopy measurements (RAIRS) showed that tartaric acid molecules are adsorbed as bitartrate in the (9 0, 1 2) and as monotartrate in the c(2 × 4). As on Cu(110), TA forms also ordered arrays on Ni(111) [49] and on Ag(111) [50]. However, no ordered TA structures were observed on Ni(110) [42,51,52], Ni(111)/Au [53] and on oxidized Ni(111) [54].

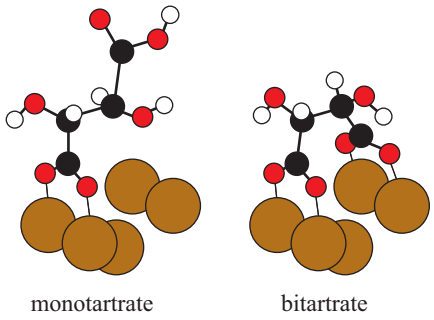

Figure 1.11: The two principle adsorption modes for butanedioic acids, demonstrated for (*R,R*)-TA. The molecule interacts either with one carboxyl group to monotartrate or with both carboxyl groups to bitartrate.

DFT calculations and angle-scanned X-ray photoelectron diffraction experiments (XPD) revealed that chirality is transferred from the chiral TA molecule into the chiral (9 0, 1 2) structure via distortion in the molecular backbone of the bitartrate species due to intramolecular hydrogen bonds between the hydroxyl hydrogen and one oxygen atom of the carboyxylate at the surface [55,56]. This bitartrate footprint is attended by an extension of the Cu-Cu distance underneath the bitartrate molecules from 2.58$\AA$ for clean Cu(110) to 2.63$\AA$ [56]. It was suggested that surface stress is induced in $[1\bar{1}0]$ direction, when more than three carboxylate groups bind next to each other in the same close-packed copper row. Two or more copper atoms must be left vacant in between to counter-balance this stress. This explains the formation of troughs between rows of three bitartrate molecules in $[\bar{1}14]$ surface direction (Figure 1.12) [57]. A surface reconstruction has also been reported for TA adsorbed on Ni(110) [42,51,52].

The (*R,R*)-configuration is the most stable form in the (9 0, 1 2) structure, i.e. (*S,S*)-TA would be destabilized by 10kJ/mol if adsorbed into this domain. Interestingly, calculations claim that no intermolecular hydrogen bonds are involved in the formation of this structure. This leaves only an interaction mediated through the copper surface [58, 59] or other intermolecular interactions like Van der Waals forces. The oxygen atoms of the bitartrate entities are believed to occupy the on-top Cu positions across the two-fold short bridge site. A similar adsorption site has been suggested for alanine [60, 61], glycine [62, 63], phenylglycine [63], formic acid [64–66], acetic acid [67, 68], succinic acid [56] and proline [69, 70] on Cu(110). Although it is assumed that intermolecular H-bonds are not important in the (9 0, 1 2) bitartrate structure, this kind of interaction could be decisive in the formation of the c(2 × 4) monotartrate structure. This is indicated by temperature programed desorption experiments (TPD) with pure TA and racemic

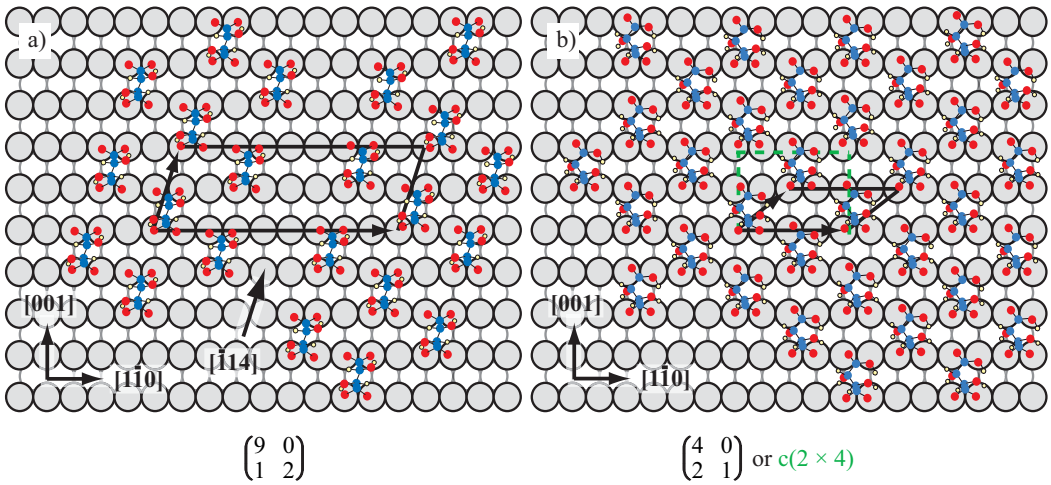

Figure 1.12: a) Model of the (9 0, 1 2) structure of (*R,R*)-TA. The molecules are adsorbed as bitartrate with both carboxyl groups deprotonated. The corresponding opposite (9 0, −1 2) enantiomorph is observed for (*S,S*)-TA. b) Only one carboxyl group is deprotonated and the (*R,R*)-TA molecules form the c(2 × 4).

TA (*rac.*-TA). The c(2 × 4) overlayer of *rac.*-TA shows a CO_2 peak at lower temperature than the c(2 × 4) (*R,R*)-TA structure. The difference is 8K and it was explained by heterochirality of the racemic c(2 × 4). Within a heterochiral c(2 × 4) structure long-range hydrogen bonded chain structures apparently can not be established as easy as in the homochiral arrangement [71, 72].

1.4.4 2D crystal structures of butanedioic acids on Cu(110)

The structures of the butanedioic acids (*R,R*)-TA, *rac.*-TA, *meso*-TA and SU at lower (θ ∼0.16) and higher coverage (θ ∼0.25) are compared in this section.

(*R,R*)-TA

- low coverage: chiral (9 0, 1 2), bitartrate, intramolecular hydrogen bonds, footprint across the two-fold short bridge site
- high coverage: achiral c(2 × 4), monotartrate, long-range hydrogen bonded chains proposed

rac.-TA

- low coverage: (9 0, ±1 2) bitartrate 2D conglomerate, i.e. homochiral domains
- high coverage: c(2 × 4), heterochiral 2D racemate crystal, intermolecular H-bonds proposed

meso-TA

- low coverage: (6 ±1, −1 ±2) conglomerate of homochiral domains, bitartrate with different intramolecular H-bonds than chiral TA, adsorption footprint stronger than for chiral TA proposed

- high coverage: achiral c(2×8), pairs of monotartrate species with hydrogen bonds between carboxylate groups assumed [56, 73, 74]

SU

- low coverage: superposition of achiral c(2×4) and chiral (9 0, $\pm$1 1), monosuccinate in c(2×4) and bisuccinate in (9 0, $\pm$1 1), adsorption-induced chirality as in case of *meso*-TA [75, 76]
- high coverage: p(2×4), bisuccinate, two distinct molecular orientations with opposite chirality, racemate with homochiral chains along [001], adsorption not across two-fold bridge but in diagonal adsorption site as depicted in figure 1.13b) [77]

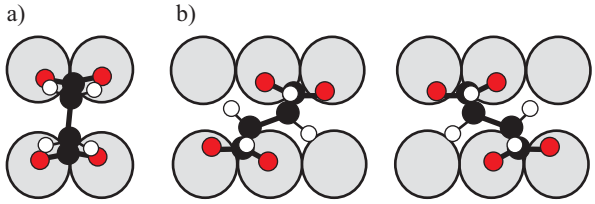

Figure 1.13: Energetically optimized adsorption configuration from DFT of an isolated bisuccinate molecule [56]. Chirality is expressed by the distortion of the molecular backbone as well as the slight twist of the carboxylate group planes compared to the close packed Cu-row direction, as also suggested for the bitartrate species. b) Two enantiomorphous molecular orientations with more diagonal geometry.

1.4.5 Mixing and doping experiments

As mentioned above, the prochiral species *meso*-TA and SU have no preference to single handedness and form always racemic or conglomerate lattices. When SU layers were doped with chiral TA, 2% was enough to induce single enantiomorphism on the entire surface (Figure 1.14). 2% of (*R,R*)-TA established the (9 0, 1 1) overlayer, while after doping with 2% of (*S,S*)-TA only the mirrored (9 0, $-$1 1) was observed. Hence the TA molecules act as chiral seeds and force SU molecules into the same absolute configuration. It is expected that such a low concentration of TA can only have a global influence if the SU domains are large enough. The existence of domain boundaries could in addition be energetically unfavorable and thus act as a supplemental driving force towards homochirality [78, 79]. This effect is called sergeants and soldiers effect: The TA sergeants tell the SU soldiers which sign of handedness they should adopt and the soldiers obey.

The sergeants and soldiers effect was first observed for *n*-hexyl-isocyanate polymers in a liquid environment. A chiral comonomer was able to distort the normally equal probability for left- and right-handed helical sequences [80–82]. The induced effect was dependent on the temperature and also on the used solvent.

The 2D sergeants and soldiers effect was also observed for *meso*-TA with chiral TA as dopant [74, 79].

1.4.6 Enantiospecific substitution of chiral guest molecules

Chiral recognition was observed when chiral TA molecules were adsorbed to the p(2×4) structure of SU. This structure is composed of homochiral lines of bisuccinate molecules with a footprint

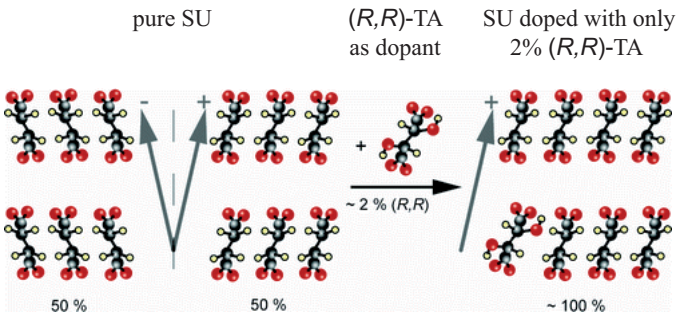

Figure 1.14: Achiral SU adsorbs on Cu(110) in two domains with opposite handedness. All molecules within a specific domain are assumed to have the same chiral distortion in the molecular backbone. 2% of (*R,R*)-TA as dopant induces single enantiomorphism on the entire Cu-surface. (*S,S*)-TA as dopant induces opposite handedness.

as depicted in figure 1.13b). From line to line the handedness of molecules alternates. TA guest molecules are adsorbed as bitartrate only in those lines where the present bisuccinate molecules have a chiral distortion into the same direction as the respective bitartrate, i.e. the same handedness. Thereby TA is adsorbed in the same diagonal footprint as SU and not in the footprint across the two-fold short bridge site as proposed by theory and demonstrated by experiment for pure TA [56, 77].

1.4.7 Enantiomerically unbalanced monolayers

Enantiomeric excess (e.e.) experiments using (*R,R*)-TA and (*S,S*)-TA have been performed by Raval and co-workers. At 20% e.e. (proportion of 60% : 40%) only the majority enantiomer could form large islands, whereas the minority enantiomer was adsorbed only in very small islands. Apart from the ordered islands disordered regions were observed. This symmetry breaking in supramolecular organization was explained by a maximization of the configurational entropy in the disordered regions: The mixing entropy in the ordered regions is zero, but it is largest when the proportion of majority and minority molecules in the disordered region is 1:1. The flux of molecules from ordered islands into the disordered region or from the disordered region into ordered islands depends on the circumference of these islands and on the number of majority or minority molecules. Hence in order to compensate for the larger number of majority molecules the minority enantiomer has to assemble in smaller and more islandes than the majority enantiomer. Thus the probability of a minority molecule to be in the disordered region is increased and the 1:1 proportion can be established [83]. We will discuss this mechanism further below and suggest a different mechanism.

1.5 Aim of the thesis

Malic acid (MA, Figure 1.10) is also a butanedioic acid and it was first isolated from apple juice by the Swedish chemist Carl Wilhelm Scheele in 1785. He referred to it as "acid of apples", which explains the german name Äpfelsäure. In 1787 Lavoisier suggested the alternative name *acide malique*, from the Latin *malum* or apple [84]. In nature MA occurs in its laevo-rotatory (*S*)-enantiomer [85] in unripe fruits like apples, grapes, rowan berries or gooseberries. Both the natural (*S*)-MA and artificial (*R*)-MA are used as food additives (E296). MA confers a tart taste to wine and it is also the source of tartness in food products. In biochemistry malic acid salt (malate) plays an important role in the C4 carbon fixation process and also in the citric acid

cycle [86].

The importance of malic acid for this thesis is given by the difference of the butanedioic acids TA, SU and MA as depicted in figure 1.10. Obviously the main difference of these three molecules is the number of hydroxyl groups. By investigation of the system MA/Cu(110) the following questions are addressed:

1. Which influence has the number of hydroxyl groups on the self-assembly of butanedioic acid molecules on Cu(110)?

2. What is the influence of the lower symmetry of bimalate on Cu(110) (C_1) as compared with bitartrate or bisuccinate (C_2)?

3. In which adsorption geometry does MA adsorb on Cu(110)? That is, does MA adsorb across the two-fold short bridge site as it is theoretically predicted for single TA and SU molecules on Cu(110) or rather in a diagonal adsorption site as proposed for SU in the p(2×4) (Figure 1.13)?

4. What is the nature of the chirality transfer from single molecule into enantiomorphous domains? The self-assembly of the (9 0, 1 2) (*R,R*)-TA structure was first explained by intermolecular hydrogen bonds [45]. But then it was pointed out that only intramolecular hydrogen bonds should play a role in this structure [56]. Consequently other intermolecular or through-metal forces were called to account for self-assembly. The asymmetry of malic acid (only one hydroxyl group) might help to unearth the truth in this question.

Another interesting point is chiral interaction and chiral recognition. Doping achiral SU or *meso*-TA with chiral TA allowed to introduce a single enantiomorphism in the entire system. The chiral bias introduced by the dopant could force molecules to adopt the dopant's handedness. However, neither SU nor *meso*-TA are chiral and thus they basically do not resist to chiral TA. But what happens if one replaces SU or *meso*-TA by another chiral butanedioic acid, for instance by chiral malic acid? It is not possible that a TA dopant can inverse the handedness of single MA molecules. Hence in this case a chiral conflict might be observable, but the consequence for the enantiomorphism of extended 2D domains is worth studying.

Furthermore, chiral recognition is important in sensors and devices as well as crystallization of a racemic compound in homochiral conglomerates or asymmetric crystallization by use of a chiral seed. Thus chiral recognition is in general an important and interesting effect. Since a racemate is expected to separate much more readily into homochiral domains in 2D than in 3D the restriction to 2D might in general ease the investigation of chiral recognition.

In chapter 2 of this thesis the used experimental methods are presented. The adsorption of enantiopure MA on Cu(110) is presented in chapter 3, while the system *rac.*-MA/Cu(110) is topic of chapter 4. Thermal decomposition of MA in TPD experiments is treated in chapter 5. Chiral conflict in self-assembly at molecular level is presented in the chapters 6 and 7.

Chapter 2

Experimental Methods

In this chapter, the used experimental methods will be shortly discussed. These methods are usually used under ultra high vacuum conditions (UHV, pressure in chamber $\leq 10^{-9} mbar$) since a freshly prepared sample should stay clean at least for one hour.

2.1 Sample preparation

The experiments were conducted on a Cu(110) single crystal in chambers with base pressures $\leq 5 \cdot 10^{-10} mbar$. The single crystal was cleaned by sputtering with Ar^+ at a pressure of $\sim 1 \cdot 10^{-5} mbar$ and a voltage of 1kV. Afterwards it was annealed for 2min at about 873K in order to get large atomically flat terraces. Cleanliness was controlled by X-ray photoelectron spectroscopy (XPS), low energy electron diffraction (LEED) or scanning tunneling microscope (STM) respectively (Figure 2.1). The sputtering and annealing cycle was repeated until no contamination was observed anymore. The molecules were then deposited on the clean crystal by means of sublimation from an effusion cell.

2.2 X-Ray Photoelectron Spectroscopy (XPS)

The basic principle of XPS is the photoelectric effect [87]. With XPS it is possible to investigate the surface of a material including an adsorbate until a depth of about 3nm. The photoelectrons typically carry an energy of $> 100eV$. It is possible to determine the chemical composition of the adsorbate. Therefore, XPS is also called Electron Spectroscopy for Chemical Analysis (ESCA) [43, 88–91].

2.2.1 Theory

In XPS a photon with energy $h \cdot \nu$ transfers all its energy to an electron. If the photon energy is sufficiently high the electron is excited into the vacuum. Its kinetic energy E_{kin} is given by

$$E_{kin} = h \cdot \nu - E_{bin} - \phi \,. \tag{2.1}$$

E_{bin} is the binding energy of the electron referred to Fermi level and ϕ the work function (Figure 2.2).

Determination of the kinetic energy E_{kin} of the photoelectron by means of an energy analyzer allows the calculation of the binding energy E_{bin} in the initial state. Each chemical element has characteristic binding energies associated with its atomic core levels, resulting in a characteristic set of peaks in the photoelectron spectrum. Thus by comparing a recorded spectrum with

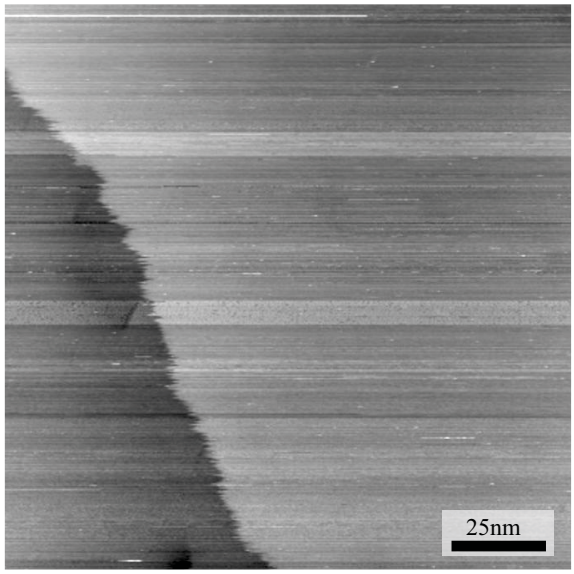

Figure 2.1: 150nm × 150nm scanning tunneling microscope (STM) image of a clean Cu(110) surface: A wide terrace can be seen that merges into a step edge which seems to be frayed. This indicates that atoms attach and detach at this temperature (∼400K) from the step edge. Tunneling conditions were U= -2V and I= 50pA.

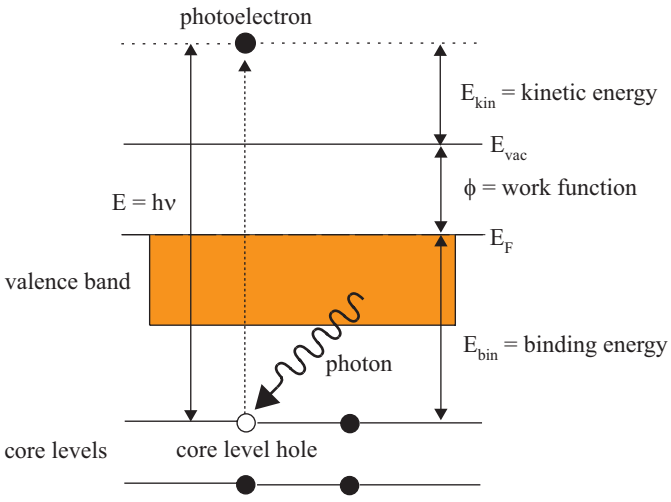

Figure 2.2: A core level electron is excited by an incident photon with energy $E = h{\cdot}\nu$ leading to a core level hole and a photoelectron with kinetic energy E_{kin}. The binding energy is now $E_{bin} = h \cdot \nu - E_{kin} - \phi$.

theoretical spectra, the chemical composition of a bulk material or adsorbate can be determined. Moreover, the intensity of the observed peaks is also related to the number of atoms of the elements at the surface. A shift in binding energy of a core level reflects the chemical state of that atom.

2.2.2 Experimental Setup

X-ray source and a concentric hemispherical analyzer (CHA) with electron detector are the main components of a XPS set-up (Figure 2.3). The X-ray radiation is produced by accelerating electrons from a hot cathode towards a metal anode by applying an electrical field of about 15kV. This induces bremsstrahlung as well as photons with a characteristic energy. Typical anode materials are magnesium and aluminum with the following characteristic energies:

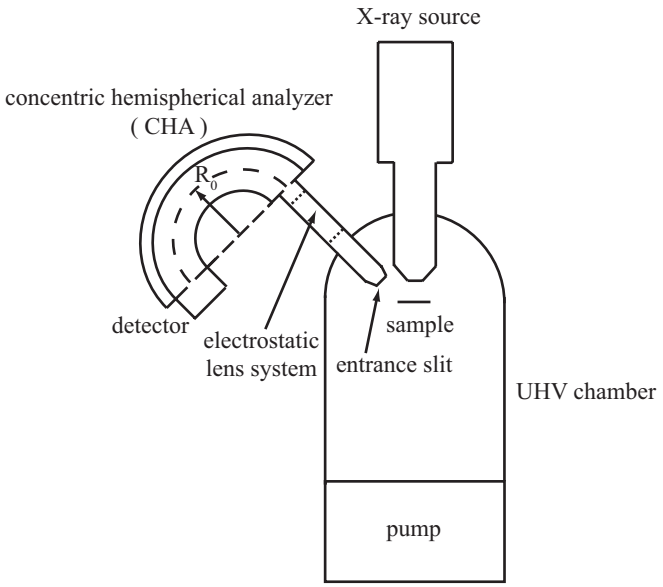

Figure 2.3: Experimental setup of XPS.

$$MgK_\alpha : E = h \cdot \nu = 1253.6eV$$

$$AlK_\alpha : E = h \cdot \nu = 1486.6eV$$

All photoelectrons entering the CHA at the entrance slit are collected, transferred and retarded to the specific analyzer pass energy E_{pass} by the electrostatic lens system. To obtain a spectrum, the lens voltages are scanned and the intensity of electrons corresponding to a certain kinetic energy is determined in the detector. The energy resolution ΔE of the CHA can be improved by either decreasing the pass Energy E_{pass} or by increasing the mean radius R_0.

2.3 Ultraviolet Photoelectron Spectroscopy (UPS)

While in XPS the energy is high enough to excite electrons from a core level, the energy in UPS is chosen to allow the excitation of electrons bound in a valence level.

2.3.1 Experimental Setup

The low energy light used for UPS is produced in a noble gas discharge lamp [43]:

$$He(^1S_0) \rightarrow He^*, He^+, \ldots \ (1)$$

From the (1s,2p) state fluorescence occurs with photon emission via

$$He(^1P_1) \rightarrow He(^1S_0) + h \cdot \nu \ (2).$$

The light of process (2) has an energy of 21.2eV and is the so-called He I radiation. By lowering the He pressure it is also possible to increase the yield of light with a higher energy (40.8eV) from a resonance line of ionized He^+. Since there is no air-proof and transparent material for this wavelength, the He I and He II radiation are admitted window-less to the UHV system. This requires differential pumping stages in order to maintain at least high vacuum in the chamber. As in XPS the kinetic energy of the excited electrons can be determined with the CHA.

2.4 Low Energy Electron Diffraction (LEED)

The principle of LEED measurements goes back to an experiment performed by Davisson and Germer in 1927 [92]. In this experiment they proved the wave nature of electrons by diffraction at a Ni crystal. In order to observe a LEED diffraction pattern low energy electrons (10-500eV) are scattered from a crystal surface. Interference of the elastically scattered electrons leads to a diffraction pattern that - as for X-ray diffraction of 3D crystals - represents the reciprocal lattice. Static LEED does not give any information on the exact position of scatterers in the unit cell, but rather gives the periodicity of the lattice. To get a diffraction pattern the ordered structure must have a minimum size of about 10-30nm depending on the instrument [43].

2.4.1 Theory

In 1923 De Broglie proposed the wave/particle dualism, i.e. a particle with kinetic energy $E_{kin} = p^2/2m$ is equivalent to a wave with wavelength $\lambda = h/p$. Here p is the momentum of the particle, m its mass and h is Planck's constant. The wavelength λ is also known as De Broglie wavelength. In the case of LEED the electrons are accelerated by a voltage V and their kinetic energy is given by $E_{kin} = e \cdot V$. The De Broglie wavelength of such electrons is

$$\lambda(\mathring{A}) = \frac{h}{\sqrt{2meV}} = \sqrt{\frac{150.9}{E(eV)}}. \tag{2.2}$$

If the primary electrons strike a one-dimensional periodic lattice with periodicity a under an incident angle ϕ_0, constructive interference of the backscattered electrons occurs in direction ϕ given by (Figure 2.4)

$$L_2 - L_1 = a \cdot (\sin\phi - \sin\phi_0) = n \cdot \lambda, \ n = 0, 1, 2, 3 \ldots . \tag{2.3}$$

This is the Bragg condition. $L_2 - L_1$ is the optical path difference. Extending the arrangement of periodic scatterers in figure 2.4 into two dimensions, then the lattice points may be considered as an ensemble of parallel rows of scatterers with directions $[h, k]$ and distances $d_{[h,k]}$, where (h, k) are the Miller indices. Equation 2.3 alters to

$$L_2 - L_1 = d_{[h,k]} \cdot (\sin\phi - \sin\phi_0) = n \cdot \lambda, \ n = 0, 1, 2, 3 \ldots . \tag{2.4}$$

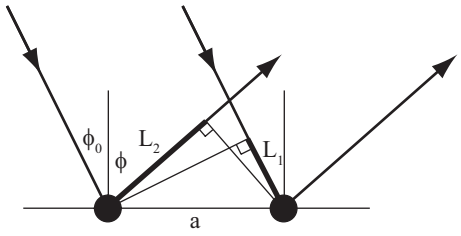

Figure 2.4: The diffraction of electrons from a one-dimensional periodic structure with periodicity a is shown. Constructive interference occurs if the difference in path length $L_2 - L_1$ equals a integer multiple of the wavelength.

2.4.2 Conversion from real space to reciprocal space and vice versa

A LEED pattern shows the lattice of a periodic structure in the reciprocal space. Let $\vec{a_i}, \vec{a_j}$ be the unit cell vector of a 2D arrangement in real space. Then for the unit cell vectors $\vec{a_i}^*, \vec{a_j}^*$ in the reciprocal space holds [43]

$$\vec{a_i} \cdot \vec{a_j}^* = \delta_{i,j} \tag{2.5}$$

$$|\vec{a_i}| = \frac{1}{|\vec{a_i}^*| \sin \gamma^*} \tag{2.6}$$

$\delta_{i,j}$ is the Kronecker Delta (i.e. $\delta_{i,j} = 0$ for $i \neq j$ and 1 for $i = j$). γ^* is the angle between the reciprocal unit cell vectors $\vec{a_i}^*, \vec{a_j}^*$. Thus $\vec{a_1} \perp \vec{a_2}^*$ and $\vec{a_2} \perp \vec{a_1}^*$. In figure 2.5 the situation is represented for an fcc(110) surface.

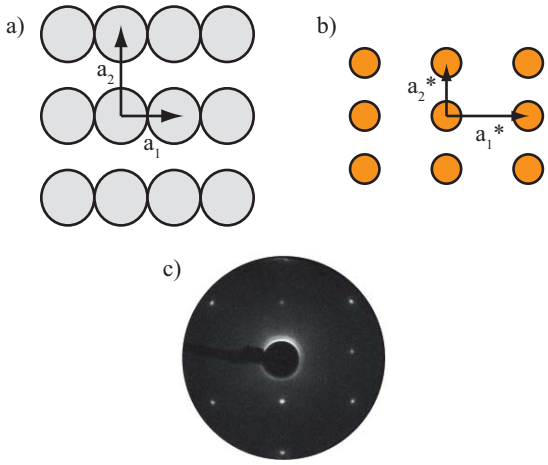

Figure 2.5: a) The Cu(110) surface in real space. The basic vectors $\vec{a}_1$ and $\vec{a}_2$ are indicated. b) A Cu(110) surface in reciprocal space. $\vec{a}_1^*$ and $\vec{a}_2^*$ are the corresponding basic vectors. c) LEED pattern of a clean Cu(110) surface at 74eV.

2.4.3 Experimental Setup

A grounded crystal is placed in front of the LEED apparatus, which usually consists of calottes of three of four grids. The second and third grid are kept on a potential slightly lower than the

primary electron beam energy in order to cut off the inelastically scattered electrons. The first and fourth grid are held on ground potential to avoid field inhomogeneities. Elastically scattered electrons are accelerated towards the fluorescent screen where they excite the phosphorus film upon impact (Figure 2.6). The brightness of the spots is a measure of the frequency of occurrence of a certain structure, while the spot width is indicative for the size of the islands.

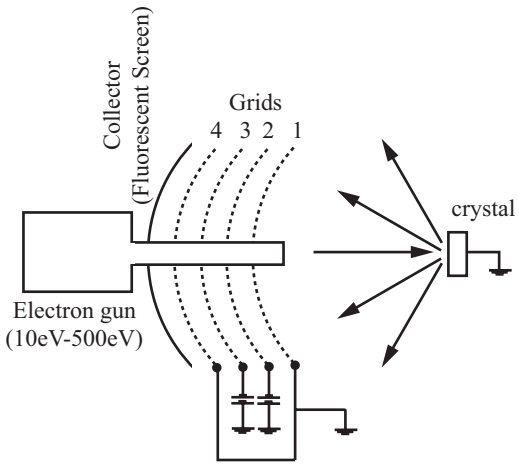

Figure 2.6: The setup for a LEED measurement is shown.

2.5 Temperature Programmed Desorption (TPD)

TPD is an analytical technique that yields information on adsorption/desorption energetics and kinetics. This includes the activation energy of desorption, the order of the desorption step and the pre-exponential factor. The activation energy of desorption is equal to the heat of adsorption, if the adsorption is a non-activated process. This analytical technique has first been described by Apker in 1948 [93].

2.5.1 Theory

At high pumping speed S the desorption rate $N(t)$ is proportional to the measured pressure P [88, 94–96], i. e.

$$P \propto N(t). \tag{2.7}$$

The desorption rate $N(t)$ is related to the surface coverage Θ by

$$N(t) = -\frac{d\Theta}{dt} = k_n \cdot \Theta^n = \nu_n \Theta^n e^{-E/RT}. \tag{2.8}$$

Here k_n is the rate constant, n the reaction order and E is the activation energy for desorption. Equation 2.8 is called 'Wigner-Polanyi equation'.

Lateral interactions among the particles complicate the analysis of TPD spectra. The important variable is the lateral interaction energy relative to the adsorbate-substrate interaction [97]. Including lateral interactions a good description of the multiple peak desorption spectra could for instance be given for β-CO on W [98].

2.5.2 Surface Explosion

If the desorption peaks shift strongly to higher temperatures with increasing coverage and the signal at saturation coverage is extremely narrow a so-called surface explosion rules the desorption process (Figure 2.7). Due to autocatalytic decomposition, an exponential increase of desorption rate of products is observed under isothermal conditions [99].

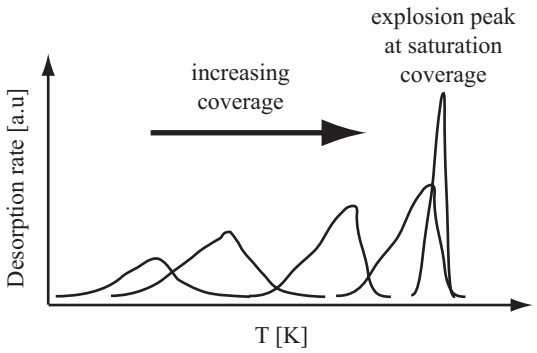

Figure 2.7: Schematic presentation of TPD peaks of a system exhibiting a surface explosion. At maximum coverage a very narrow TPD peak results.

2.5.3 Experimental Setup

The experimental setup for TPD experiments is shown in figure 2.8. The main parts are: quadrupole mass spectrometer, turbo molecular pump (pumping speed in our experiments was S(N_2)= 210L/s) and heat controller with variable heating rate β. Heating up a crystal will always also result in a warming of the vicinity of the crystal. This could affect the TPD spectra. A stainless steel cap with a little hole in the front plate (1mm diameter), placed directly before the mass spectrometer, inhibits this, since all molecules or atoms now detected must originate from the crystal (Figure 2.9). This setup requires a differential pumping of the mass spectrometer. In the spectrometer the intensity of the mass over charge ration (m/Z) is detected for a certain molecule or atom. Plotting the recorded intensity against the corresponding temperature of the crystal results in a TPD spectrum.

2.6 Scanning Tunneling Microscopy (STM)

STM as analytical technique is based upon tunneling of electrons through the vacuum. Binning and Rohrer incorporated this physical effect in a new analytical device [100, 101].

2.6.1 Theory

The transmission coefficient $T(E)$ of an electron with energy E through a one-dimensional potential barrier with width a and height $V_0 > E$ is given by [102] (Figure 2.10)

$$T(E) = \left[1 + \frac{V_0^2}{4E(V_0 - E)} \sinh ka^2\right]. \tag{2.9}$$

$k = \left(2m(V_0 - E)/\hbar^2\right)^{1/2}$ represents the momentum of the electron. If ka is large formula 2.9 can be rewritten as

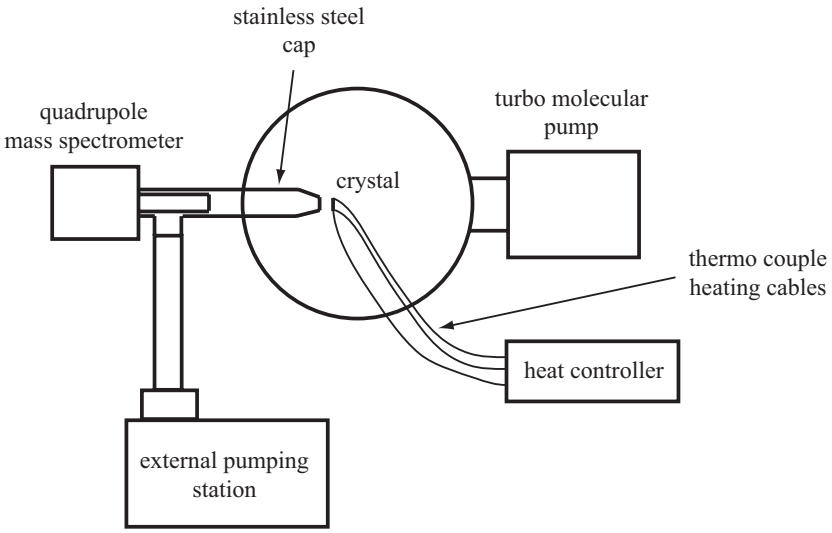

Figure 2.8: The experimental setup for a TPD measurement is shown.

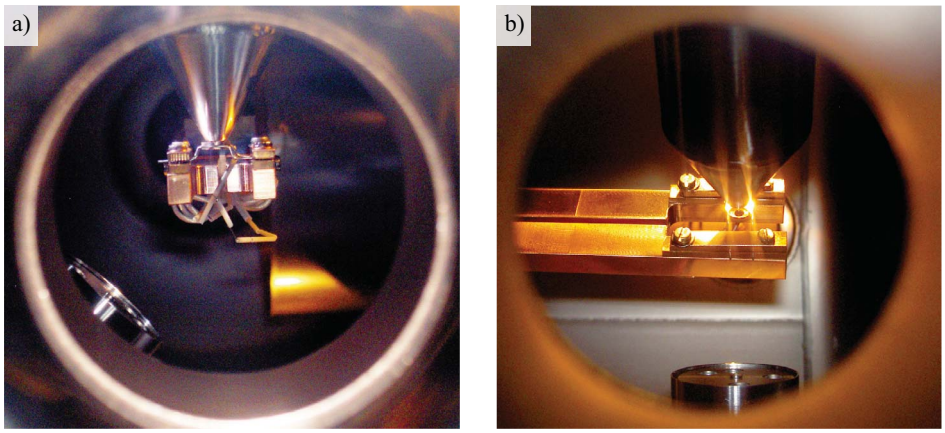

Figure 2.9: a)The stainless steel cap touches almost a Cu(110) surface. The distance between cap and crystal is less than 1mm. In b) the steel cap is yet further away from the crystal surface.

$$T(E) \approx \frac{16E}{V_0} e^{-2ka}. \tag{2.10}$$

Hence the transmission coefficient decreases exponentially with the barrier width.

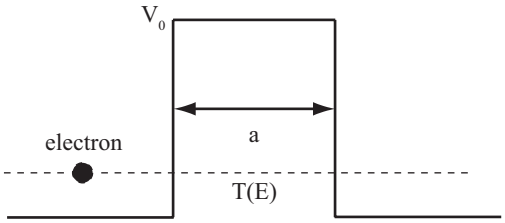

Figure 2.10: The probability of an electron with energy E to tunnel through a potential barrier with width a and height V_0 is given by the transmission coefficient $T(E)$.

The tunneling current density $j(E)$ is now proportional to the transmission coefficient $T(E)$:

$$j(E) \propto T(E) \cdot \delta(E_L - E_R). \tag{2.11}$$

The delta function just means that the energy of the electron on the left side of the potential well $E = E_L$ must be equal to the energy on the right side E_R (energy conservation). In a STM measurement on one side of the potential barrier (= vacuum) one would have the continuous energy levels of the free electrons in the metallic STM tip and on the other side discrete levels of adsorbed molecules or atoms. Because of the delta function in 2.11 the Fermi level in the tip must be adjusted in order to match a certain level in a molecule. This can be done by applying a voltage between tip and sample. The electrons will now tunnel from the tip Fermi level into a free molecular orbital or from a occupied molecular level into the Fermi level. Because of the exponential dependence of the tunneling current with distance STM is extremely height sensitive. By scanning the tip over a single crystal with adsorbed molecules or atoms on it (distance around $10\mathring{A}$) a topographic landscape can be recorded in two ways:

1. The tunneling current is held constant and the vertical displacement of the tip reflects the topography (Constant Current Mode (CCM)).

2. The height is held constant and the current between sample and tip represents the sample relief (Constant Height Mode (CHM)). CHM allows a higher scanning speed than CCM since no height adjustment is needed but the sample surface must be very flat.

The description so far has been simplified. In reality tunneling is not only a one-dimensional process but a three-dimensional one and the influence of the tip shape has also not been considered. J. Tersoff and D. R. Hamann showed that the tunneling current is proportional to the local density of states $\rho(\vec{r}, E)$ on the surface and at the position of the tip [103]. Thus STM images a contour of constant local density of states. The smaller the tip radius r and the distance d between tip and surface the better is the lateral resolution.

2.6.2 Experimental Setup

The tip can be moved by applying a voltage at the three piezodrives P_X, P_Y and P_Z (Figure 2.11). For a certain tip voltage V_T the control unit (CU) detects the tunneling current I. If

the measured current deviates from the chosen value, the *CU* adjusts the voltage applied at the piezodrive P_Z and thus increases or decreases the distance d between surface and tip by Δd. Then the tip is moved in x- or y-direction by changing the respective voltage applied at the piezodrives. At the new position the whole circuit starts again. A map of the vertical displacement Δd at each position represents the topography (CCM mode, subsection 2.6.1). In CHM the procedure is similar, but the height in z-direction is not adjusted. Instead of this the current is recorded and mapped for each position.

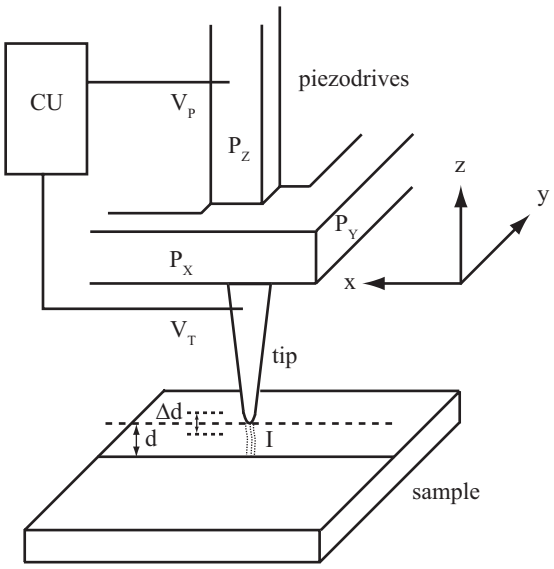

Figure 2.11: STM allows to record a topography map by changing voltages applied at two (CHM) or three (CCM) piezodrives (P_X, P_Y and P_Z). The control unit (CU) actuates the piezodrives in order to meet the chosen parameters and to scan the surface. In doing so the needed height displacement Δd or the measured tunneling current I are the important quantities.

2.7 Reflexion Adsorption Infrared Spectroscopy (RAIRS)

RAIRS is a vibrational spectroscopy technique based on the excitation of dipole moment oscillations by an incident electromagnetic wave. Compared to XPS and UPS, RAIRS delivers more detailed informations about the structural properties of adsorbates.

2.7.1 Theory of RAIRS

The dipole matrix element $\vec{M}_{i,k}$ for a transition from an initial vibrational state ψ_i to a final vibrational state ψ_k is given by [104, 105]

$$\vec{M}_{i,k} = \int \psi_i^* \vec{p} \psi_k d\tau_{el} d\tau_N. \tag{2.12}$$

The integration is over all core and electron coordinates ($d\tau_N$ or $d\tau_{el}$ respectively). $\vec{p}$ is the dipole operator. From the condition $\vec{M}_{i,k} \neq 0$ the following selection rule can be deduced:

Selection rule ($\vec{M}_{i,k} \neq 0$)

$\mathbf{\Delta v = v_i - v_k = 0, \pm 1, \pm 2, \pm 3, \pm 4 \ldots}$
(energy of oscillator with frequency $\boldsymbol{\omega}$ is $\mathbf{E = \hbar\omega\left(v + \frac{1}{2}\right)}$, $\mathbf{v = 0, 1, 2, 3 \ldots}$ is the oscillation quantum number)

$\Delta v = \pm 2, \pm 3, \pm 4 \ldots$ (overtones) follows if one takes a Morse-potential as core potential. Transitions within the same oscillation level ($\Delta v = 0$) are real rotation transitions. The probability and intensity for a transition with $\Delta v = \pm 2, \pm 3, \pm 4 \ldots$ are low.

Terminology for characteristic group frequencies

In figure 2.12 characteristic dipole oscillations and their denotations are shown [43]. In a), b) and c) the atoms move always in opposite directions. d) shows a symmetrical vibration whereas e) shows in principle the same vibration, but this time in an antisymmetric manner. The H-atoms in f) merge and then diverge on a curved course. In g) the atoms again move on curved course, yet this time in the same direction. h) and i) show situation in which the H-atoms move out of the plane. In h) they do it in opposite directions and therefore they twist, while in i) the motion is again simultaneously (wagging).

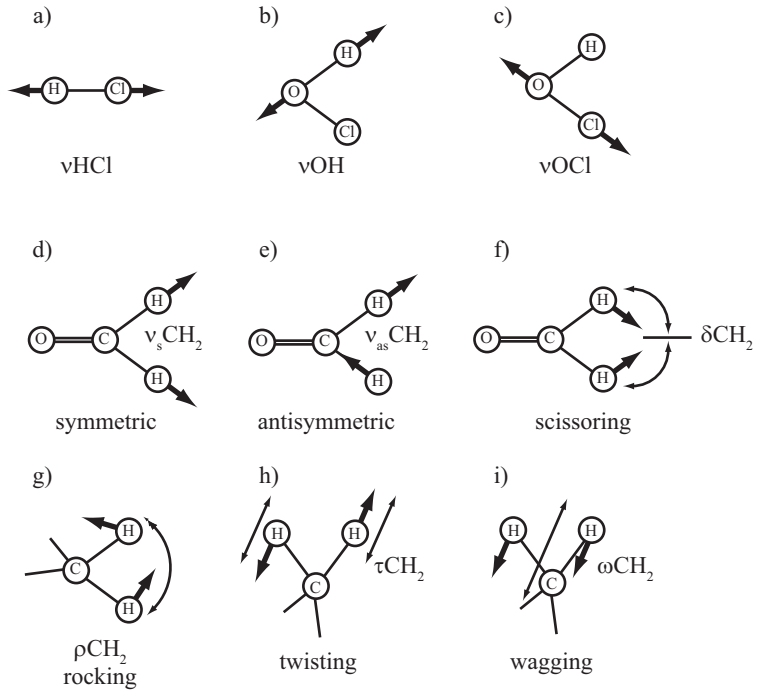

Figure 2.12: Characteristic vibrations are shown: a)-c) valence vibrations in diatomic and polyatomic groups, d) symmetrical stretching, e) antisymmetrical stretching, f) scissoring, g) rocking mode, h) twisting and i) wagging.

Selection rule imposed by metal surface (Metal-Surface Selection Rule)

The adsorption of molecules on a metal imposes another selection rule:

Only changes in dipole moments perpendicular to the metal surface can be excited by an incident electromagnetic wave and are thus dipole active.

There are several explanations for this selection rule. It can on the one hand be explained by the phase change of light reflected from a metal surface [106, 107] or also by the boundary condition of an electric field at the interface [108].

But the most illustrative explanation can be given if one takes a look at a dipole located on a metal surface (Figure 2.13) [88, 109]. The dipole induces an image dipole in the free electron gas of the metal. The image dipole of a dipole oriented parallel to the surface will also be parallel to the surface or interface respectively. But the direction of its dipole moment will be reversed. Therefore the dipole moment changes of real and image dipole due to vibrations will point in opposite directions. The situation is different if the dipole is perpendicular to the surface. Then the resulting image dipole moment points in the same direction as the original one and the same is true for the dipole moment changes. In both cases the separation of the dipole and its image is of the order of molecular dimensions (few $\mathring{A}$). Yet the wavelength of the electromagnetic infrared wave is much larger ($\approx 2 - 12\mu m$). Thus the wave actually sees the superposition of real and image dipole moment changes. In the case of a parallel dipole the superposition will just cancel out and the wave can only excite a perpendicular dipole. However, if molecules are adsorbed on very small metal particles (size $< 20\mathring{A}$) then the surface rule will no longer be valid [108].

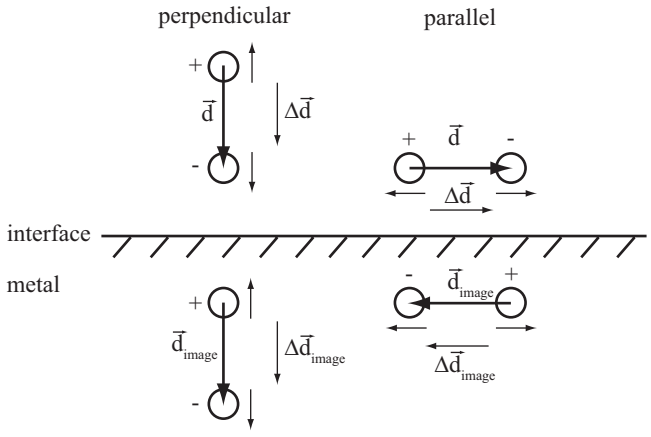

Figure 2.13: Dipoles and their dipole moment changes on a surface are shown. On the left side a perpendicular dipole induces an image dipole pointing in the same direction. This also holds for the dipole moment changes. On the right side a dipole lying parallel to the surface induces an image dipole pointing into the opposite direction. Hence the dipole moment changes will just cancel out.

Principle of RAIRS measurement in UHV

The molecules adsorbed on a single crystal or nanoparticles are irradiated with infrared light (IR) with a wavelength of about $2 - 10\mu m$. Because of the metal surface selection rule (section 2.7.1) the angle of incidence with respect to the surface normal should be rather high ($\approx 80°$). Thus the p-polarized electric field component is almost perpendicular to the metal surface and the coupling between IR light and dipole moment is strong. If one now determines if IR light with a certain wavelength λ (or wavenumber $\bar{\nu} = 1/\lambda$)is absorbed by the molecules, then this shows if the respective dipole oscillations have been excited or not. This can be done by determining either the transmission factor T or the absorption factor A, which are defined as follows (Figure 2.14):

$$T = I_{out}^{ads} / I_{out}^{metal} \tag{2.13}$$

$$A = -log(T) \tag{2.14}$$

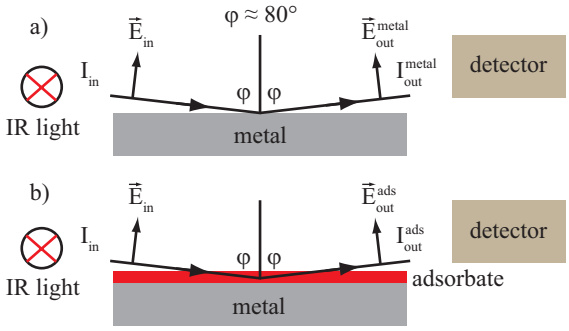

Figure 2.14: a) A clean metal surface is irradiated under grazing incidence by IR light at a certain wavelength and with intensity I_{in}. The reflected light carries the intensity I_{out}^{metal}. In b) an adsorbate has been deposited on the metal surface. Now dipole moment oscillations are excited and the outgoing beam has intensity I_{out}^{ads}. In both cases a detector determines the intensities of the reflected beam.

Equation 2.14 is called Lambert-Beer's law, I_{out}^{metal} is the intensity of IR light reflected from a clean metal surface and I_{out}^{ads} the intensity, when an adsorbate has been deposited on the surface.

The resulting absorption or transmission spectra contains information about the orientation of the molecule and it also indicates how the molecule (functional group) is bound to the surface. Even the adsorption site on a specific surface can be determined: The recorded signal for CO adsorbed on Pd(111) depends for instance on the adsorption site. CO adsorbed at a threefold hollow site shows a different spectrum (peak at 1800-1900 cm^{-1}) than CO at a bridge site (peak at 1900-2000 cm^{-1}) [107,110]. Thus RAIRS offers a means to investigate catalytic systems where it is important to know on which surface site binding occurs.

Frequency shifts in the spectra of adsorbed molecules compared to gas phase spectra can be attributed to the adsorption of the molecules on the metal surface (mechanical shift), to an interaction of a dipole moment with its own image (self-image shift), to a chemical interaction between the molecules and the substrate through electron transfer (chemical shift) or to an increased coverage. Increasing the coverage will lead to a raised coupling of adjacent dipoles or to a stronger interaction of molecules through the metal electrons [58,59]. Thus it is clear that frequency shifts

contain a lot of information about the mechanical and chemical interaction between molecules and a surface, but also about the interaction between neighbouring adsorbates.

A lot of information can also be derived from the lineshap and the halfwidth of the adsorption peaks. If a line width broadening is observed then this could be homogeneous or inhomogeneous. A homogeneous line broadening is caused by the damping of vibrations due to an interaction with the metal surface such as phonon coupling to vibrational modes. An inhomogeneous distribution of molecules and therefore of oscillators results in an inhomogeneous line width broadening. It is determined by the homogeneity of the individual oscillator frequency with respect to the adsorption site and also by the vibrational coupling between individual oscillators.

RAIRS measurement at higher pressures

The IR light used in RAIRS measurements is not polarized. But as seen, only the p-polarized component of the electric field will excite dipole moment oscillations in molecules adsorbed on a metal surface. This is true at UHV and under higher pressure conditions (mbar region). But at higher pressures s- and p-polarized electric field induce dipole oscillations also in the gas phase. By the use of a Photoelastic Modulator (PM) that switches between s- and p-polarized light, the adsorption of molecules on metal surfaces can also be investigated at higher pressures. p-polarized light induces oscillations in the gas phase and in the adsorbed molecules while s-polarized light excites only the molecules in the gas phase. Thus by subtracting the signal of the s-component by the signal of the p-component only the signal corresponding to the adsorbed molecules is left. This means that RAIRS can also be applied at higher pressures. Therefore RAIRS is an excellent tool to investigate catalytic systems because it allows to do adsorption probe on supported nanoparticles (site specific) also under elevated pressure conditions (by use of a PM). In this way the pressure and materials gap, that complicate the investigation of catalytic systems, can be closed to some extent [107, 110, 111].

2.7.2 Fourier Transform Infrared Spectroscopy

The heart of a FTIR spectrometer is a Michelson interferometer, which consists mainly of a fixed mirror M_1, a movable mirror M_2, a beamspliter (for instance KBr) and the IR light source (U-shaped silicon carbide)(Figure 2.15). The beam radiated from the IR source is not monochromatic. Thus the transmission or absorption is measured for all IR waves at the same time. A beamspliter splits the IR light into two beams B_1 and B_2. Since the path length of beam B_2 differs from the path length of beam B_1 by Δx (movable mirror), the phase of B_2 differs from the phase of B_1 by $2\pi\widetilde{\nu} \cdot 2\Delta x$. This can result in a totally constructive ($2\Delta x = n \cdot 1/\widetilde{\nu}$; $n = 0, 1, 2 \ldots$) or destructive ($2\Delta x = (2n+1) \cdot 1/\widetilde{\nu}$; $n = 0, 1, 2 \ldots$ interference. The measured intensity $I(\Delta x)$ of the recombination beam $B = B_1 + B_2$ in the detector is given by

$$I(\Delta x) = S(\widetilde{\nu}) \cdot \cos(2\pi\widetilde{\nu}\Delta x). \tag{2.15}$$

The function $S(\widetilde{\nu})$ includes a possible absorption of IR light with wavelength λ and wavenumber $\widetilde{\nu} = 1/\lambda$ due to excitation of dipole moment oscillations. By using a monochromatic light with well defined wavenumber $\widetilde{\nu}$, the cosinual interference pattern of $I(\Delta x)$ (Equation 2.15) allows a very precise tracking of the movable mirror. For this one can for instance use a HeNe laser with wavelength $\lambda = 633nm$ and wavenumber $\widetilde{\nu} = 15798cm^{-1}$.

$I(\Delta x)$ in equation 2.15 is zero for $\Delta x_1 = 1/4\widetilde{\nu}$ and $\Delta x_2 = 3/4\widetilde{\nu}$. Hence in order to get from one knot in $I(\Delta x)$ to the next one, mirror M_2 would have to be shifted by $\delta x = \Delta x_2 - \Delta x_1 = 1/2\widetilde{\nu}$. The distance between two knots in $I(\Delta x)$ of the HeNe laser $\delta x(HeNe)$ defines the sampling interval. IR light with a higher wavenumber than the HeNe laser would have a shorter distance δx between two knots. However, the position of mirror M_2 is determined by the knots in $I(\Delta x)$ of the HeNe

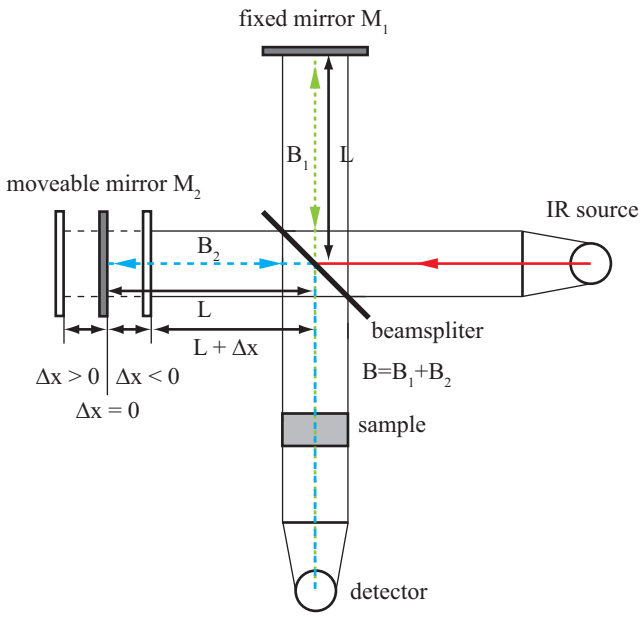

Figure 2.15: The constitution of a Michelson interferometer is shown.

laser. Thus a lot of information of the $I(\Delta x)$ function of IR light with a higher wavenumber than the HeNe laser would be lost. Therefore the wavenumber of the HeNe laser defines a border (so called Nyquist-frequency): no vibrations with wavenumber $\widetilde{\nu} > 15798 cm^{-1}$ can be detected.

The sampling interval $\delta x(HeNe)$ should not be confused with the real distance δx_{real} mirror M_2 is moved. This distance is defined by the resolution. Normally the resolution is chosen to be $4cm^{-1}$, corresponding to a δx_{real} of $1.25mm$.

Superposition of all $I(\Delta x)$ functions of all wavenumbers gives now the interferogram $\sum_{\widetilde{\nu}} I(\Delta x, \widetilde{\nu})$ (Figure 2.16). Since $I(\Delta x)$ in equation 2.15 has a maximum for $\Delta x = 0$ independent of the wavenumber, the interferogram shows a positive interference of all $I(\Delta x)$ at this point. This is called centerburst.

In order to get the spectrum $I(\widetilde{\nu})$ the functions $I(\Delta x)$ must be subjected to a Fourier transformation given by

$$I(k \cdot \Delta\widetilde{\nu}) = \sum_{n=0}^{N} I(n \cdot \Delta x^{'}) e^{i2\pi nk/N}. \tag{2.16}$$

The wavenumber $\widetilde{\nu}$ is here given by the expression $k \cdot \Delta\widetilde{\nu}$ and the displacement Δx is expressed by $n \cdot \Delta x^{'}$, whereas n goes from 0 to N. Hence neither the wavenumber nor the displacement are continuous variables, but discrete functions in k and n. This causes the spectrum $I(\widetilde{\nu})$ to be rather angled (Picket-fence effect). The finite length of the interferogram is in additional responsible for wiggles in the spectrum (leakage effect). Both effects can be weakened by the use of appropriate mathematical methods (zero filling, apodisation).

Advantages of FTIR compared to other RAIRS systems are

- highly precise wavenumber scale (CONNES advantage)
- higher throughput of radiation in FTIR (circular apertures) than in grating spectrometers (slits) (JACQUINOT advantage)
- all wavelength from IR simultaneously on detector (FELLGETT advantage)

JACOUINOT and FELLGET advantage result in an excellent signal to noise ratio.

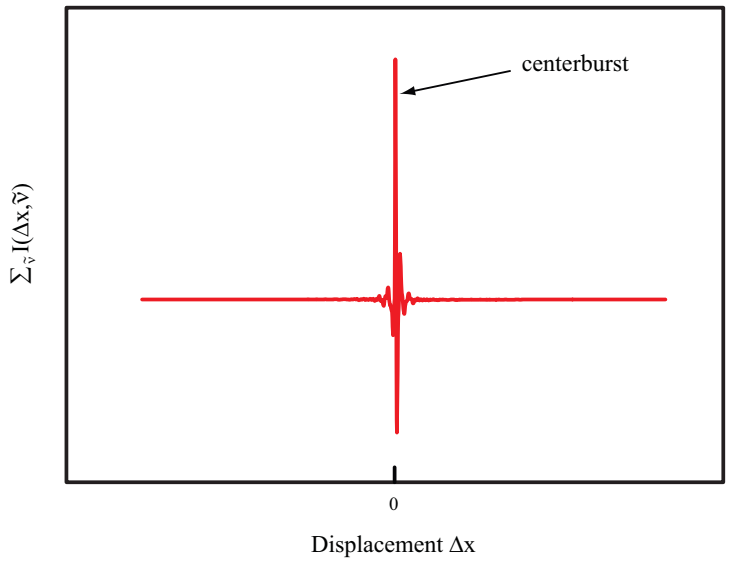

Figure 2.16: A typical interferogram is shown. The centerburst is located at displacement $\Delta x = 0$.

2.8 Assembly of the UHV-RAIRS system

A main part of this thesis work was the assembly of a UHV-RAIRS system. In this section the assembly will be covered and the most important parts will be briefly presented.

2.8.1 UHV-RAIRS system

Figure 2.17 shows the RAIRS system consisting of a main chamber for sample preparation and a small RAIRS chamber, in which the vibrational spectra are recorded.

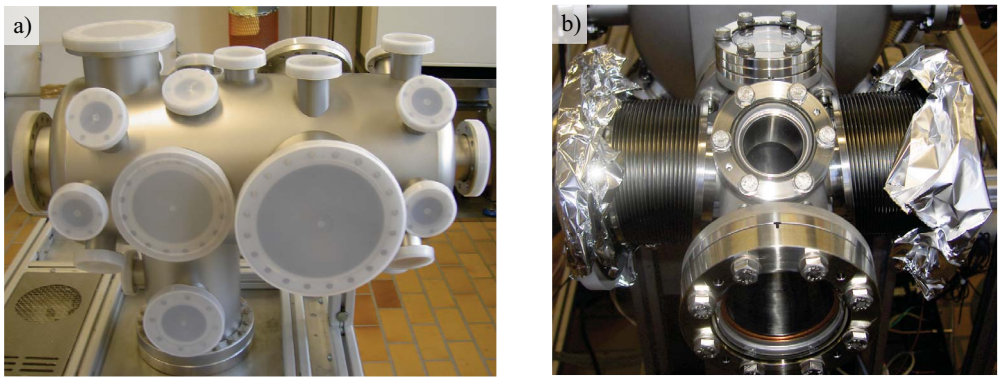

Figure 2.17: a) main chamber of the UHV-RAIRS system, b) RAIRS chamber. The main chamber is used for sample preparation.

Standard surface analytical tools like XPS, LEED and TPD are mounted on the main chamber. An XPS analyzer (PHOIBOS Hemisperical Energy Analyzer by SPECS) and a X-ray source (XR 50 by SPECS) are pumped differentially. During operation the X-ray gun is cooled by a chiller. The mass spectrometer (Balzers Prisma QMS 200) is mounted into a retractable, differentially pumped cap with a pinhole (ø 1mm, section 2.5). Thus only molecules from the crystal are detected

in a TPD experiment (Figure 2.18a)). LEED patterns (Specs ErLEED 1000-A) are recorded with a USB CCM Monochrome camera (DMK 21 AU04 by TheImagingSource, Figure 2.18b)).

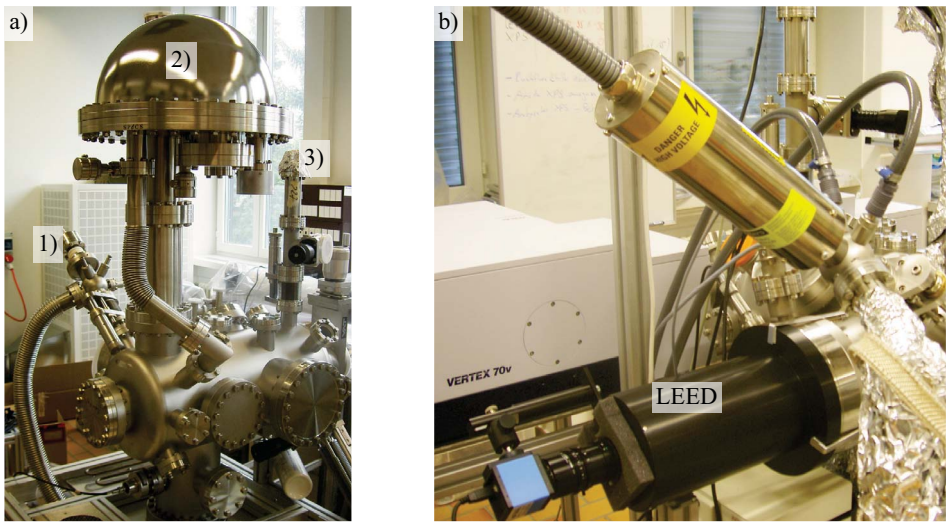

Figure 2.18: a) X-ray source 1), electron analyzer 2) and MS 3) are shown. Gun, analyzer and MS are differentially pumped. b) LEED optics is shown. A camera is used to record the LEED patterns.

Sample cleaning is performed with a sputter gun (IQE 11-A by Specs). By means of a threefold evaporation cell (TCE-BSC by kentax.de) molecules can be deposited on the crystal, which is mounted on a VAb manipulator. Two Ta wires with a diameter of 0.5mm (99.9% purity, temper annealed, by ADVENT Research Materials Ltd.) connect the single crystal with the copper stayer of the manipulator (Figure 2.19). A thermocouple type K is attached at the crystal and connected to a fast heat controller (HA 901 by RKC instruments, 25msec sampling time), which allows to heat up the crystal with a very high slope even when a lot of energy is needed to change the crystal temperature and thus a fast sampling time is required. The heat controller is connected to a power supply (SM 18-50 by Delta Electronics, 12ms rise time) that yields 0-50A current and 0-18V voltage. Depending on the measured crystal temperature the heat controller causes the power supply to conduct current through the Ta wires. In the wires energy dissipation occurs and the crystal is heated up. The crystal can also be cooled down, for instance with liquid N_2 as coolant.

The base pressure in the system is about $5 \cdot 10^{-10} mbar$. It is established and maintained by three different pumps: an ion getter pump, a turbo molecular pump and a titan sublimation pump (TSP, Figure 2.20). The turbo pump (TMU 071P by Pfeiffer) has a pumping speed of S(N_2)= 59L/s. The ion pump (Perkin Elmer) can be switched on at a pressure of about $1 \cdot 10^{-6} mbar$ and has at this pressure a pumping speed for air of S(air)= 270L/s. After having accomplished a good pressure of $\leq 10^{-9} mbar$ in the system the TSP can be used to even improve it. Four gauges are included in the system that cover the whole pressure range from 1000mbar to $1 \cdot 10^{-10} mbar$.

A second evaporation cell can be mounted on the small RAIRS chamber (Figure 2.21). Thus the crystal has not to be moved during RAIRS measurements. By the use of a shot and an all metal angle valve it is even possible to change the cell without venting the system.

By means of special adapters (built in the workshop at Empa) the bellows of the RAIRS chamber are connected with the FTIR spectrometer(VERTEX 70v by Bruker) and the external MCT detector. After crossing an aperture ($0.7mm \times 4mm$ in our measurements) the IR leaves the spectrometer by the mirror box, which is a special adaptation for RAIRS measurements in UHV.

Figure 2.19: Sample holder with the elevated Cu crystal.

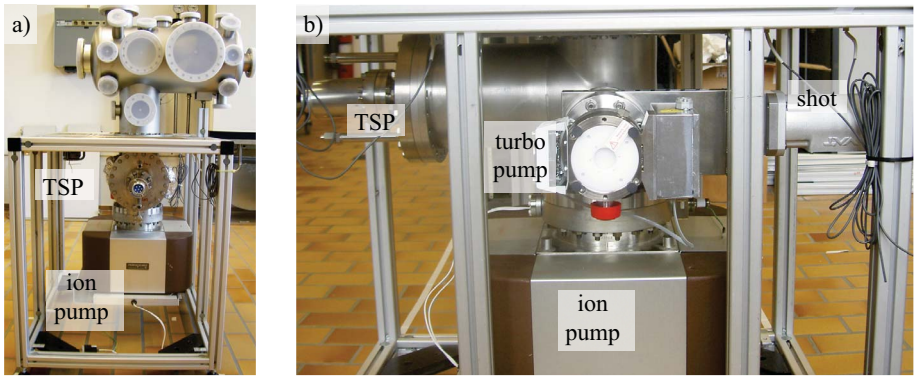

Figure 2.20: a) The ion getter pump and titan sublimation pump (TSP) are shown. Both pumps are mounted at a T-piece below the main chamber. In b) also the turbo molecular pump can be seen that is fixed to the same T-piece as the ion pump and TSP.

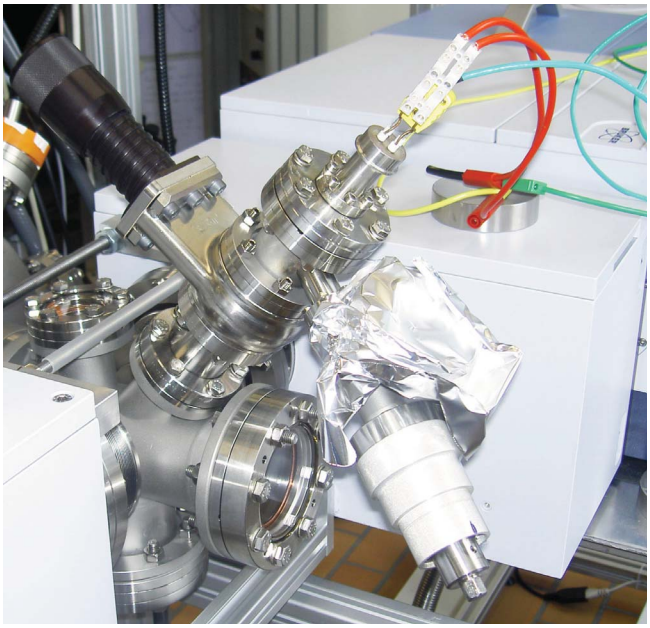

Figure 2.21: An evaporation cell can be mounted directly on the RAIRS chamber. Thus the crystal has not to be moved during the deposition of molecules.

Then the light travels along the belows and enters the RAIRS chamber through CaF_2 viewports (transmission $> 90\%$ for light with wavenumber between $1500cm^{-1}$ and $30000cm^{-1}$, UHV tight until $1 \cdot 10^{-10}mbar$, by LewVac). Due to the aperture the incident IR light has an elliptical shape, which results in a circular projection on the crystal in the RAIRS chamber. The IR light is reflected and then directed, again through a CaF_2 viewport, towards the FTIR detector (Figure 2.22).

In order to reduce substantially absorption of IR light by residual gas both FTIR spectrometer and detector are pumped by a membrane pump (ACP 15, by Adixen). In this way the pressure can be reduced to about $0.5mbar$ as it is depicted in figure 2.23.

For bakeout spectrometer and detector can be moved on carriages back and forth (Figure 2.24).

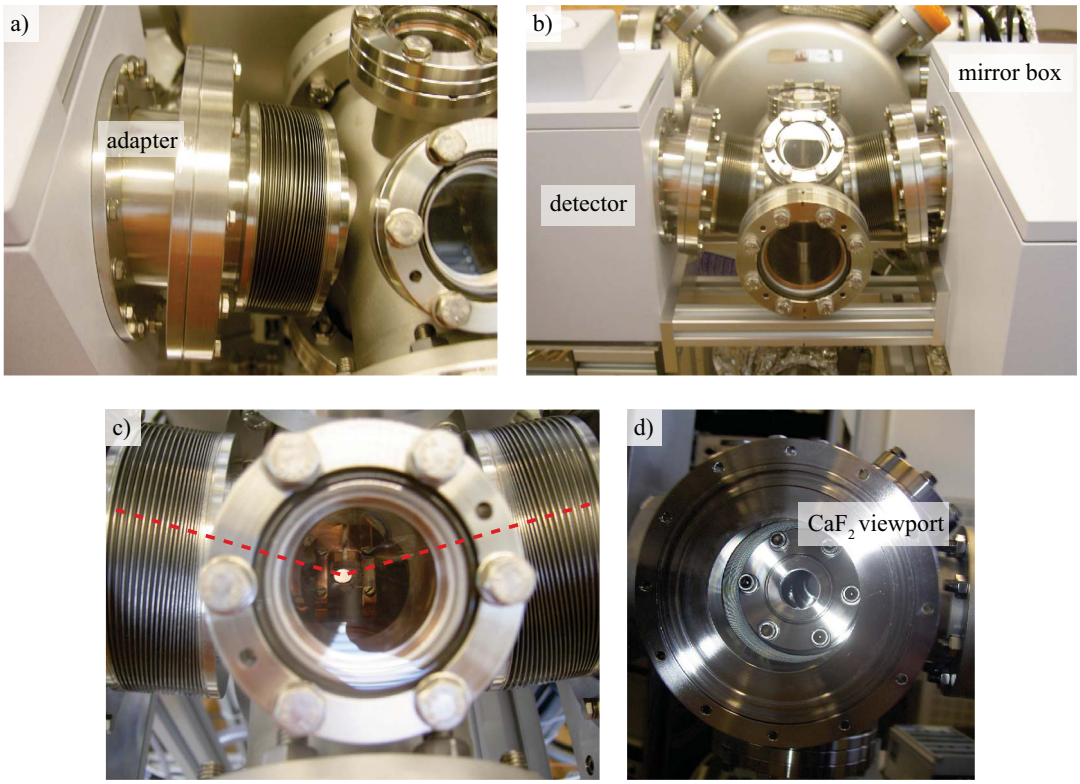

Figure 2.22: a) shows an adapter that connects a below of the RAIRS chamber with the mirror box of the FTIR spectrometer and the MCT detector (shown in b)). In c) the light path is indicated: IR light enters the RAIRS chamber through a CaF_2 viewport, is reflected on a crystal surface and than directed towards the detector. A CaF_2 viewport is shown in d).

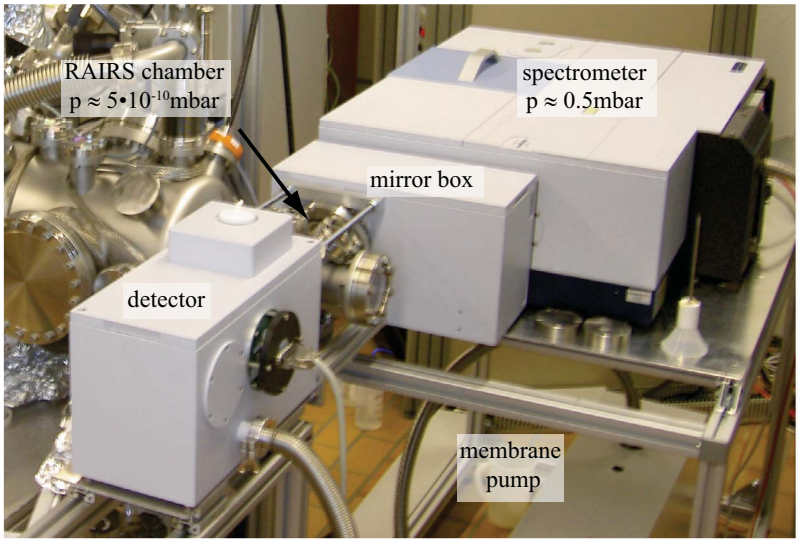

Figure 2.23: A membrane pump creates in the spectrometer/detector a vacuum of $0.5mbar$. However, the pressure in the RAIRS chamber is within the $10^{-10}mbar$ region.

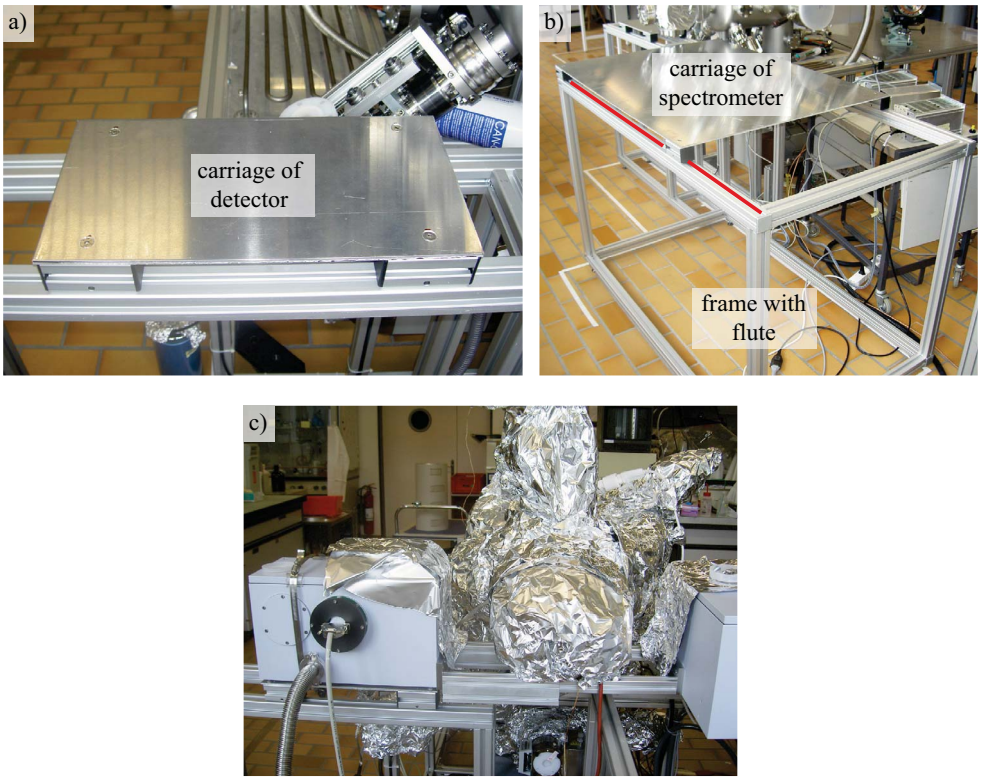

Figure 2.24: a) and b) show the carriages of the detector and spectrometer respectively. In b) one flute in which wheels of a carriage move has been marked red. During the bakeout shown in c) the carriages are moved away from the RAIRS chamber.

2.8.2 Test for proper operation of the UHV-RAIRS system

One way to test for proper operation of the system is to record a RAIRS spectrum of a certain ordered structure and then to compare it with an already published spectrum of the same structure recorded with a different spectrometer. For this test the (4 1, 2 3) structure of (*R,R*)-tartaric acid was chosen since it is easy to prepare: 1ML of (*R,R*)-tartaric acid was heated for 30min at 75°*C*. The resulting RAIRS spectrum and LEED pattern are presented in figure 2.25 and the corresponding vibrations are displayed.

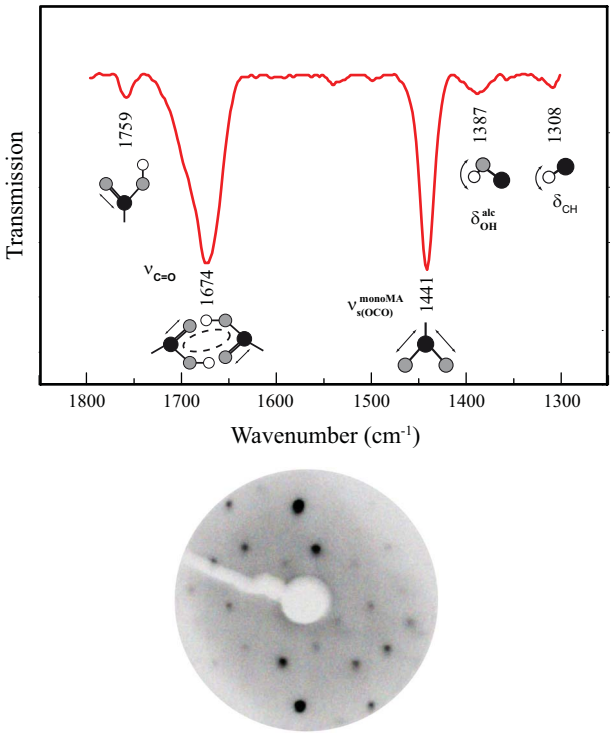

Figure 2.25: a)The RAIRS spectrum of the (4 1, 2 3) structure of (*R,R*)-tartaric acid is shown. In b) the corresponding LEED pattern at 28eV can be seen.

In table 2.1 all the vibrations observed for the (4 1, 2 3) (*R,R*)-tartaric acid structure published in [45] are listed and compared with the observed bands in figure 2.25. It can be concluded that we have successfully assembled the first UHV-RAIRS system in Switzerland. The system works and reasonable spectra can be measured.

Comparison of observed vibration frequencies in cm^{-1}					
vibrations in [45]	1759	1674	1441	1381	1308
vibrations measured	1759	1674	1441	1387	1308

Table 2.1: In this table the observed vibration frequencies of the (4 1, 2 3) (*R,R*)-tartaric structure published in [45] are compared with the frequencies measured with the newly assembled UHV-RAIRS system.

Chapter 3

Two-dimensional self-assembly of chiral malic acid on Cu(110)

In this chapter we will discuss the two-dimensional self-assembly of enantiomerically pure malic acid (MA) on Cu(110). This includes possible adsorption configurations of isolated MA molecules, ordered overlayers observed with LEED and STM as well as informations on the configuration of molecules gained by means of XPS, UPS and RAIRS. If not stated otherwise, the presented data were obtained with (*R*)-MA.

3.1 Adsorption configuration

3.1.1 Models

As tartaric acid (TA) and succinic acid (SU), MA can adsorb on Cu(110) either with one carboxylate group as monomalate or with both carboxylate groups as bimalate. Compared to SU or TA the missing C_2 symmetry of MA allows additional variations. As shown in figure 3.1a) monomalate can either adsorb with the hydroxyl group at the second or third C-atom. Also for bimalate two possibilities exist. A 180° rotation leads to different alignments with respect to adjacent molecules (Figure 3.1b). Hence the missing C_2 symmetry of MA should have an effect on the self-assembly in 2D chiral arrays.

For the bitartrate a conformation across the two-fold short bridge site has been predicted by density functional theory (DFT) and confirmed in X-ray photoelectron diffraction experiments (XPD, Figure 3.1c), left) [55, 56]. In contrast, DFT favours the diagonal conformation (Figure 3.1c, right) for bisuccinate [77]. Since MA is quasi an intermediate between TA and SU, both footprints could be possible.

3.1.2 Density functional theory calculations

In order to determine the most favourable structures among the ones proposed in figure 3.1 DFT calculations have been performed by collaborators. A Gaussian plane wave (GPW) [112] approach as implemented in the code cp2k was used in the local density approximation (LDA). The electron-ion interaction was described by the norm-conserving pseudo-potentials of Godecker-Teter-Hutter (GTH) and a TZV2P basis set was used for all elements of the molecule. For the copper atoms a DZVP basis set was used. All bases were optimized for molecular and condensed phase systems [113, 114]. The Cu(110) was modeled with four layers of 18-24 atoms (three close packed lines) each. Only the top line was allowed to relax during the geometry optimizations. A vacuum region of 20$\mathring{A}$ was included in the direction orthogonal to the surface and full periodic boundary conditions were adopted.

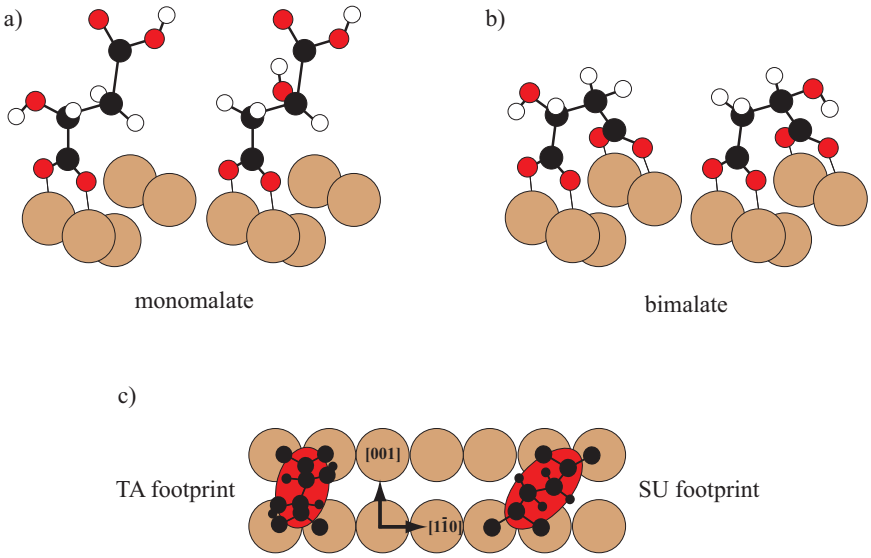

Figure 3.1: Adsorbate models for MA on Cu(110) (a-b) and footprints of TA and SU (c). a) shows monomalate with the OH group either at C2 or C3. In b) the two possible relative orientations of the alcohol group in (*R*)-MA are illustrated. Right-handed footprints of (*R,R*)-bitartrate (left) and bisuccinate (right) on Cu(110) are depicted in c).

Figure 3.2 represents the calculated structures [115]. In a) the optimized configuration of an isolated (*R*)-bimalate molecule is shown. The O-Cu distance at the adsorption sites is 1.90$\mathring{A}$ and the H-O intramolecular distance is 1.87$\mathring{A}$, which is smaller than the 1.97$\mathring{A}$ and 2.03$\mathring{A}$ determined for *meso*-TA and (*R,R*)-TA [56]. The adsorption energy with respect to the gas phase of the doubly deprotonated bimalate amounts to 4.95eV. The energy of the diagonal footprint in b) is 0.24eV higher.

The bimalate prefers lying across the close packed lines of Cu(110) rather than the 90° rotated geometry depicted in c). Interestingly, the two structures in a) and c) are only 0.2eV different in energy.

In the first monomalate configuration in d) the OH group is at the C3 atom and it can reach down to the surface and establish a chemical bond to the substrate. The distance between the hydroxyl hydrogen and the Cu atom is 2.1$\mathring{A}$. This configuration is favored by 0.54eV over the monomalate configuration with alcohol group at the C2 atom shown in e).

3.2 Coverage calibration

Adsorption of malic acid on Cu(110) results in an increasing C1s XPS signal as shown in the inset in figure 3.3. At a certain dose the C1s signal saturates. After Shirley background subtraction the C1s/Cu3s intensity ratio was 0.55 for the saturation coverage at RT.

In the c(2×4) structure one molecule amounts to four Cu atoms. Hence an absolute coverage of θ=0.25 is assigned to this overlayer. Per definition an absolute coverage θ=0.25 is equal to a relative coverage of 1ML (ML = monolayer): 1ML $\widehat{=}$ θ=0.25.

A c(2×4) LEED structure with best quality is observed at a C1s/Cu3s ratio of 0.43, i.e. at a coverage below the RT saturation coverage. Hence this ratio equals to an absolute coverage of θ=0.25 and the relative coverage of 1ML. At C1s signal saturation the absolute coverage is

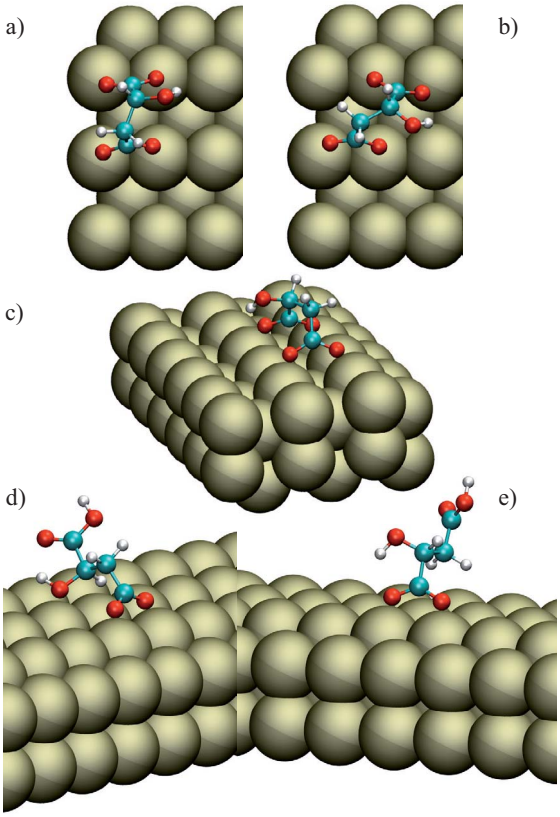

Figure 3.2: Results from DFT calculations. The most stable structure for bimalate (a) is 0.24eV lower in energy than the configuration with a diagonal footprint (b) and 0.2eV lower than the 90° rotated configuration (c). d) The most stable monomalate has the hydroxyl group at the C3 atom interacting with the surface. The configuration with the OH group at C2 is 0.54eV higher in energy (e).

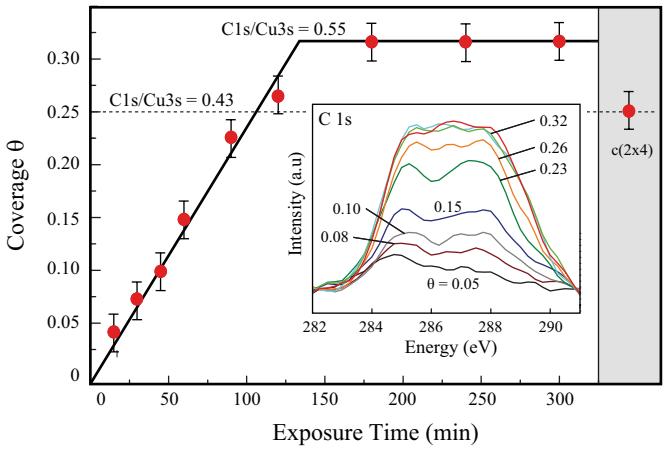

Figure 3.3: Coverage versus exposure time at room temperature. The coverage was calculated from the relative intensity of the XPS C1s peaks in the region 282-291eV and calibrated with respect to the best-quality-c(2×4)-LEED-structure, i.e. θ=0.25. The inset shows the corresponding C1s spectra.

θ=0.32 and the relative coverage amounts to 1.28ML. The RT saturation layer probably involves a partially populated second layer. This is supported by the observation that molecules from the second or higher layers desorb slightly above RT at 307K (Fig. 3.4).

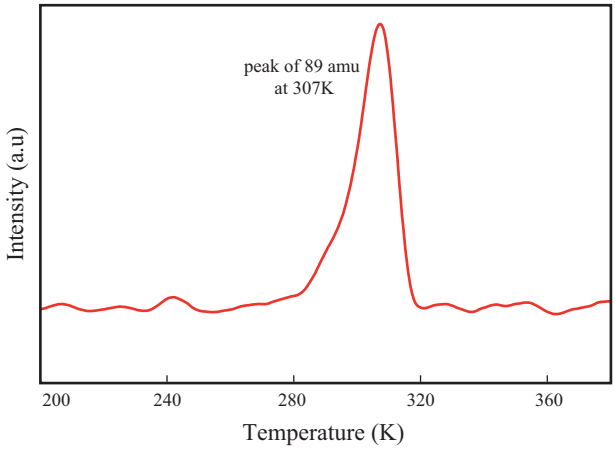

Figure 3.4: TPD spectrum of a multilayered *rac.*-MA sample after exposure at 80K. The heating rate was β=4.1K/s. The 89 amu fragment ($HOOC-CH(OH)-CH_2\cdot$) is representative for an intactly desorbing molecule.

In the case of absolute coverage θ we make a difference between the global (θ^{global}) and the local absolute coverage (θ^{local}). The global coverage θ^{global} is the amount of MA deposited on the single crystal. The local coverage θ^{local} is the coverage of a certain ordered superstructure. Only if this structure covers the complete crystal surface, global and local coverage are identical. This is rather rare in the case of MA/Cu(110). More commonly the ordered structure is embedded in low ordered regions, making it necessary to distinguish between local and global coverage.

3.3 XPS curves

The system tartaric acid on Cu(110) allowed to establish a good understanding of the C1s binding energies in XPS. This was mainly possible due to detailed RAIRS experiments performed by Raval and co-workers for (*R,R*)-TA, identifying which adsorbate species is present in certain phases [45, 75]. In figure 3.5 peak fits for different coverages, including a *rac.*-MA multilayer spectrum, are depicted. The following assumptions were made for fitting the XP spectra:

1. Similar to TA/Cu(110) annealing at low or medium coverage creates a bimalate species.

2. A monomalate species is formed at high coverage.

The bimalate species is then expected to show three peaks arising from the carbon atoms in COO^-, $CH(OH)$ and CH_2. Hence the corresponding ratio of peak areas should be 2 (COO^-) : 1 ($CH(OH)$) : 1 (CH_2). The same ratio is also expected in the fit of the multilayered spectrum. But this time the peak with double area is due to the carboxylic acid group $COOH$, since deprotonation to bimalate only occurs at direct contact to the copper surface, i.e. in the monolayer.

For monomalate four C1s peaks with equal area are expected owing to the $COOH$, COO^-, $CH(OH)$ and CH_2 groups.

Tabel 3.1 summarizes all the fits represented in figure 3.5. The peak energies and FWHM's (in parentheses) are indicated in eV. The values from the fits are compared to literature values.

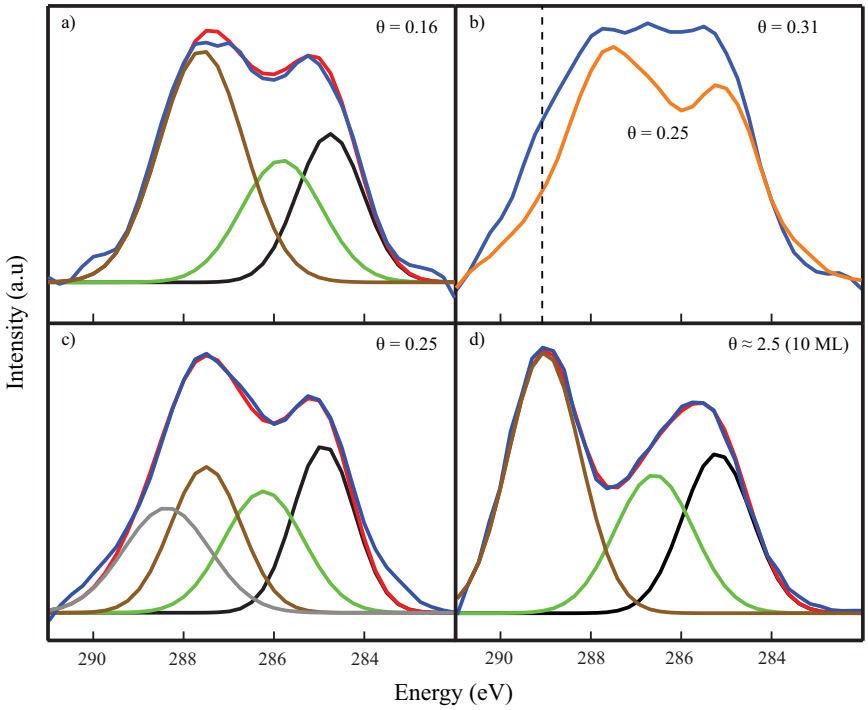

Figure 3.5: C1s XPS signals (blue curves) for differently prepared MA layers. The sum of the fitted peaks is displayed in red. a) 50% of a saturated monolayer ($\theta^{global} = 0.16$) after annealing for 5min at 343K. A bimalate adsorbate mode is assumed in the fit. b) Spectrum of a sample at RT saturation ($\theta^{global} = 0.32$) compared with the spectrum taken from a c(2×4) structure. c) Spectrum of a c(2×4) structure and corresponding fit for a monomalate adsorbate mode. d) Multilayered *rac.*-MA sample (≈10ML).

Components of C1s (*R*)-MA spectra in figure 3.5				
Coverage / system	$CH(OH)$	COO^-	$COOH$	$-CH_n$ $(n = 1, 2, 3)$
0.16	285.8 (2.1)	287.6 (2.2)	-	284.8 (1.7)
0.25	286.2 (2.1)	287.5 (1.8)	288.4 (2.25)	284.9 (1.6)
2.5	286.9 (2.2)	-	289.5 (2.0)	285.4 (1.7)
bi-(*R*,*S*)-TA [73]	286.5	288.0	-	-
bi-(*R*,*R*)-TA [73]	286.4	287.9	-	-
mono-(*R*,*S*)-TA [73]	286.2	287.7	288.6	-
mono-(*R*,*R*)-TA [73]	286.2	287.8	288.6	-
formic acid/Cu(110) [116]		287.7		
acetic acid/Cu(110) [117]		288.2		285.0
glycine/Cu (polycryst.) [118]		288.2		286.2
cysteine/Cu (polycryst.) [119]		288.6		286.1

Table 3.1: The C1s binding energies and full-width-at-half-maximum (FWHM, in parentheses) in eV obtained from peak fitting of XPS curves represented in figure 3.5. At low coverage a bimalate adsorption mode is assumed after annealing. At θ=0.25 MA is assumed to be adsorbed as monomalate. Values from the literature are also listed.

Figure 3.5a) shows the XP spectrum of a bimalate layer, for which in LEED a (1 2, −8 2) structure has been observed (Figure 3.8 in section 3.6). A comparison of the RT saturation spectrum with the C1s peak of the c(2 × 4) structure can be seen in figure 3.5b). A high energy shoulder coincides with the multilayer carboxyl signals (dashed line). This supports the conclusion that at RT the second layer is partly populated. The C1s peak acquired from a c(2 × 4) is again shown in figure 3.5c). In this case the corresponding fit is made for monomalate and hence four different chemical shifts are taken into account. The monomalate spectrum has a slightly more pronounced high energy shoulder than the bimalate spectrum in 3.5a), but the difference in C1s binding energy between carboxyl and carboxylate is only 0.8eV (Table 3.1) and hence both spectra appear to be quite similar. This simple picture of bimalate in the case of low coverage and moderate annealing and monomalate at high coverages roughly holds. But, as will be shown in the RAIRS section, perfect layers containing only a single adsorbate mode are difficult to prepare.

3.4 UP spectra

In figure 3.6a) the UP spectrum from the clean Cu(110) surface is shown. The main features are the peaks arising from the Cu 3d bands between 2-5eV. The spectrum from a (5 3, −9 6) overlayer (θ=0.19, 15min annealed at 343K) is depicted in b). As compared to the clean Cu surface, peaks have evolved in the region between 6 and 10eV. Furthermore, the 3d Cu peaks are not that intense anymore. The 3 d peak at ∼5eV is now higher than the two others, while the second peak at ∼3eV is rather a shoulder. But not only the height of the 3d peaks is different, they are in addition slightly shifted to higher binding energies. This indicates that the 3d band of Cu are involved in the binding of MA to the Cu(110) surface. The peak at 5eV in the (5 3, −9 6) spectrum in 3b) is assigned to the lone pairs of binding oxygen from the carboxylate groups. The peak that appears at about 7eV is identified with the σ_{C-C} orbital, that one at 9eV with σ_{OCO} and π_{OCO} and in the last peak at ∼10eV σ_{OH} and π_{CH2} are assumed to contribute. The assignments were made by comparison with handbooks of HeI photoelectron spectra [120, 121] as well as measured spectra of formic acid, formaldehyde, acetic acid and acetaldehyde on Cu(110) [116, 122].

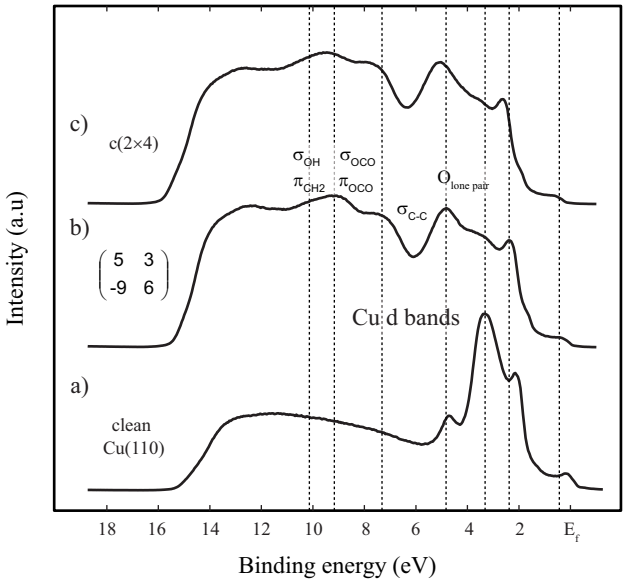

Figure 3.6: UP spectra for different MA structures. a) represents the spectrum of the clean Cu(110) surface. Mainly the 3d Cu bands contribute to the signal. b) Spectrum of the (5 3, −9 6) overlayer at coverage θ=0.19. c) c(2 × 4) layer at θ=0.25.

The spectrum in 3b) is representative for all preparations and structures. Although the adsorption mode is changed between bimalate and monomalate (c(2×4) layer in 3c)), UPS does not reveal striking differences. This is not the case for RAIRS, which clearly helps to distinguish between adsorbate modes.

3.5 RAIRS measurements

As shown for tartaric acid on Cu(110), RAIRS allows to distinguish different adsorbate modes [45]. We use the same assignments of IR bands as been made for TA. Figure 3.7 shows IR spectra of differently prepared samples. The shown spectral range has bands that are particularly sensitive for the adsorbate mode.

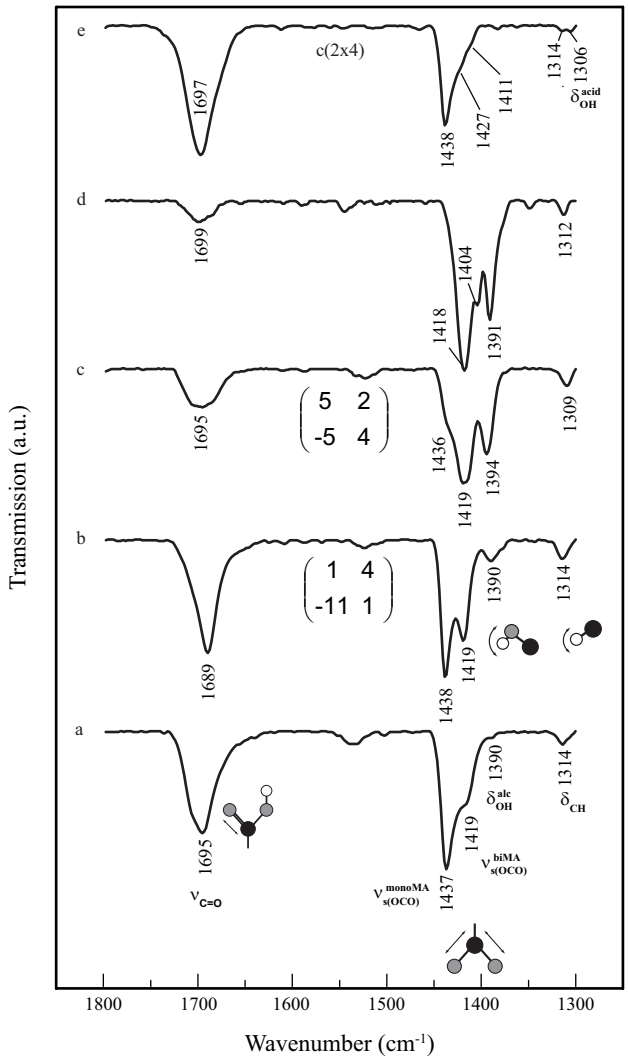

Figure 3.7: IR spectra showing the transmission of (R)-MA overlayers. a) θ=0.21 at RT. b) θ=0.20 after 20min at 348K. c) θ=0.20 after 30min at 383K. d) θ=0.124 after 20min at 333K. e) θ=0.25 after 5min at 343K. Superstructures observed in LEED are also indicated for spectra b), c) and e).

All the spectra basically show in varying intensity the following peaks

- C=O stretching mode ($\nu^{C=O}$) at $1695 - 1700 cm^{-1}$

- symmetric OCO stretching mode (ν_S^{OCO}) of the carboxylate at $1436 - 1438 cm^{-1}$ for monomalate
- symmetric OCO stretching mode (ν_S^{OCO}) of the carboxylate at $1418 - 1419 cm^{-1}$ for bimalate
- deformation mode of the hydroxyl group (δ^{OH}) at $1390 - 1394 cm^{-1}$
- CH deformation band (δ^{CH}) at $1309 - 1314 cm^{-1}$, although this vibration could also be identified as wagging of the whole methylene group in the backbone (γ^{CH_2}, $1311 cm^{-1}$ for SU [75])

Figure 3.7a) represents the RT spectrum of MA at a coverage θ=0.20. It is dominated by monomalate, although a band characteristic for bimalate ($1419 cm^{-1}$) can also be identified. This feature becomes stronger upon annealing, which indicates an activated process for bimalate formation (Fig.3.7b)). The strong CO stretching mode attests that there is still monomalate present in the layer after 20min annealing at 348K. Further annealing for 30min at 383K increases the intensity of the ν_S^{OCO} at $1419 cm^{-1}$, as shown in figure 3.7c). Although the intensities of the monomalate bands at $1695 cm^{-1}$ ($\nu^{C=O}$) and $1436 cm^{-1}$ (ν_S^{OCO}) decrease simultaneously, they do not disappear. Hence at this coverage a pure bimalate layer cannot be prepared.

On the other hand at lower coverage θ=0.124 this is almost achieved after 20min at 333K. In figure 3.7d) the ν_S^{OCO} of monomalate at $1436 cm^{-1}$ has disappeared from the spectrum and the CO stretching is now rather small. A second band at $1404 cm^{-1}$ appeared as shoulder of the bimalate ν_S^{OCO} at $1418 cm^{-1}$. Such a double band was also observed and reported for bitartrate (ν_S^{OCO} at 1430 and $1410 cm^{-1}$ in [45]).

The OH deformation band δ^{OH} at $1391 cm^{-1}$ is much more intense in case of bimalate, but not observed at all in the dense c(2×4) overlayer that has monomalate as main building block (Fig. 3.7e)). This can either be assigned to a strong intra- or intermolecular hydrogen bonding to the carboxyl group of monomalate or simply to the fact that this mode has a larger dipole moment component perpendicular to the surface in bimalate than in monomalate. A strong interaction of the OH group with the surface as calculated for the best monomalate configuration shown in figure 3.2 in subsection 3.1.2 (distance of OH group to surface only $2.1 \AA$) could be another reason for the absence in this monomalate spectrum.

The pronounced shift between the ν_S^{OCO} bands of the two different adsorbate modes is assigned to strain in the bimalate backbone. The band at $1411 cm^{-1}$ might be a strongly shifted δ^{OH} band. The δ^{OH} of the acid group is maybe observed here as well. Yet, its intensity is hardly above the noise or distinguishable from the δ^{CH} band.

All prepared layers with exception of the low coverage bimalate and the high coverage monomalate contain a mixture of both adsorbate modes. STM in section 3.7 seems to confirm this observation, since only rarely perfect monolayers could be observed.

3.6 LEED experiments

Depending on coverage and preparation conditions, basically seven different ordered phases have been observed in LEED. The diffraction patterns of six (R)-MA overlayers, plus three corresponding (S)-MA enantiomorphs and a (S)-MA structure obtained by further annealing are represented in figure 3.8.

Table 3.2 lists the preparation conditions (coverage, temperature and annealing time) for all structures shown in figure 3.8.

From table 3.2 it is seen that many phases can be prepared in the same global coverage regime of θ=0.15 to 0.175. Only the c(2×4) (θ^{global}=0.25) and the (1 4, −11 1) (θ^{global}=0.19 to 0.22) need higher coverages. Prolonged annealing alone can induce rearrangement in the layer. Figure

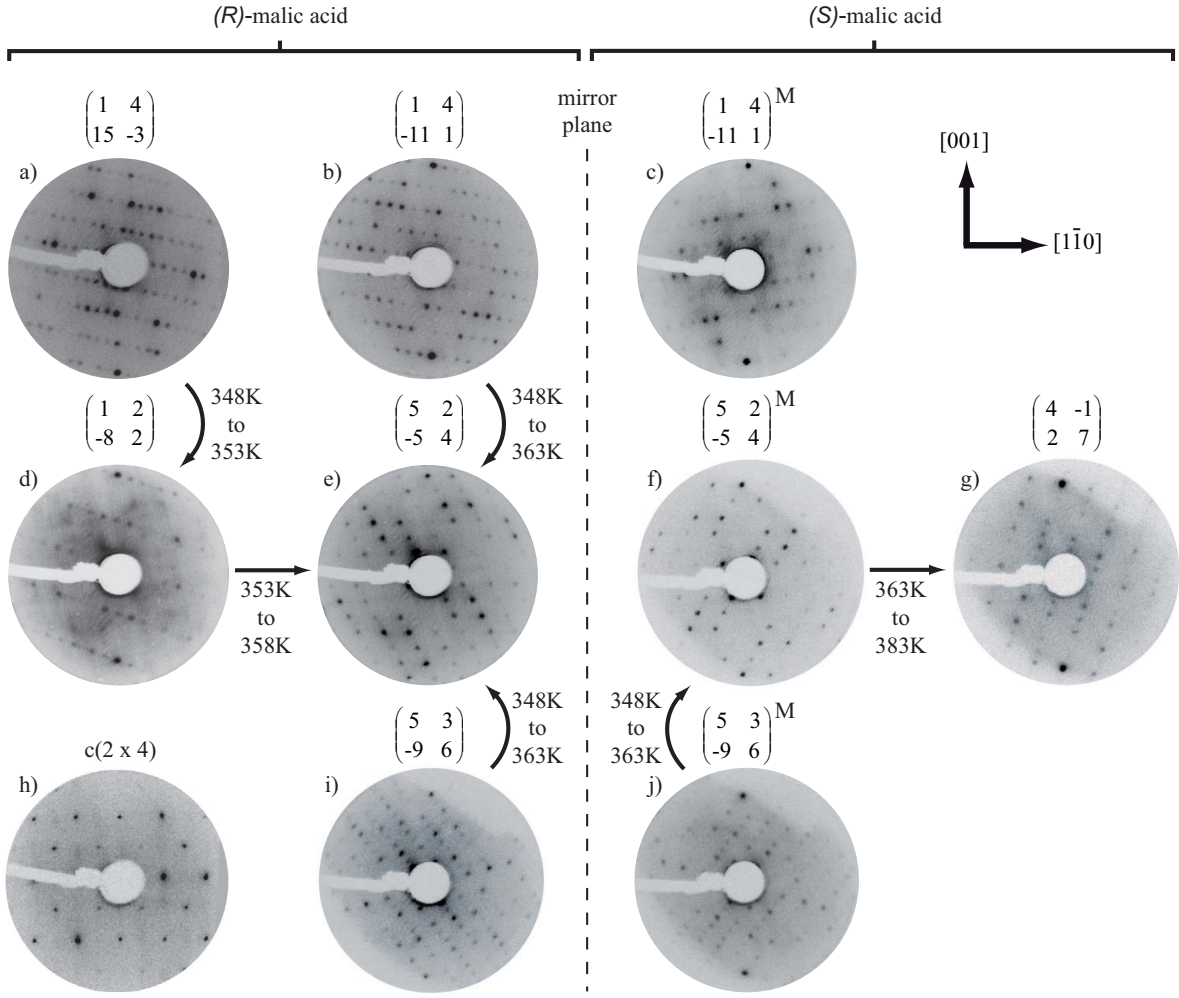

Figure 3.8: LEED patterns of different ordered structures of MA enantiomers. The dashed line separates enantiomorphs of (R)-MA and (S)-MA. The M superscript at the matrices denotes the opposite enantimorph (see ref. [44] for details). Phase transition induced by thermal treatment are indicated by arrows. Electron energies in eV: a), e): 22; b): 25; c): 26; f), j): 28; d), g), i): 27; h): 63.

Preparation conditions of observed LEED structures			
Structure	θ^{global}	Enantiomer	Annealing procedure
$\left(\begin{smallmatrix}4 & -1\\ 2 & 7\end{smallmatrix}\right)$	0.175	S	60min / 383K
$\left(\begin{smallmatrix}1 & 2\\ -8 & 2\end{smallmatrix}\right)$	0.15-0.17	R	5min / 353K
$\left(\begin{smallmatrix}1 & 4\\ 15 & -3\end{smallmatrix}\right)$	0.17-0.19	R	5min / 343K
$\left(\begin{smallmatrix}1 & 4\\ -11 & 1\end{smallmatrix}\right)$	0.19-0.20	R	60min / 338K
$\left(\begin{smallmatrix}1 & 4\\ -11 & 1\end{smallmatrix}\right)^M$	0.205-0.22	S	25min / 343K
$\left(\begin{smallmatrix}5 & 2\\ -5 & 4\end{smallmatrix}\right)$	0.17-0.20	R	10min / 363K
$\left(\begin{smallmatrix}5 & 2\\ -5 & 4\end{smallmatrix}\right)^M$	0.175	S	60min / 363K
$\left(\begin{smallmatrix}5 & 3\\ -9 & 6\end{smallmatrix}\right)$	0.126-0.175	R	60min / 348K
$\left(\begin{smallmatrix}5 & 3\\ -9 & 6\end{smallmatrix}\right)^M$	0.15-0.175	S	60min / 348K
c(2×4)	0.25	R	5min / 348K

Table 3.2: The preparation conditions of observed LEED structures. The M superscript at the matrices denotes the opposite enantimorph (see ref. [44] for details).

3.8 shows that different annealing procedures at identical global coverage allow for instance the conversion of the (1 4, 15 −3) to a (1 2, −8 2)[1], then to a (5 2, −5 2) and finally into a $(4\ -1,\ 2\ 7)^M$ structure (or (4 −1, 2 7) in case of (S)-MA).

The c(2×4) is the only overlayer with a rectangular unit cell. All other lattices express enantiomorphism, that is the adlattice has an oblique tilt angle with respect to the substrate lattice and breaks therefore the mirror symmetry of the substrate. The lattice tilt angle of the opposite enantiomer is of same magnitude but into the mirrored direction. This all suggests that the chirality of the molecule has been transfered into the extended lattice. As assumed for tartaric acid and amino acids this transfer occurs on the molecular level through chiral distortion of the molecular backbone. Intermolecular or through-metal forces induce a 2D arrangement in a chiral array [45, 48, 55–57, 75].

The LEED method reveals ordered domains down to 20nm. STM measurements evidenced that many ordered structures occur only in small islands that would not be detected with LEED. The poor quality of the (1 2, −8 2) LEED pattern allows to conclude that this phase is not well ordered. Interestingly, for TA this structure dominates in this coverage regime after thermal activation and seems to be much more stable.

[1] This structure is identical to the (R,R)-TA structure originally coined as (9 0, 1 2) and later named (1 2, −9 0) [45, 83]. Recently suggested new matrix notation rules require (1 2, −8 2) as identifier [44].

3.7 STM measurements

Other than via static LEED, STM allows to determine how molecules are arranged within a unit cell. Nine different (*R*)-MA structures represented in figures 3.10 - 3.12 have been identified by STM.

The preparation conditions are displayed in the one-dimensional phase diagram in figure 3.9.

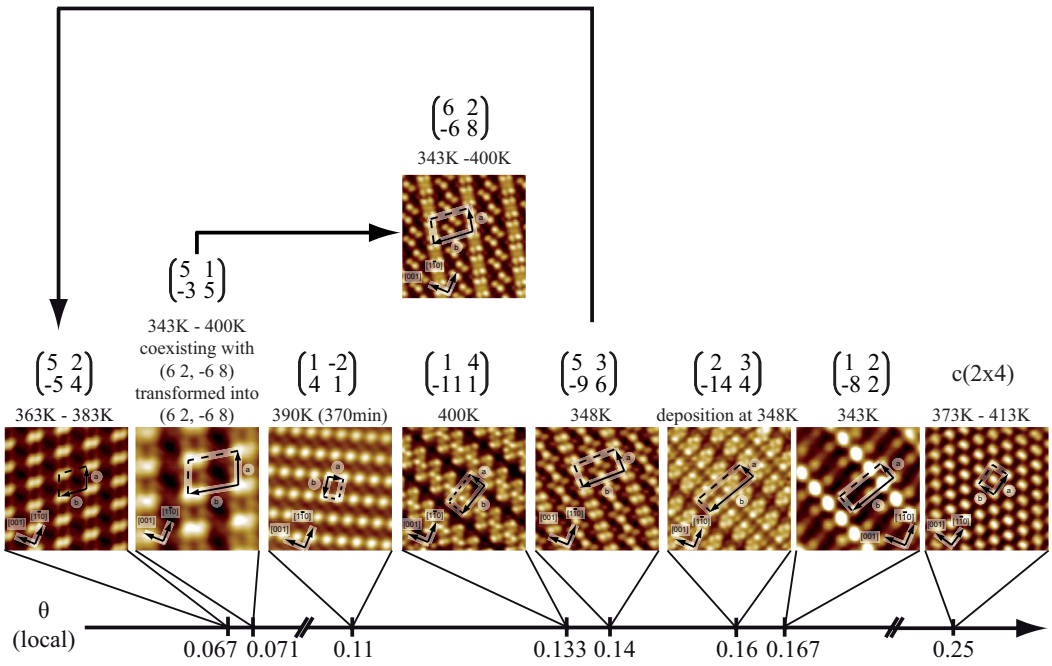

Figure 3.9: One-dimensional phase diagram of all (*R*)-MA structures observed by STM. Local coverages and annealing temperatures are indicated.

As shown in table 3.3 not all overlayers observed with LEED have been observed with STM and vice versa. This might be due to:

- The domain size is below the transfer width of the LEED optics and hence a small island might not be observed in STM scans. Only four of the observed STM structures covered basically the entire crystal surface: $(6\ 2,\ -6\ 8)$, $(5\ 3,\ -9\ 6)$, $(5\ 2,\ -5\ 4)$ and $c(2 \times 4)$.
- Identical preparation conditions in STM and LEED experiments were not easily achieved. In LEED experiments the temperature at the crystal could be controlled directly by means of a spot-welded thermocouple, while in STM experiments the sample temperature was only indirectly measured at the sample holder. Furthermore, the lack of LEED and global coverage determination via XPS in the STM-apparatus aggravated the reproduction of experiments in the STM chamber.

In figures 3.10 - 3.12 long-range STM images, high resolution filtered STM images (insets), and tentative model structures based on the STM appearance are presented. The high-resolution insets are aligned as the structure models. The STM parameters are listed in the figure captions. In all structures but the $c(2 \times 4)$, bimalate is used as adsorbate mode in the models.

The structures shown in figure 3.10 have the lowest packing density. The first two have dimers arranged along the $[\bar{1}14]$ direction as building blocks. Only the distance between dimers varies. In the $(1\ -2,\ 4\ 1)$ structure a complete row of molecules is aligned in this direction. A peculiar

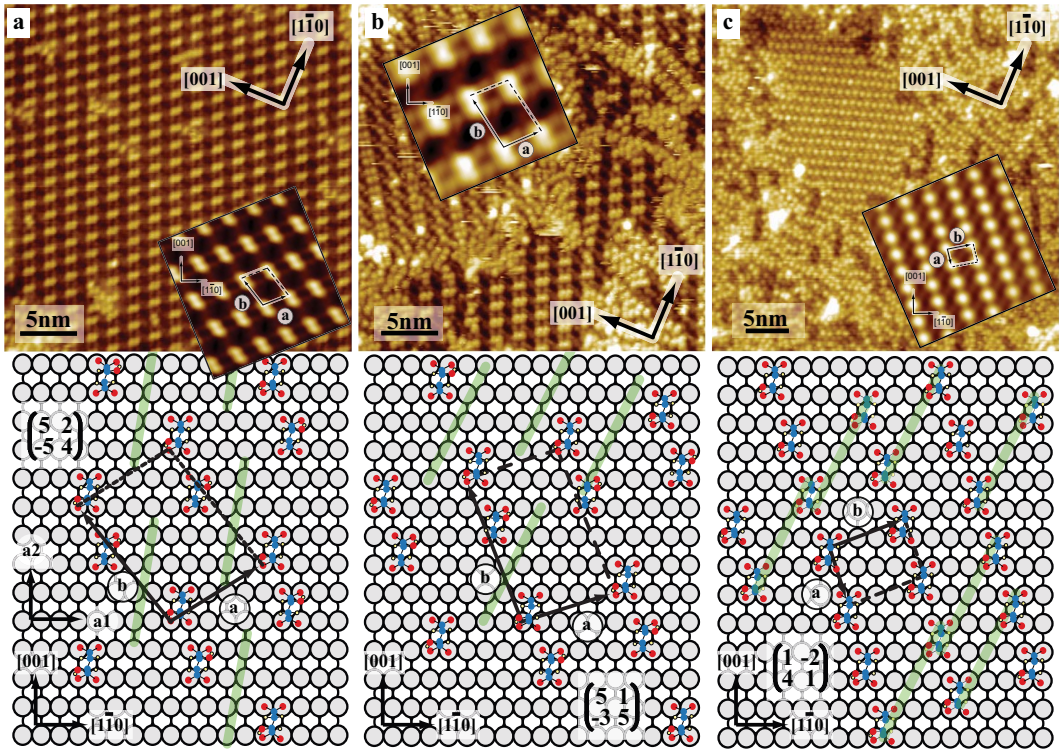

Figure 3.10: STM images and model structures for three (R)-MA overlayers. a) (5 2, −5 4), θ^{local}=0.067 (U= -1.93V, I= 50pA); b) (5 1, −3 5), θ^{local}=0.071 (U= -1.85V, I= 50pA); c) (1 −2, 4 1), θ^{local}=0.11 (U= -1.93V, I= 50pA). The high resolution insets are aligned with respect to the structure model alignment. Dimers or the complete row of molecules are oriented along the [$\bar{1}$14] direction. Green lines indicate the dim stripes observed in STM images. Insets: a) 8nm×8nm, averaged 30× , b) 5nm×5nm, averaged 10× , c) 8nm×8nm, averaged 30× .

Comparison of observed LEED and STM structures			
LEED structure	STM structure	θ^{global}	θ^{local}
$\begin{pmatrix} 4 & -1 \\ 2 & 7 \end{pmatrix}$	-	0.175	-
$\begin{pmatrix} 5 & 2 \\ -5 & 4 \end{pmatrix}$	$\begin{pmatrix} 5 & 2 \\ -5 & 4 \end{pmatrix}$	0.17-0.20	0.067
-	$\begin{pmatrix} 5 & 1 \\ -3 & 5 \end{pmatrix}$	-	0.071
-	$\begin{pmatrix} 1 & -2 \\ 4 & 1 \end{pmatrix}$	-	0.110
-	$\begin{pmatrix} 6 & 2 \\ -6 & 8 \end{pmatrix}$	-	0.133
$\begin{pmatrix} 1 & 4 \\ -11 & 1 \end{pmatrix}$	$\begin{pmatrix} 1 & 4 \\ -11 & 1 \end{pmatrix}$	0.19-0.20	0.133
$\begin{pmatrix} 5 & 3 \\ -9 & 6 \end{pmatrix}$	$\begin{pmatrix} 5 & 3 \\ -9 & 6 \end{pmatrix}$	0.126-0.175	0.140
-	$\begin{pmatrix} 2 & 3 \\ -14 & 4 \end{pmatrix}$	-	0.160
$\begin{pmatrix} 1 & 2 \\ -8 & 2 \end{pmatrix}$	$\begin{pmatrix} 1 & 2 \\ -8 & 2 \end{pmatrix}$	0.15-0.17	0.167
$\begin{pmatrix} 1 & 4 \\ 15 & -3 \end{pmatrix}$	-	0.25	0.25
c(2 × 4)	c(2 × 4)	0.25	0.25

Table 3.3: Comparison of observed LEED and STM structures. Global and local coverages are indicated

feature in all three structures of figure 3.10 are stripes (indicated as green lines) connecting the molecules of adjacent dimers. In the (5 2, −5 4) overlayer (Fig. 3.10a)) the stripes run parallel to the (1, 4) substrate vector, whereas the stripes in the (5 1, −3 5) and (1 − 2, 4 1) (Fig. 3.10b) and 3.10c) are directed parallel to the (3, 4) substrate vector.

These stripes are a strong indication for reconstruction or large strain in the substrate. Adsorption induced strain is also assumed for TA on Cu(110) [57] and Ni(110) [42,51,52]. However, this is the first time that such strain is observed directly in STM and it indicates that a strong chiral footprint is casted into the substrate. This might be the way how the handness of an adsorbate is recognized throughout the layer.

The next three structures in figure 3.11 have local coverages between θ^{local}=0.133 and 0.144. In the model of the (6 2, −6 8) overlayer a pair of [$\bar{1}$14]-dimers is placed next to each other and on the corner of the unit cell. In addition four molecules are placed in the center of the cell.

Such a four-molecule unit is also proposed for the (5 3, −9 6) phase, but here the alignment is slightly different. Finally, also in the (1 4, −11 1) and in the (2 3, −14 4) structures (Fig. 3.12a)) this four-molecule motif is observed. In the case of the (2 3, −14 4) overlayer the bright appearance of one molecule suggests that one of the molecules might be in a monomalate configuration (yello filled ellipses).

Between the pairs of [$\bar{1}$14]-dimers in the (6 2, −6 8) structure (Figure 3.11), inset) a higher intensity than for the substrate in general can be seen. This indicates either a substantial buckling of the substrate or even a coordination compound formed between Cu and molecules. Such a compound has been observed for carboxylates on copper surfaces with and without adding additional metal atoms from the gas phase [123].

All chiral structures reveal empty troughs between rows of molecules. Such channels have also been observed in the chiral "(9 0, 1 2)" overlayer of (*R,R*)-TA on Cu(110) [45–48] and they appear

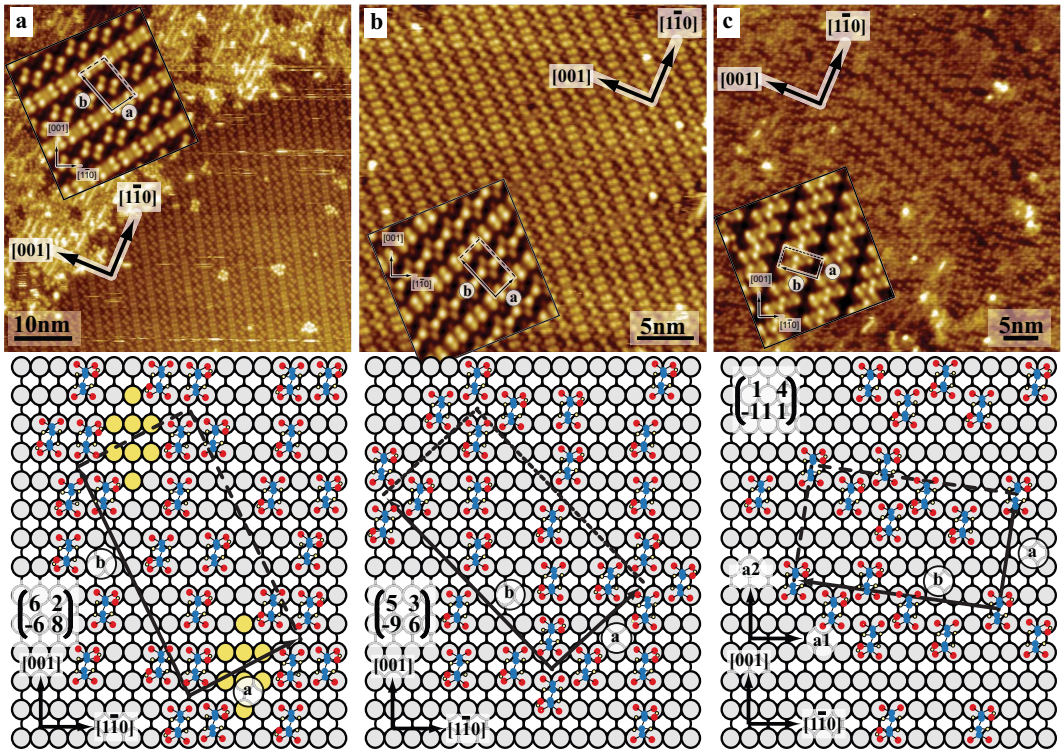

Figure 3.11: STM images and models for (R)-MA structures with local coverage θ^{local}=0.133 and 0.14. a) (6 2, −6 8), θ^{local}=0.133 (U= 1.57V, I= 60pA). Substrate areas with higher STM intensity are marked in yellow in the model. b) (5 3, −9 6), θ^{local}=0.14 (U= -1.9V, I= 50pA); c) (1 4, −11 1), θ^{local}=0.133 (U= 0.715V, I= 50pA). Insets: a) 10nm×10nm, averaged 100× , b) 7nm×7nm, averaged 10× , c) 5nm×5nm, averaged 10× .

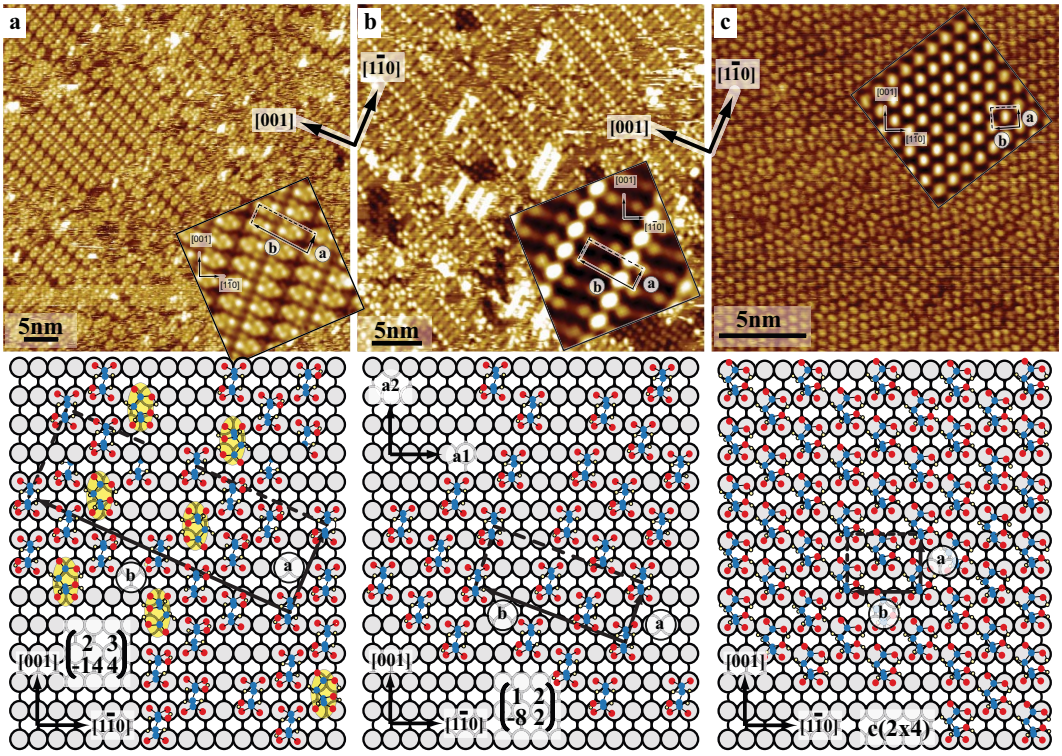

Figure 3.12: STM images and models for three different (*R*)-MA polymorphs. a) (2 3, −14 4), θ^{local}=0.16 (U= 1.75V, I= 75pA); b) (1 2, −8 2), θ^{local}=0.167 (U= -1.85V, I= 50pA); c) c(2×4), θ^{local}=0.25 (U= -1.162V, I= 1nA). Insets: a) 10nm× 10nm, no average, inverse FT, b) 5nm× 5nm, no average, inverse FT, c) 5nm × 5nm, averaged 30× , inverse FT.

again for the corresponding (1 2, −8 2) MA phase in figure 3.12b). As for TA, a triple-molecule motif is observed, interrupted by empty chiral spaces. The molecules of the middle row are imaged with much higher intensity than those close to the troughs. This holds for TA as well as MA and can be assigned to a substantial buckling of the substrate underneath. In the case of (*R,R*)-TA strain has been proposed, but a reconstruction was excluded. The amino acid lysine induces on the other hand chiral faceting on Cu(100) after annealing at 430K [124]. Hence at least nano-faceting could occur under the three molecules. The rows of molecules in the (1 2, −8 2) are aligned along the $[1\bar{1}4]$ direction. This is the mirror-like alignment as compared to the three low local coverage phases in figure 3.10. Obviously, a different relative alignment of molecules may induce the opposite chiral footprint at a surface. For racemic and (*S*)-proline, opposite footprints have been found to coexist in a (2 × 4) phase on Cu(110) [69, 70]. In the model of the (1 2, −8 2) MA phase in figure 3.12b) all molecules are assumed to be oriented identically. On the other hand, in the models representing the three low coverage structures represented in figure 3.10 every second molecule in a dimer or the row is rotated by 180°.

The averaged STM image of the c(2 × 4) MA overlayer in the inset of figure 3.12c) confirms nicely the LEED pattern periodicity. However, this structure is not perfectly ordered at the local scale, as can be seen in the large-scale STM image. Again, this is in contrast to TA, where a perfectly ordered c(2 × 4) can be observed. This observation can be assigned to the possibility that monomalate is randomly adsorbed with its hydroxyl group at the second or third carbon atom, as mentioned above, and the intermolecular hydrogen bonding occurs not uniformly.

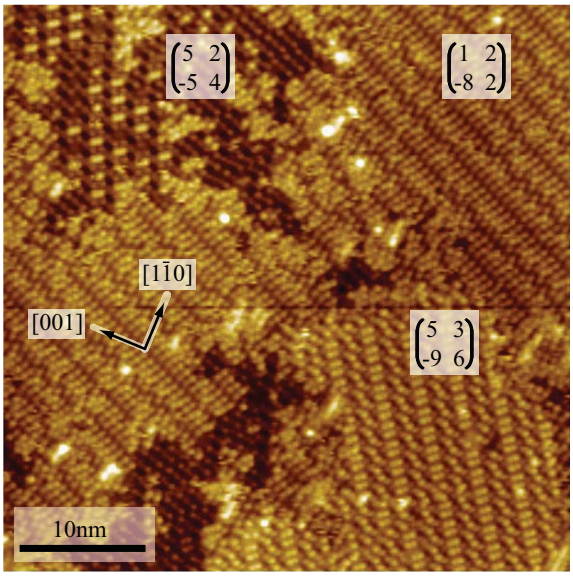

Figure 3.13: The coexistence of three different phases at θ^{global}=0.16 after annealing for 45min at 348K is shown. A rearranged substrate lattice can be identified in areas between the phases. U= -1.93V, I= 50pA.

Prolonged annealing (45min at 348K) of a (*R*)-MA layer at θ^{global}=0.16 allowed to identify three coexisting phases (Figure 3.13). In LEED experiments a transition from the (5 3, −9 6) to the (5 2, −5 4) and from the (1 2, −8 2) to the (5 2, −5 4) phase has been observed (Fig. 3.8). The local coverage of the more stable (5 2, −5 4) overlayer is by a factor of two smaller. This is again a strong indication that the underlying mechanism is not a close-packing phenomena, but rather a phase transition that involves the rearrangement of the substrate. In the areas between the molecules chains of Cu atoms are visible. The direction of theses chains is the same as the

direction of the dim stripes described for the (5 2, −5 4) above. In addition a pair of atoms can be identified between the dimers. Especially for the Cu(110) surface a high mobility of Cu adatoms, detaching and attaching at surface steps has been observed previously even at room temperature. Adsorption of MA onto such dynamic substrate leads most likely to a new substrate structure underneath the molecular layer or to Cu atoms embedded in the molecular layer.

3.8 Conclusion

One twofold-symmetric and ten structures devoid of mirror planes of (*R*)- and (*S*)-MA have been observed on Cu(110) either with LEED or STM. The appearance of a certain structure depends on the coverage as well as on the annealing temperature. The extend of order of the structures varies tremendously. Some structures studied with STM appeared in such small islands, that they have not been observed with LEED. On the other hand, four long-range ordered structures have been observed with STM. The detection of an ordered array in LEED requires a minimum island size of about 20nm. In addition, the observed LEED structures displayed different qualities. In particular the quality of the (1 2, −8 2) structure of (*R*)-MA was much below of the corresponding (*R,R*)-TA phase. For enantiopure TA the (1 2, −8 2) is the dominating overlayer at medium coverage (θ ∼0.16). But also the observed c(2 × 4) MA structure at θ= 0.25 has lower quality than the respective TA overlayer. Thus it seems as if the missing C_2 symmetry in MA results in a decreased quality of long-range order and increased variation of observed structures.

In the symmetric c(2 × 4) overlayer RAIRS measurements identified most molecules to be in a monomalate adsorption mode. In the chiral structures MA is adsorbed mainly as bimalate.

In STM the bimalate structures at low and medium local coverage (θ= 0.16) are attended by stripes and protrusions which are interpreted as reconstruction of the underlying Cu surface. In areas between different ordered structures isolated copper adatoms are identified directly! This is the first direct STM observation of adsorption-induced reconstruction on Cu(110) for butanedioic acids. It has neither been observed for TA nor SU and suggests a pronounced chirality transfer via the substrate, rather than by intermolecular hydrogen bonding.

Chapter 4

Racemic malic acid on Cu(110)

While in the last chapter the adsorption and self-assembly of enantiopure malic acid (MA) on Cu(110) was considered, this chapter treats racemic MA (*rac.*-MA). The observed results and structures of *rac.*-MA will be compared to TA as well as to enantiopure MA.

4.1 Coverage

As for enantiopure MA the adsorption of *rac.*-MA on Cu(110) results in a saturation of the XPS C1s signal and the C1s/Cu3s ratio is 0.55. Hence, the same amount of enantiopure and racemic MA can be deposited on Cu(110) at RT. The best-quality c(2×4) structure is found for *rac.*-MA also at a C1s/Cu3s ratio of 0.43. Consequently, the coverage assignment of enantiopure MA applies also for racemic MA, i.e. at a C1s/Cu3s ratio of 0.43 the absolute coverage is per definition θ=0.25 and the relative coverage is one monolayer (1ML). At saturation the ratio is 0.55 and the absolute and relative coverages are θ=0.32 or 1.28ML respectively.

Deposition of (*R,R*)-tartaric acid ((*R,R*)-TA) on Cu(110) results in a c(2×4) at θ=0.25. But further exposure leads there to the formation of a (4 1, 2 5) overlayer at a saturation coverage that is about 10% higher [45]. Such a behaviour is not observed for *rac.*-TA. Thus the coverage at saturation is 10% lower for *rac.*-TA than it is for enantiopure TA [71].

4.2 LEED patterns of *rac.*-MA

The denotation of *rac.*-MA overlayers uses a (m_{11} $\pm m_{12}$; m_{21} $\pm m_{22}$) matrix for the superposition of both mirror domains.

Only three different structures have been observed for *rac.*-MA in LEED. The diffraction patterns are shown in figure 4.1.

The preparation conditions including coverage, temperature and annealing time are listed in table 4.1 for all structures shown in figure 4.1.

All matrices represented in figure 4.1 and table 4.1 describe a symmetric structure. The (1 $\mp$1, 9 $\pm$5) overlayer (θ^{global}=0.188-0.20) in a) is produced by a 30min annealing at 348K. Further annealing of the (1 $\mp$1, 9 $\pm$5) structure at 373K results in a (1 $\pm$1, $-$5 $\pm$2) overlayer after 60min. The quality of this heating induced superstructure is rather low as can be seen from the blurred spots in the corresponding LEED pattern (b). The transition from (1 $\mp$1, 9 $\pm$5) to (1 $\pm$1, $-$5 $\pm$2) is accompanied by halving of the unit cell in [1$\bar{1}$0] direction. At higher global coverage of θ^{global}=0.25 a well ordered c(2×4) can be observed (c). During the annealing process the C1s/Cu3s ratio decreases from 0.55 to 0.44, indicative for the desorption of molecules probably from the second partially filled layer. However, XPS revealed that no carbon is produced by this heating process and therefore no molecules are decomposed (section 4.4).

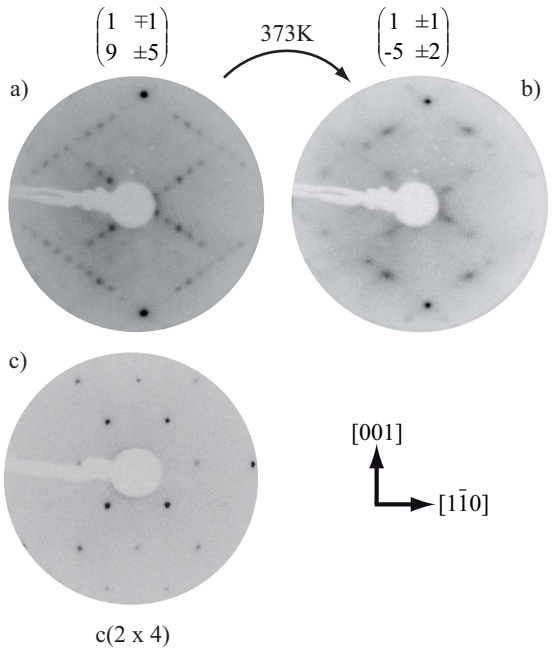

Figure 4.1: The three ordered superstructures observed for *rac.*-MA in LEED. The phase transition from $(1 \mp 1,\ 9 \pm 5)$ to $(1 \pm 1,\ -5 \pm 2)$ induced by thermal treatment is indicated. Electron energies in eV: a) 23; b) 26; c) 49.

Preparation conditions of observed LEED structures of *rac.*-MA			
Structure	θ^{global}	Annealing procedure	
$\left(\begin{smallmatrix}1 & \mp 1\\ 9 & \pm 5\end{smallmatrix}\right)$	0.188-0.20	30min / 348K	-
$\left(\begin{smallmatrix}1 & \pm 1\\ -5 & \pm 2\end{smallmatrix}\right)$	0.188-0.20	$\left(\begin{smallmatrix}1 & \mp 1\\ 9 & \pm 5\end{smallmatrix}\right)$ 60min annealed at 373K	
$c(2 \times 4)$	0.25	saturated monolayer 5min at 420K	

Table 4.1: The preparation conditions of observed *rac.*-MA LEED structures. Denotation follows the rules stated in [44].

In general it is surprising that only three ordered LEED structures could be found for *rac.*-MA. Apart from the c(2 × 4) overlayer no superstructure observed for enantiopure MA finds its analogy in the racemic MA structures. In this respect, MA/Cu(110) is different from TA/Cu(110). The (9 0, 1 2) (*R,R*)- and (9 0, −1 2) (*S,S*)-TA structures are observed when the racemate is deposited [72]. Even the procedure to create the c(2 × 4) overlayer differs from racemic to enantiopure MA (Table 4.2). This is a first indication, that *rac.*-MA forms heterochiral domains within the c(2 × 4) structure.

Comparison of preparation conditions of the c(2 × 4) structures		
Compound	Coverage θ	Annealing procedure
(*R*)-MA	0.25	5min at 348K
rac.-MA	0.25	saturated monolayer (θ=0.32) 5-7min at 430K

Table 4.2: The preparation conditions of the racemic and enantiopure c(2 × 4) structure are compared.

4.3 STM investigation of *rac.*-MA

Only five ordered overlayers were found for *rac.*-MA with the STM. The quality of these superstructures was in general very poor and two overlayers are rather due to an ordered reconstruction of the Cu(110) surface than due to self-assembly of molecules.

(3 ∓2, 3 ±4) overlayer

Figure 4.2 shows an STM image of the (3 ∓2, 3 ±4) overlayer, prepared by 120min heating at 393K. The two domains (green and red) have opposite handedness and cover rather small areas. The inset framed in green represents a section from the (3 −2, 3 4) structure, while the inset framed in red shows a section from the opposite handed (3 2, 3 −4) superstructure ((3 −2, 3 4)^M according to [44]). Since neither a (3 −2, 3 4) nor a (3 2, 3 −4) has been observed with enantiopure MA in LEED or STM measurements and since in STM three protrusions are visible per unit cell, it is assumed in the tentative models that these structures are formed by (*R*)- and (*S*)-MA molecules (green and red) in the ratio 2:1 or 1:2 respectively. The local coverage is θ^{local}=0.16. The brighter spot within the unit cell can be explained either by a buckling of the Cu surface or a monomalate adsorbate mode.

(1 ∓1, 9 ±5) overlayer

At a global coverage of about θ=0.19 and after 30min annealing at 348K the situation represented in figure 4.3 was found with STM. Lines of Cu atoms form ordered (1 −1, 9 5) and (1 1, 9 −5) structures. The height of the features identified as Cu atoms is always lower than zero ($\sim -0.4\mathring{A}$), while the height of the MA molecules inbetween the Cu atom lines is always higher than zero ($\sim +0.06\mathring{A}$). Furthermore, the distance between two maxima in the Cu lines amounts to $4.4\mathring{A}$, which is exactly the distance between two Cu atoms in the Cu(110) surface in $(1, \pm 1)$ surface direction. In the (1 −1, 9 5) the Cu lines are arranged in (1, -1) surface direction and coloured red in figure 4.3. The lines in the opposite handed (1 1, 9 −5) are green and oriented in (1, 1) direction. Between the rows of Cu adatoms MA molecules are located. These MA structures also display opposite chirality, although the ordering is not well extended in 2D (blue framed inset in figure 4.3). Hence it is assumed that the observed (1 ∓1, 9 ±5) LEED structure corresponds to the lines of reconstructed Cu atoms. Since such a severe reconstruction of the Cu surface has

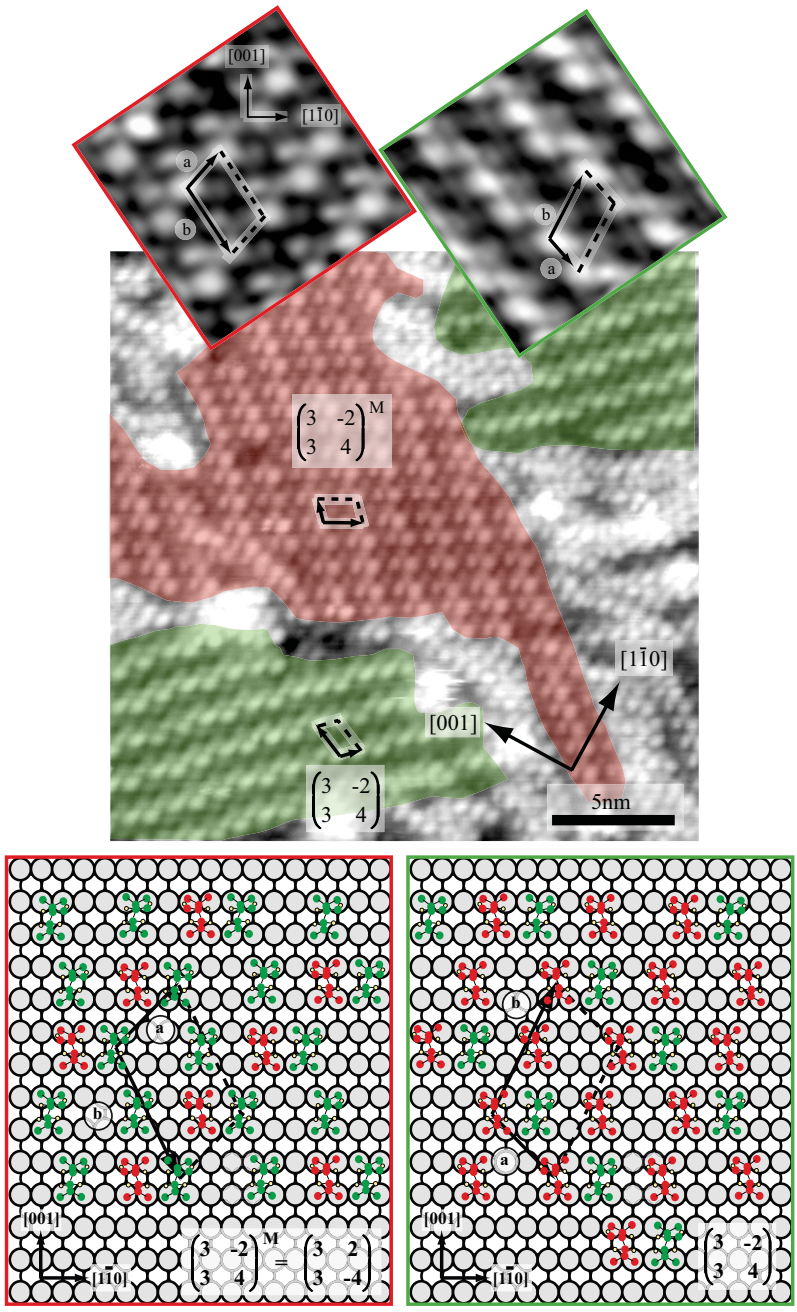

Figure 4.2: STM image of the racemic $(3\ \mp 2,\ 3\ \pm 4)$ overlayer and tentative models. The $(3\ -2,\ 3\ 4)$ structure is represented in the green islands, while the $(3\ 2,\ 3\ -4)$ is formed in the red islands. The structures in the red and green domains have opposite handedness. The inset on the right represents a section from the $(3\ -2,\ 3\ 4)$ structure, while on the left a section from the opposite handed $(3\ 2,\ 3\ -4)$ superstructure is shown. U= -1.93V, I= 50pA. Insets: 5nm × 5nm, inverse FT.

not been observed for enantiopure MA, (R)- (green molecule) and (S)-MA (red molecule) are expected to be adsorbed as heterochiral pairs in these MA structures.

$(\mathbf{1}\ \mp\mathbf{1},\ \mathbf{3}\ \pm\mathbf{2})$ and $(\mathbf{1}\ \pm\mathbf{1},\ -\mathbf{5}\ \pm\mathbf{2})$

After 60min at 373K a transition from the $(1\ \mp 1,\ 9\ \pm 5)$ to the $(1\ \pm 1,\ -5\ \pm 2)$ structure was observed in LEED (section 4.2). As shown in figure 4.4, STM revealed the simultaneous formation of a $(1\ \mp 1,\ 3\ \pm 2)$ and a $(1\ \pm 1,\ -5\ \pm 2)$ structure after 60min annealing at about 383K. Different colours are used: $(1\ -1,\ 3\ 2)$ in red, $(1\ 1,\ 3\ -2)$ in green, $(1\ 1,\ -5\ 2)$ in blue and $(1\ -1,\ -5\ -2)$ in yellow. The $(1\ -1,\ 3\ 2)$ and $(1\ 1,\ 3\ -2)$ structures have opposite handedness . The same is true for the $(1\ 1,\ -5\ 2)$ and $(1\ -1,\ -5\ -2)$. All these structures are formed by lines of reconstructed Cu atoms. In the $(1\ \pm 1,\ -5\ \pm 2)$ pairs of (R)- and (S)-MA molecules in a bimalate mode are used in the tentative models.

c$(\mathbf{2}\times\mathbf{4})$

Figure 4.5 shows the STM image of one saturated monolayer racemic MA (θ=0.32) after 10min heating at about 420K. A well-ordered c(2×4) is observed on the entire surface. In the tentative models a homochiral and a heterochiral arrangement of monomalate is shown in a) and b). The different conditions to prepare a c(2×4) structure for enantiopure and racemic MA indicate that a heterochiral structure forms (Table 4.2).

Probably due to the small domain size not all racemic overlayers observed with STM could also be observed with LEED as indicated in table 4.3. The small size of domains might be ascribed to an increased surface reconstruction in the presence of racemic MA.

Comparison of observed LEED and STM structures of racemic MA				
LEED structure	STM structure	θ^{global}	θ^{local}	remark
-	$\begin{pmatrix} 3 & \mp 2 \\ 3 & \pm 4 \end{pmatrix}$	∼0.20	0.11	-
$\begin{pmatrix} 1 & \mp 1 \\ 9 & \pm 5 \end{pmatrix}$	$\begin{pmatrix} 1 & \mp 1 \\ 9 & \pm 5 \end{pmatrix}$	0.188-0.20	-	reconstructed Cu(110)
-	$\begin{pmatrix} 1 & \mp 1 \\ 3 & \pm 2 \end{pmatrix}$	0.188-0.20	-	reconstructed Cu surface
$\begin{pmatrix} 1 & \pm 1 \\ -5 & \pm 2 \end{pmatrix}$	$\begin{pmatrix} 1 & \pm 1 \\ -5 & \pm 2 \end{pmatrix}$	0.188-0.20	-	reconstruction of surface
c(2×4)	c(2×4)	0.25	0.25	-

Table 4.3: Comparison of observed LEED and STM structures of racemic MA. Global and local coverages are indicated

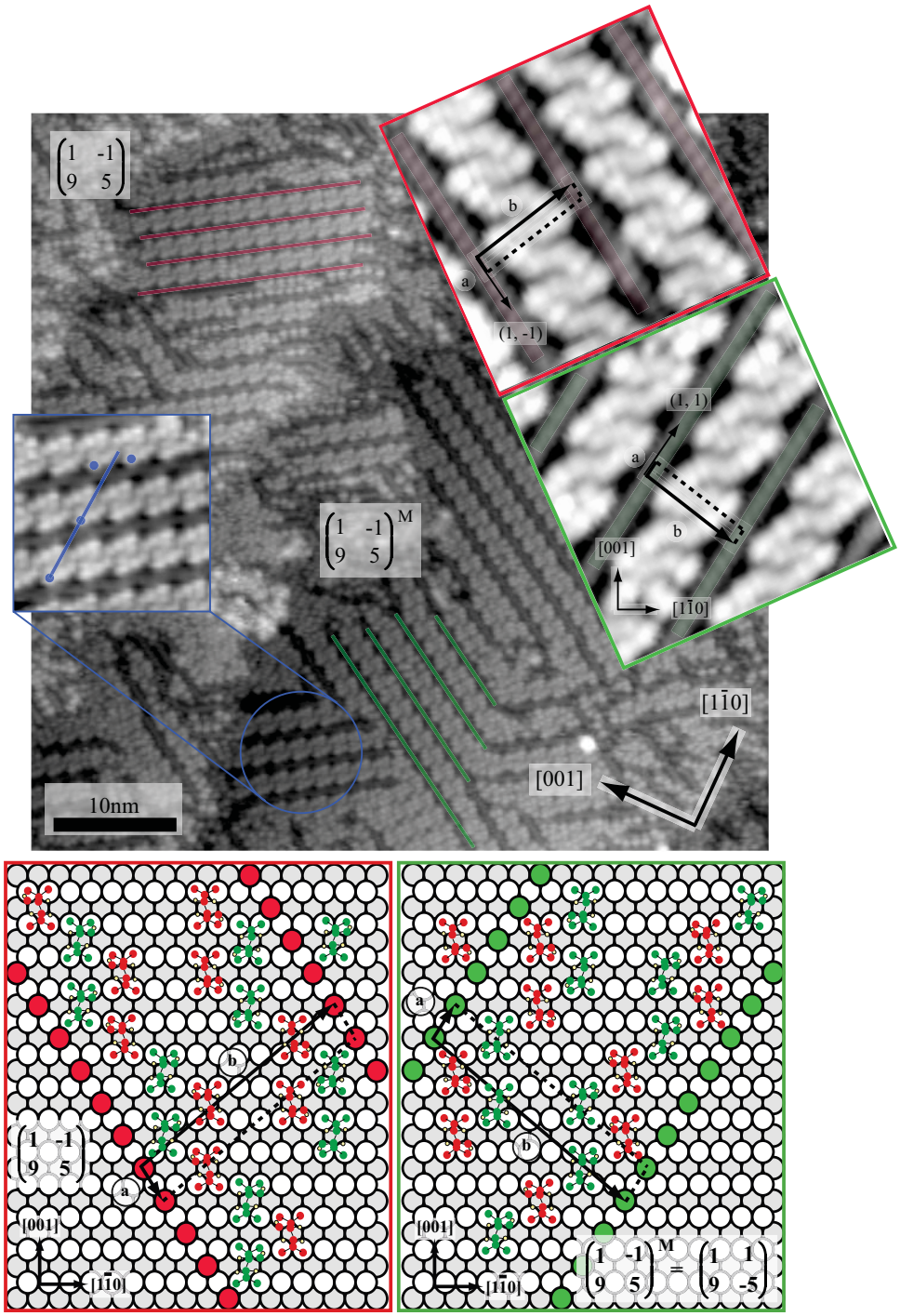

Figure 4.3: Reconstructed Cu atoms form ordered $(1\ -1,\ 9\ 5)$ (red lines) and $(1\ 1,\ 9\ -5)$ (green lines) structures with opposite handedness. The insets show the reconstruction in greater detail, whereat the red framed blow-up depicts the situation in the $(1\ -1,\ 9\ 5)$ superstructure and the green framed inset the $(1\ 1,\ 9\ -5)$ overlayer. Between the lines of reconstructed Cu atoms MA molecules are adsorbed in (1, -1) and (1, 1) surface direction. These opposite handed MA structures are not adsorbed in a long-range ordered 2D array (blue framed inset). Tentative models: (*R*)-MA is represented by green molecules and (*S*)-MA by red ones. U= -1.93V, I= 50pA. Insets: 7nm × 7nm (red and green), 9nm × 9nm (blue).

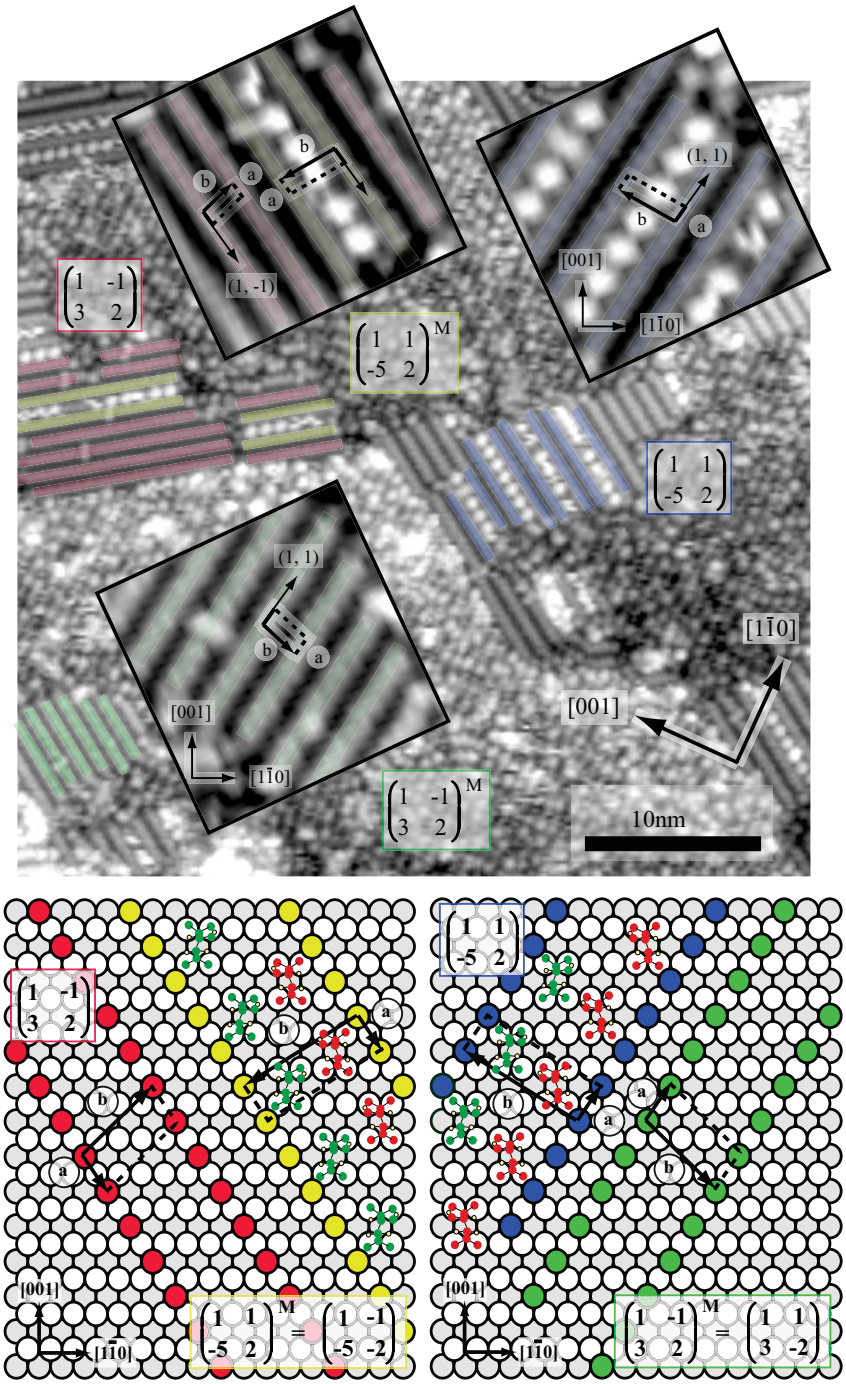

Figure 4.4: A $(1\ \mp 1,\ 3\ \pm 2)$ and a $(1\ \pm 1,\ -5\ \pm 2)$ structure are formed after 60min annealing at 383K. The structures are established by lines of reconstructed Cu atoms. Colour code: $(1\ -1,\ 3\ 2)$ in red, $(1\ 1,\ 3\ -2)$ in green, $(1\ 1,\ -5\ 2)$ in blue, $(1\ -1,\ -5\ -2)$ in yellow. Tentative models: (R)-MA represented by green molecules and (S)-MA by red ones. U= -2.0V, I= 50pA. Insets: 6nm × 6nm.

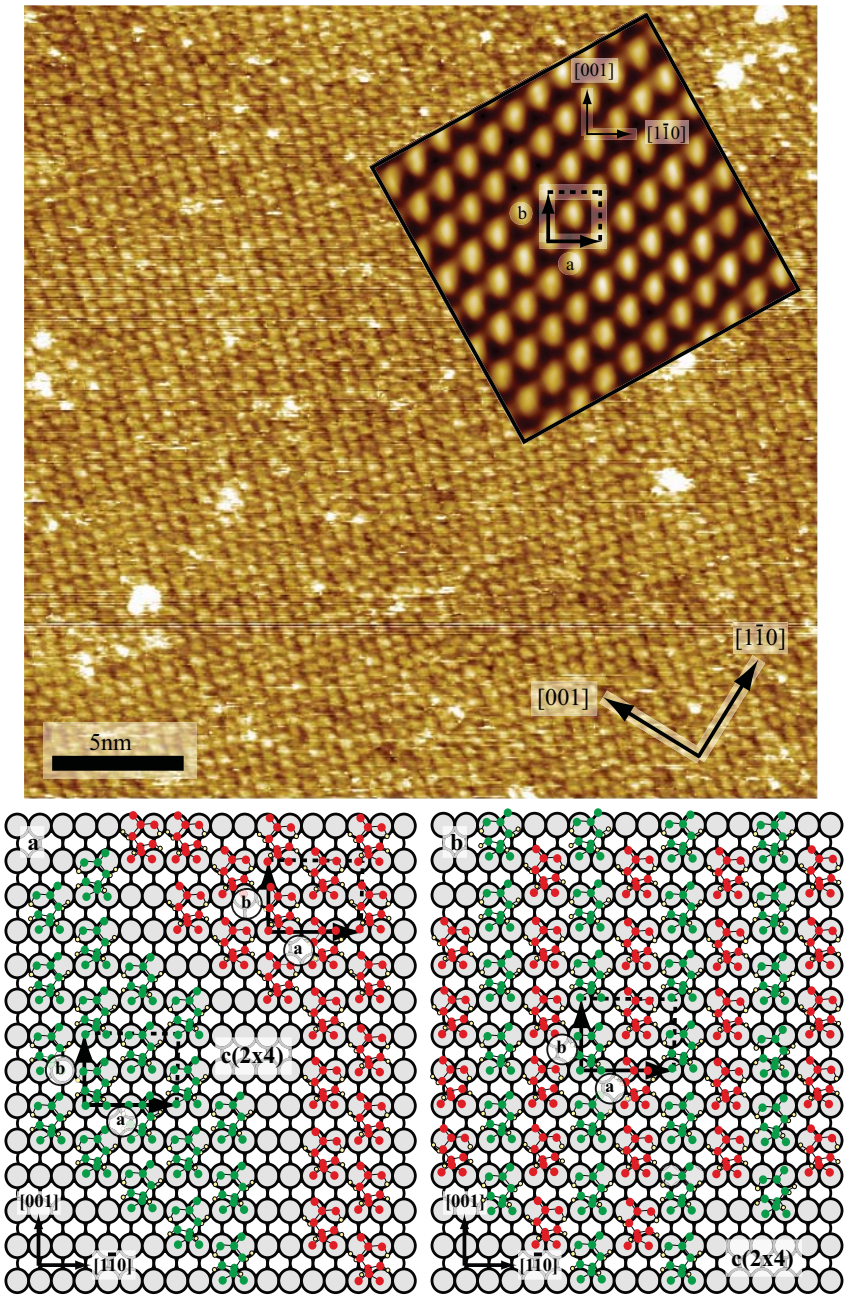

Figure 4.5: c(2 × 4) of *rac.*-MA. Homochiral (a) and heterochiral (b) arrangement of MA in the monomalate mode. U= +1.74V, I= 70pA. Inset: 5nm × 5nm, averaged 100×, inverse FT.

4.4 XPS measurements of *rac.*-MA

Figure 4.6 shows fits for different coverages of *rac.*-MA. As for enantiopure MA it was assumed that annealing at medium coverages results in a bimalate species, while a monomalate configuration is assumed at high coverages. A ratio of 2 (COO^-) : 1 ($CH(OH)$) : 1 (CH_2) was used for fitting the bimalate spectrum and four peaks with equal area ($COOH$, COO^-, $CH(OH)$ and CH_2) for the monomalate signal.

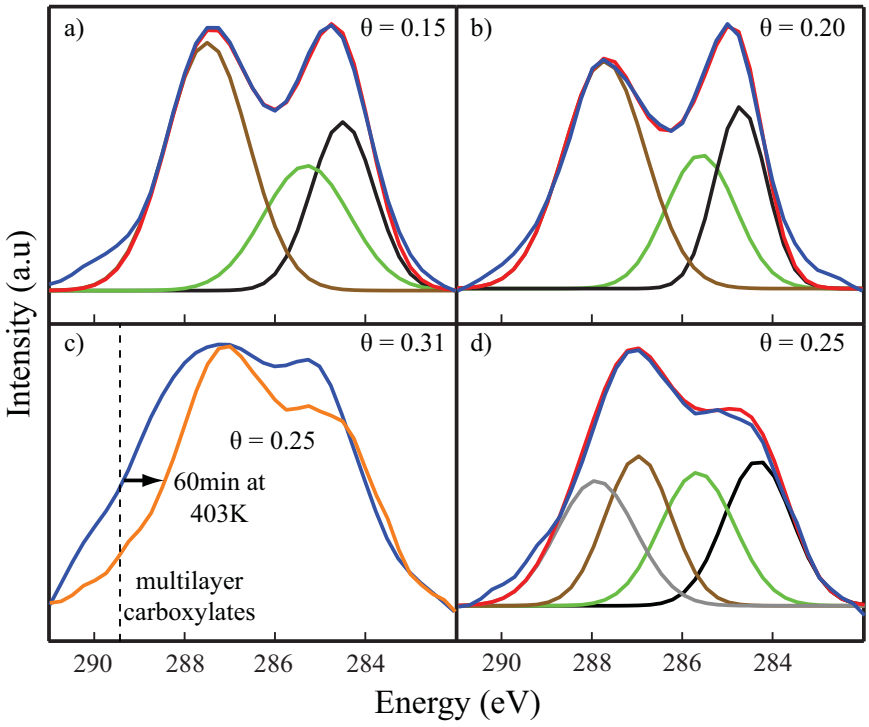

Figure 4.6: C1s signals for *rac.*-MA at different coverages. Measured data are displayed in blue and the fits are red. a) ∼47% of a saturated monolayer *rac.*-MA adsorbed on a hot crystal at 373K. A bimalate adsorption mode is assumed for the fit. b) Spectrum at higher absolute coverage of $\theta^{global} = 0.20$ after prolonged annealing (60min at 348K). The fit is again made for a bimalate adsorbate mode. c) Comparison of a saturated monolayer spectrum at RT (blue) and corresponding spectrum of a c(2 × 4) structure at $\theta^{global} = 0.25$ (orange). The fit of the c(2 × 4) structure is shown in d). In this case MA is expected to be adsorbed as monomalate. The c(2 × 4) was prepared by a extended heating of the saturated monolayer at high temperature (60min annealing at 403K).

The fits represented in figure 4.6 are listed in table 4.4. Peak energies and FWHM's (in parentheses) are indicated in eV. As for (*R*)-MA in section 3.3 the values from the fits are compared to values from the literature.

The C1s spectrum in a) was recorded for *rac.*-MA deposited directly on a hot crystal at 373K. The absolute coverage θ^{global} is 0.15. In the fit a bimalate mode is assumed. The coverage in b) is slightly higher and amounts to $\theta = 0.20$. This spectrum corresponds to the $(1 \mp 1,\ 9 \pm 5)$ LEED pattern created by 60min annealing at 348K (section 4.2). As before MA is expected to be adsorbed as bimalate. The comparison of a saturated monolayer at RT (blue) and the C1s signal from a c(2 × 4) superstructure (orange) is represented in c). The c(2 × 4) was produced

Fits of *rac.*-MA spectra in figure 4.6				
Coverage / system	$CH(OH)$	COO^-	$COOH$	$-CH_n$ $(n = 1, 2, 3)$
0.15	285.3 (2.2)	287.5 (2.2)	-	284.5 (1.6)
0.20	285.6 (1.8)	287.7 (2.1)	-	284.7 (1.3)
0.25	285.7 (1.9)	287.0 (1.7)	288.0 (2.1)	284.4 (1.7)
bi-(*R,S*)-TA [73]	286.5	288.0	-	-
bi-(*R,R*)-TA [73]	286.4	287.9	-	-
mono-(*R,S*)-TA [73]	286.2	287.7	288.6	-
mono-(*R,R*)-TA [73]	286.2	287.8	288.6	-
formic acid/Cu(110) [116]		287.7		
acetic acid/Cu(110) [117]		288.2		285.0
glycine/Cu (polycryst.) [118]		288.2		286.2
cysteine/Cu (polycryst.) [119]		288.6		286.1

Table 4.4: The C1s binding energies and full-width-at-half-maximum (FWHM) in parentheses in eV obtained from peak fitting of XPS curves represented in figure 4.6. At low coverage a bimalate adsorbate mode is assumed after annealing. At θ=0.25 MA is assumed to be adsorbed as monomalate. Values from the literature are also listed.

from the saturated monolayer by prolonged heating at elevated temperature (60min at 403K). During this annealing procedure the C1s/Cu3s ratio decreased from 0.55 to 0.44, indicating the desorption of molecules from the partially filled second layer (section 3.2). Compared to the saturated monolayer spectrum the c(2×4) signal is shifted to lower binding energy (displayed by an arrow). This is again a sign for desorption from the second layer, since these molecules are expected to contribute to a high energy shoulder representing multilayer carboxyls at ∼289.5eV (dashed line, section 3.3). In d) a fit of the c(2×4) is shown. As for pure MA a monomalate adsorption mode is expected in this structure. The carboxyl binding energy is only slightly higher than the binding energy of the carboxyl groups in a) and b), while the $CH(OH)$ binding energy is approximately the same for all of these three spectra (Table 4.4). This points to a bimalate contribution in c(2×4) XP spectrum. Hence as for enantiopure MA it can be concluded that the assumption of bimalate at low coverage and moderate annealing and monomalate at high coverage indeed allows to fit the respective spectra, but also for *rac.*-MA perfect overlayers with only one adsorption mode are difficult to prepare.

XP spectra of enantiopure and racemic MA are very similar at equal coverage and same adsorption mode as can be seen from the comparison of *rac.*-MA and (*R*)-MA spectra in table C (appendix C).

4.5 UP spectra of *rac.*-MA

The c(2×4) (θ=0.25) and saturated monolayer UP spectra (θ=0.32) of *rac.*-MA and (*R*)-MA are compared in figure B (appendix B). As in the case of enantiopure MA the influence of coverage and ordering on the UP spectra is also low for *rac.*-MA. The c(2×4) spectra and the saturated monolayer signals of racemic and enantiopure MA are similar. Hence UPS in general is not a good means to differ between enantiopure and racemic MA on Cu(110).

4.6 RAIR spectra of *rac.*-MA

In figure 4.8 RAIR spectra for *rac.*-MA at different coverages and temperatures are shown. The assignment of specific frequencies to vibrations follows section 3.5.

In a) the absolute coverage is 0.19. This spectrum is dominated by monomalate as shown by $\nu^{C=O}$ at $1694cm^{-1}$ and ν_S^{OCO} at $1431cm^{-1}$. But there is probably also a bimalate contribution indicated by ν_S^{OCO} at $1419cm^{-1}$. The $\nu^{C=O}$ band is composed of at least three peaks at $1694cm^{-1}$, $1679cm^{-1}$ and $1654cm^{-1}$. There is no deformation vibration of the alcohol group observable at RT. As already proposed for enantiopure MA the absence of an alcohol δ^{OH} band can be explained either by a strong inter- or intramolecular hydrogen bonding or by the fact that this mode has only a small dipole moment component perpendicular to the surface in monomalate.

After 30min annealing at 383K the signal in b) was observed. The $\nu^{C=O}$ band around $1697cm^{-1}$ is considerably lower in intensity and quite broad. It might be an artefact of the measurement. The ν_S^{OCO} at $1431cm^{-1}$ has disappeared. Hence monomalate has transformed into bimalate during the annealing procedure. The newly evolved δ^{OH} band at $1392cm^{-1}$ is a further sign for a bimalate adsorption mode.

Adsorbing 1ML *rac.*-MA at RT on Cu(110) results in the spectrum shown in c). Only two bands at $1698cm^{-1}$ ($\nu^{C=O}$) and $1435cm^{-1}$ (ν_S^{OCO}) can be observed. The signal at $1435cm^{-1}$ has in addition a shoulder at $1418cm^{-1}$. While the ν_S^{OCO} band at $1435cm^{-1}$ represents monomalate, the small signal at $1418cm^{-1}$ represents a bimalate adsorption mode. Thus at θ=0.26 and RT MA adsorbs preferentially as monomalate.

30min heating at elevated temperature of 383K changes the situation. The $\nu^{C=O}$ band in d) is now split into two distinct signals at $1687cm^{-1}$ and $1654cm^{-1}$. The vibrations at $1687cm^{-1}$ and $1434cm^{-1}$ might again represent a monomalate adsorption mode, while the ν_S^{OCO} band at $1423cm^{-1}$ could stand for bimalate. The $\nu^{C=O}$ signal at $1654cm^{-1}$ is also observed in the spectra in a), but with lower intensity. In section 4.3 STM revealed severe Cu surface reconstructions after annealing of *rac.*-MA. These reconstructions explain the band at $1654cm^{-1}$ which is due to an unidente carboxylate formed by a carboxylic acid group as indicated in figure 4.7. Unidente carboxylates have $\nu^{C=O}$ in the region $1675-1575cm^{-1}$ and ν^{C-O} at $1420-1260cm^{-1}$ [125].

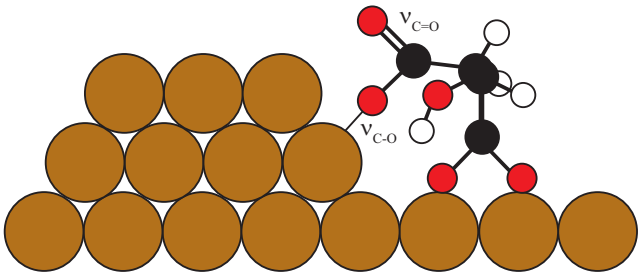

Figure 4.7: Monomalate bound to a reconstructed Cu surface forms an unidente carboxylate species. $\nu^{C=O}$ ($1675-1575cm^{-1}$) and ν^{C-O} ($1420-1260cm^{-1}$) should be detectable [125].

At saturation again only two peaks are observable at RT (e). There is no low wavenumber shoulder in the band at $1435cm^{-1}$. Together with the $\nu^{C=O}$ signal at $1697cm^{-1}$ it can be concluded that at saturation and RT *rac.*-MA adsorbs almost exclusively in a monomalate adsorption mode.

In f) the situation is shown after a short annealing at high temperature (5min at 420K). The coverage decreases from θ=0.32 at saturation to 0.25. In LEED a c(2×4) with good quality can be observed. The annealing procedure is manifested by a shift of $\nu^{C=O}$ to slightly lower wavenumber and the appearance of a shoulder at $1654cm^{-1}$ (reconstruction, unidente carboxylate) as well as

by the evolution of a band at $1424cm^{-1}$. Most molecules are here adsorbed as monomalate, but a small portion of bimalate molecules is also present on the surface. The coverage in the spectra in d) and f) is almost the same. Nevertheless, the different preparation conditions result in different situations. The "surface reconstruction band" at $1654cm^{-1}$ is stronger after extended annealing at moderate temperature (30min at 383K, d) than after a short tempering at high temperature (5min at 420K, f).

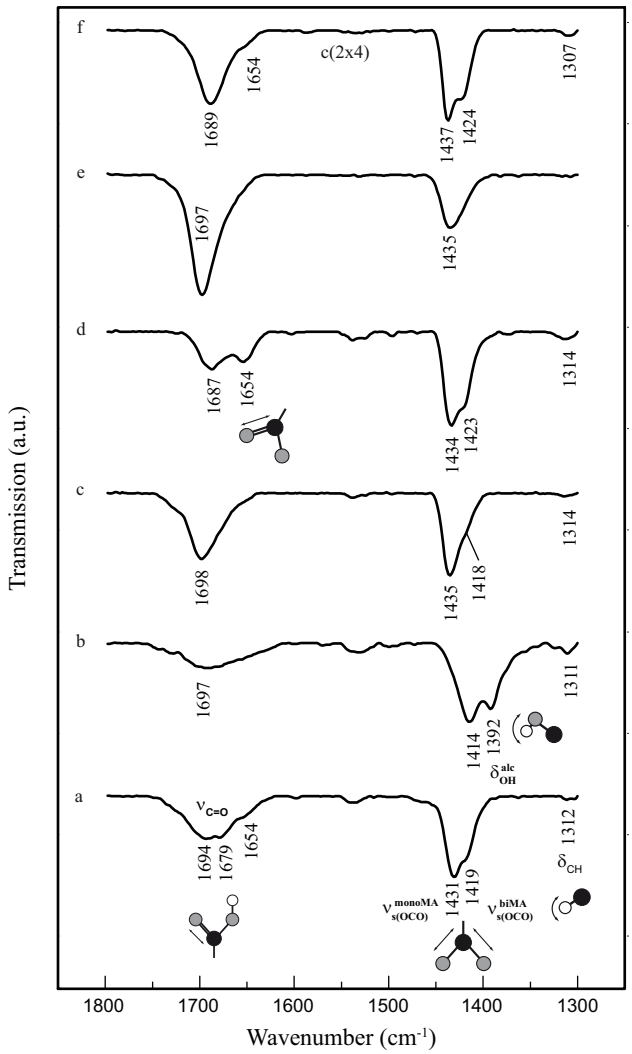

Figure 4.8: IR spectra showing the measured transmission of *rac.*-MA at different coverages and temperatures. a) θ=0.19 at RT. b) θ=0.19 after 30min at 383K. c) θ=0.26 at RT and in d) after 30min at 383K. e) θ=0.32 adsorbed at RT and then 5min annealed at 420K f). During heating at 420K the coverage decreases from θ=0.32 to 0.25.

In matters of the CH deformation band δ^{CH} (or wagging of the whole methylene group in the backbone (γ^{CH_2})) it can be concluded that this band becomes stronger after annealing as clearly observable in b), d) and f). Since annealing goes along with the transformation of monomalate to bimalate, the evolution of δ^{CH} depends also on the bimalate concentration.

The most striking difference between RAIR spectra of *rac.*-MA and (*R*)-MA structures is the shape of the $\nu^{C=O}$ band. In the case of enantiopure MA this band is narrow, while *rac.*-MA shows normaly a broad signal. Oscillations at $1654cm^{-1}$ have never been observed for pure MA. This suggests that surface reconstructon is more important for racemic MA.

4.7 Conclusion

Five ordered overlayers could be observed for racemic MA with LEED and STM, whereof three can be assigned to a severe reconstruction of the Cu(110) surface. Such a strong reconstruction has been observed neither for enantiopure MA, enantiopure TA nor racemic TA. It can be attributed to the simultaneous presence of both MA enantiomers on the surface. The quality of the observed structures is in general much lower than in the case of enantiopure MA. Only the racemic c(2×4) shows a better ordering than the enantiopure counterpart, probably due to a heterochiral arrangement of monomalate molecules.

Chapter 5

Thermal decomposition of MA on Cu(110)

In this chapter thermal decomposition of enantiopure and racemic malic acid (MA) is discussed. In order to reveal the underlying decomposition mechanism TPD, XPS and RAIRS are used.

5.1 TPD of enantiopure MA

Enantiopure (S)-MA was deposited on the clean Cu(110) crystal at RT and the crystal was heated up with a heating rate of β=4.1K/s. Decomposition of MA on Cu(110) leads to desorption of decomposition products like CO_2, CO, H_2 and H_2O. The same products have been observed for TA on this surface [71].

We observe two decomposition peaks in TPD for MA. Neither TA nor SU show more than one peak in the signals of their decomposition products [71, 75]. Figure 5.1 shows mass 44 amu TPD spectra corresponding to different deposition times (5min to 30min) and hence coverages. The low-temperature peak shifts strongly to higher temperature with increasing coverage. The saturated monolayer peak appears then at 512K, is intense and has a full width at half-maximum (FWHM) of only 2.3K. Hence enantiopure MA on Cu(110) is an example of so-called "surface explosion". Surface explosion was also observed for TA on Cu(110) [71], formic acid on Ni(110) [126, 127], acetic acid on Ni(110) [128] as well as for acetic acid coadsorbed with oxygen or carbon on various surfaces such as Rh(111) [129], Rh(110) [130] or Pd(110) [131, 132]. In a surface explosion the decomposition of adsorbed molecules is hindered since the surface coverage is at saturation and thus adjacent molecules inhibit the decomposition of each other. But at a certain temperature higher than the proper decomposition temperature of the respective molecules the decomposition starts at a certain point on the surface. This results in a gaining of catalytically avtive areas and consequently the molecules start to decompose at high rate.

The inset in figure 5.1 represents the second decomposition signal. This second peak does not shift and shows saturation already at low MA coverage. Compared to the first peaks they are rather broad (FWHM ∼37K). The peak-maximum temperature of the second peak is 571K.

In table 5.1 the integrated peak intensities and temperatures of the first (I_1, T_1) and second peaks (I_2 and T_2) are listed for the whole coverage range. The ratio $R = I_2/I_1$ of intensities is also indicated. The following facts can be deduced (time indications depend on temperature of evaporation cell, but the conclusions are only reliant on the specific coverage):

- After 15min deposition time the peak temperature of the first decomposition peak is almost stable. The same is true for the integrated peak intensities. Hence a saturated monolayer is reached after 10-15min evaporation.

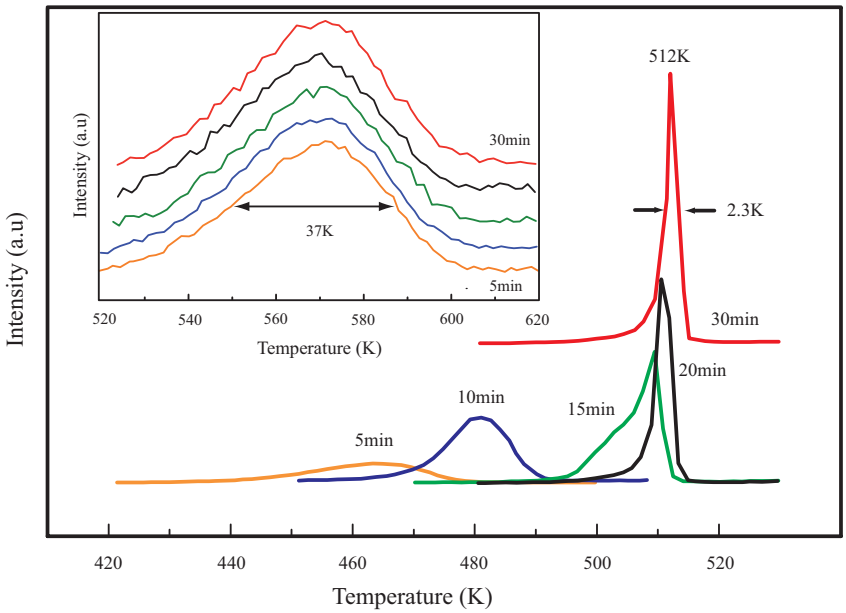

Figure 5.1: 44 amu signal with increasing initial coverages of MA. A shift to higher temperature and the small FWHM at saturation coverage (30min) are indicative for a surface explosion. The inset shows the second peak of the 44 amu signal. The peak temperature does not shift with coverage and is saturated at low MA coverage.

Peak intensities (I_1 and I_2) and temperatures (T_1 and T_2) of 44 amu					
Deposition time	I_1 (a.u.)	T_1 (K)	I_2 (a.u.)	$T_2(K)$	R
1min	1.0	453	1.0	574	1.0
2min	1.55	458	1.5	568	1.0
5min	4.9	463	4.4	571	0.9
10min	9.2	481	4.9	573	0.5
15min	9.7	510	4.9	571	0.5
20min	9.0	511	4.4	570	0.5
30min	9.7	512	4.1	571	0.4

Table 5.1: Integrated peak intensities (a.u., 44 amu) and peak temperatures in K of the first and second peak signals for various deposition times. The intensity ratios $R = I_2/I_1$ of first and second peak are also calculated.

- The intensity of the second peak seems to saturate already after 5-10min deposition.
- The peak intensities at saturation suggest that in the first decomposition step approximately twice as much CO_2 is produced than in the second step at 570K.

Our TPD set-up excludes that we detect desorbing molecules other than from the sample (e.g. the rods holding the sample).

The ratio of the 44 amu peak (CO_2) to the 28 amu peak (CO) is for both peaks significantly different. Assuming that the fragmentation process for CO_2 in the mass spectrometer is constant at these pressures, we come to the conclusion that CO is an intrinsic product of the second decomposition reaction, while the 28 amu signal in the first desorption peak is due to fragmentation of CO_2 in the mass spectrometer. Most likely, only CO_2 is formed in the surface explosion reaction at 513K.

Spectra corresponding to 2 amu, 44 amu and 28 amu signals at saturation are presented in figure 5.2. The absolute (S)-MA coverage in these experiments was always θ=0.32 at RT. It can be seen that all the first peaks appear at approximately the same temperature of 511K. The second peaks in the H_2 and CO_2 spectra have been blown up by a factor 4 and also these peaks have about the same peak temperature of ~570K. The area of the second peak in the 2 amu spectrum is approximately the half of the area under the first peak (1 vs. 2.2 in a.u.).

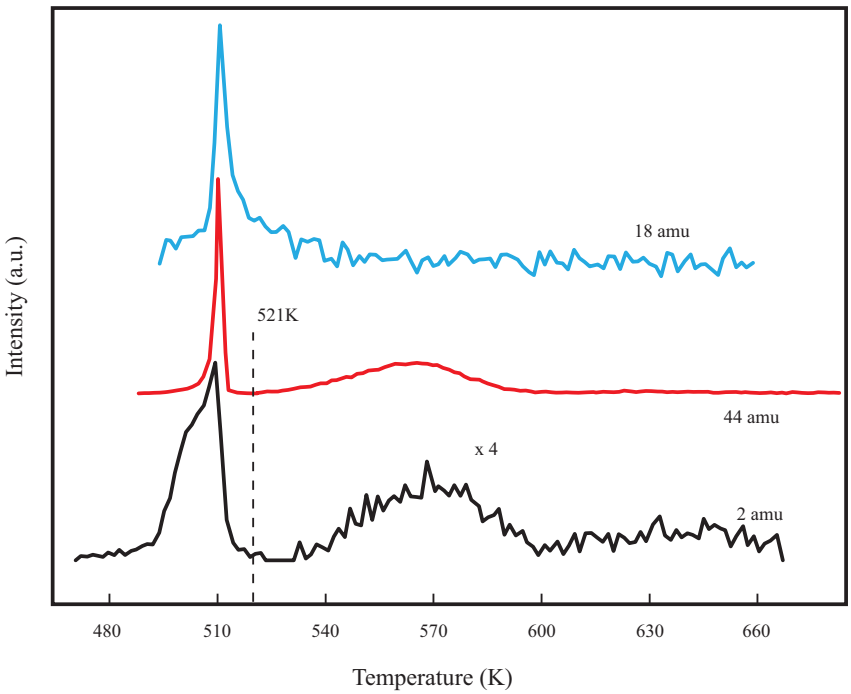

Figure 5.2: 2 amu, 18 amu and 44 amu spectra of a saturated (S)-MA monolayer are shown. The first and second peaks appear for all products at the same temperature. For H_2O no second peak is observed. The local minimum at 521K between first and second peak is also indicated. The spectra to the right of this minimum have been blown up by a factor 4.

The following table 5.2 sums up the decomposition of a saturated monolayer of enantiopure MA on Cu(110) and indicates which fraction of a certain signal (in percentage) is produced in the first and second TPD peak, e.g. 66% of the total CO_2 signal originates from the first peak and only 33% from the second one.

Decomposition products of a saturated MA monolayer				
peak	CO_2	CO	H_2O	H_2
peak 1	66%	-	100%	66%
peak 2	33%	100%	-	33%

Table 5.2: Decomposition of a saturated monolayer of pure MA with declaration of percentage.

Adsorption of (*S*)-MA on a hot crystal at 373K did not alter the observed results, i.e. the 44 amu spectrum still showed two peaks and the ratio of first and second peak intensity of a saturated monolayer was still 0.5.

5.2 TPD of racemic MA

Figure A in appendix A compares 44 amu TPD spectra of (*S*)-MA and *rac.*-MA. The peak maxima of the *rac.*-MA and (*S*)-MA show up at exactly the same temperatures. At full saturation coverage both the enantiopure and the racemic compound display a surface explosion. As for enantiopure MA the ratio $R = I_2/I_1$ of the integrated intensities of the first and second peak in a saturated monolayer spectrum is about 0.5 (Table A in appendix A). Hence it can be concluded that thermal decomposition of *rac.*-MA proceeds in essentially the same way as for enantiopure MA. In order to track the decomposition mechanism an enrichment experiment was conducted.

5.3 Thermal decomposition chemistry

The local minimum between the first and second peak in 44 amu TPD spectra appears at 521K (Figure 5.2). In order to enrich molecules and fragments after this decomposition step one saturated ML of racemic or enantiopure MA was deposited at RT on the crystal. Subsequently the crystal was heated to 521K with a heating rate of β=4.1K/s. Afterwards another full monolayer was deposited and the crystal was again heated to the 521K. This cycle was repeated three times and after each annealing step the residuals on the crystal were either investigated with RAIRS or XPS. After the third cycle the crystal was heated to 800K in order to desorb the enriched second peak. Again, the remaining residuals were investigated by RAIRS or XPS. XPS revealed no significant differences in experiments with *rac.*-MA and enantiopure MA (appendix D). Therefore XPS and RAIRS results of *rac.*-MA are presented in the following.

5.3.1 XPS of O1s spectrum

In the enrichment experiment not only the C1s but also the O1s XP spectrum of each step was recorded. Thus in order to be able to assign certain peaks to a specific functional group, the O1s spectrum of a chiral (1 2, −8 2) (*R*)-MA overlayer (θ=0.16) was fitted after Shirley background subtraction as shown in figure 5.3. Since in the (1 2, −8 2) a bimalate mode is assumed for MA, the spectrum was fitted with peaks displaying areas in the ration 1 ($CH(OH)$) : 4 (COO^-). Table 5.3 summarizes the fit of the (1 2, −8 2) overlayer. The peak energies and FWHM's (parentheses) are indicated in eV and the fitted spectrum is compared to literature values.

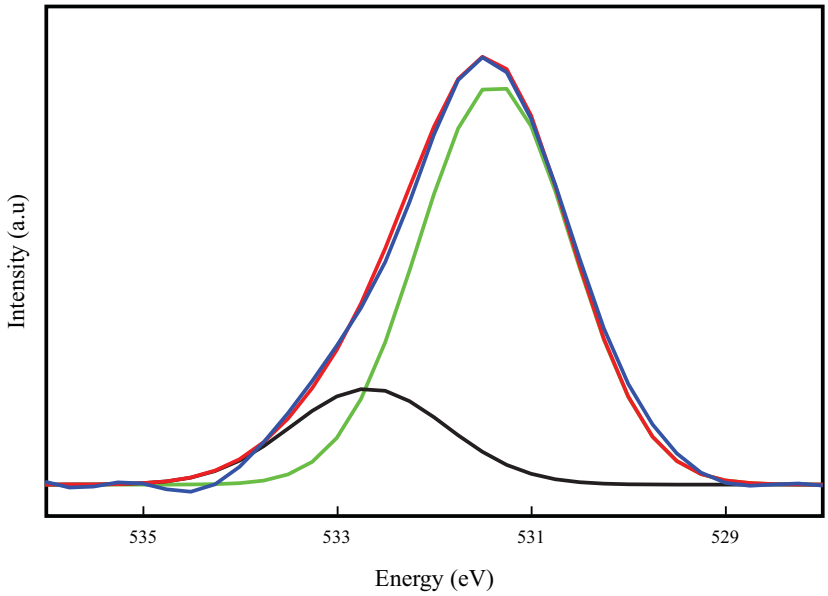

Figure 5.3: Fit (red curve) of the (1 2, −8 2) structure of (*R*)-MA at θ=0.16. The area ration of peaks is 1 ($CH(OH)$) : 4 (COO^{-}). A bimalate adsorption mode is assumed.

Fit of O1s peak of (*R*)-MA (1 2, −8 2) overlayer		
Coverage / system	$CH(OH)$	COO^{-}
0.16	532.7 (1.9)	531.4 (1.9)
Formic acid [116]	-	531.5
Acetic acid [122]	-	531.6

Table 5.3: Fit of the O1s peak of the (*R*)-MA (1 2, −8 2) overlayer. Peak energies and FWHM's are indicated and compared to values from literature.

5.3.2 Fits of C1s and O1s XPS signals

In figure 5.4 the C1s and O1s peaks corresponding to successive steps in the enrichment process are represented and the relative maxima in relation to the C1s and O1s peaks of a saturated monolayer at RT (a) are indicated. In b) peaks after three enrichment cycles and subsequent annealing to 521K are shown. The spectra in c) represent the residuals on the crystal after annealing to 800K.

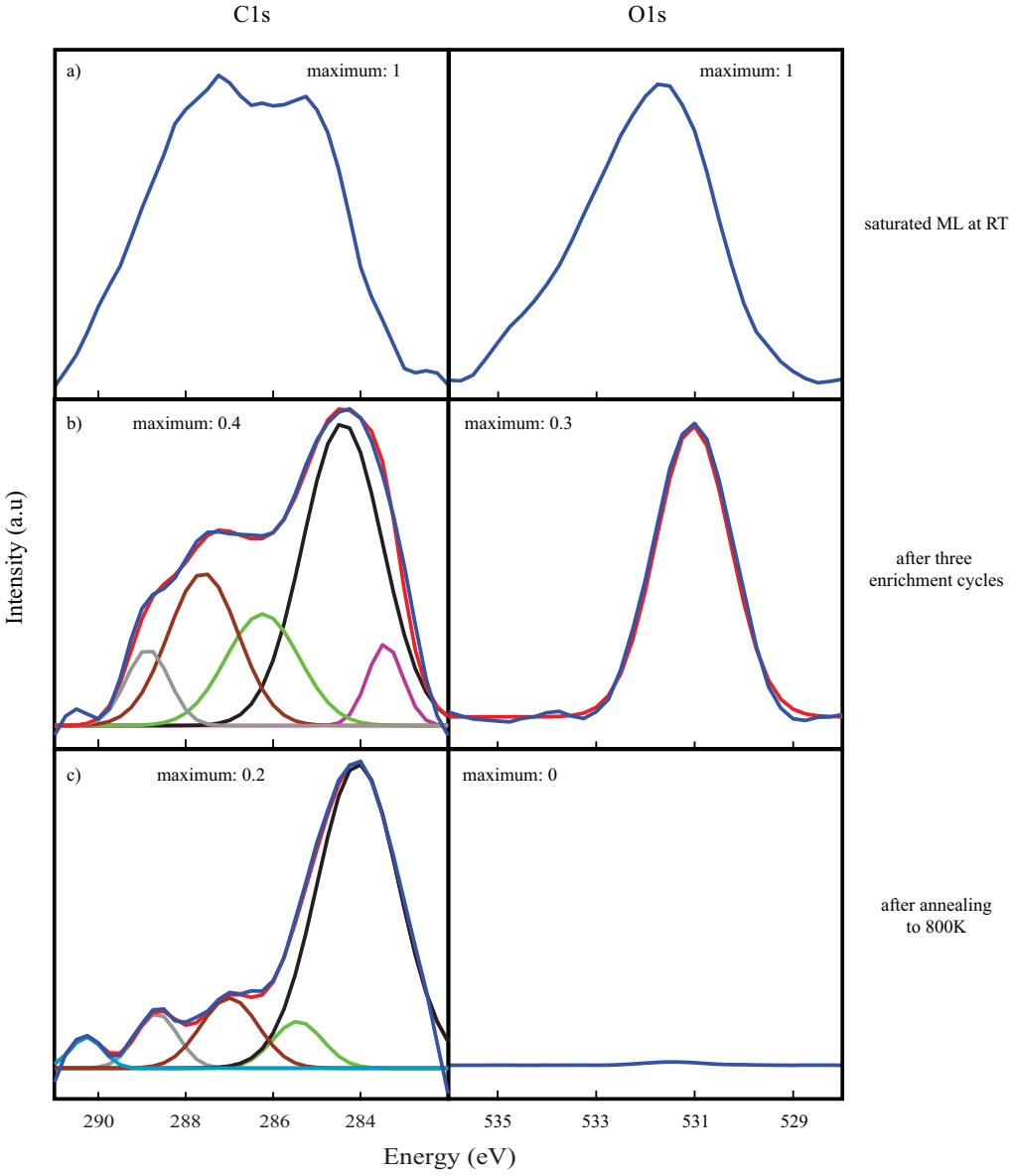

Figure 5.4: Fits for the C1s and O1s peaks of different steps in the enrichment experiment. a) Peaks corresponding to one saturated monolayer. b) Signals after three enrichment cycles (annealing to 521K). c) Residuals on the Cu(110) surface after annealing to 800K. Relative maxima compared to a saturated monolayer at RT are indicated.

The energies with FWHM's in eV and relative areas of the fit peaks are summed up in table 5.4. From the relative areas the (rounded) number of respective C atoms has been calculated in such a way, that the smallest fit peak corresponds to one carbon atom.

The small peak at 283.4eV after three enrichment cycles (b) is interpreted as residual carbon

Fit of C1s peak in enrichment experiment					
after three enrichment cycles and heating to 521K					
	$CH(OH)$	COO^-	$COOH$	$-CH_2$	graphite-like
Energy	286.2 (2.9)	287.6 (1.9)	288.9 (1.2)	284.4 (2.1)	283.4 (1.0)
relative area	0.35	0.43	0.14	1	0.12
number of C's	3	4	1	8	1
after heating to 800K					
	$CH(OH)$	COO^-	$COOH$	$-CH_2$	graphite-like
Energy	285.4 (1.3)	287.0 (1.6)	288.7 (1.1)	284.1 (2.2)	-
relative area	0.1	0.16	0.09	1	-
number of C's	1	2	1	11	-

Table 5.4: Peak energies and full-width-at-half-maximum (FWHM) in parentheses in eV obtained from peak fitting of the C1s peaks represented in figure 5.4. The relative areas in relation to the fit peak with largest area are also indicated. The assignment of peak energies to functional groups follows table 3.1 in section 3.3. The number of C's represents the relative areas and has been calculated in such a way that the fit peak with lowest relative area corresponds to one C atom. These numbers are rounded.

since its energy is lower than the CH_2 peak energy [90]. It is not visible anymore after annealing to 800K, probably due to the shift of the CH_2 peak to lower energy. In general, all the peaks shift to lower binding energy after heating to 800K, which could express the increased importance of the aliphatic moiety.

The situation is much clearer for the O1s peaks. Three enrichment cycles yield one single peak at 531eV (FWHM = 1.8eV), identified as COO^- (Table 5.3). Interestingly, the $CH(OH)$ peak observed in the C1s fit is not found in the O1s signal, where it should appear at ∼532.7eV according to table 5.3. Two reasons could explain this finding:

1. The COO^- and CH_2 peaks are broader than indicated in table 5.4, suggesting a general heterogeneity and disorder on the crystal. Such a situation is quite reasonable after a surface explosion. However, the small FWHM of the corresponding O1s signal contradicts this assumption.

2. The peak corresponding to $CH(OH)$ in the C1s fit is real. Yet, this group is oriented in such a way, that the carbon energy is almost not changed, while the O1s energy experiences a considerable down-shift to ∼531eV. Formic acid bound to Cu(110) by the hydroxyl group and its unidente carboxylate species are for instance expected to show the same C1s binding energies [116]. On the other hand, a CHO group that binds directly to Cu(110) by its oxygen atom should have almost the same O1s binding energy as a carboxylate group. Hence CHO and $CH(OH)$ should have the same C1s, but different O1s binding energies. Thus the assumption of $-CHO$ instead of $CH(OH)$ could explain the observed C1s and O1s spectra.

According to the O1s signal there is no oxygen left after heating to 800K. The corresponding C1s peak shows signals identified with COO^- and $COOH$. However, the relative C1s maximum is rather low (0.2) and thus the oxygen containing carbon peaks might be artefacts due to the background subtraction or the signal-to-noise ratio. In any case the dominant species adsorbed on Cu(110) after heating to 800K is plain carbon.

5.3.3 RAIRS

From XPS it is clear, that COO^- and CH_2 are present on the surface after heating to 521K. In order to get more informations about the presence of $CH(OH)/CHO$ and $COOH$, RAIRS experiments with (R)-MA were conducted. Figure 5.5 depicts spectra of different steps in the enrichment process. The assignment of bands follows section 3.5.

In a) the vibrations of a saturated monolayer are shown. The bands at $1700cm^{-1}$ ($\nu^{C=O}$) and $1435cm^{-1}$ (ν_S^{OCO} of monomalate) represent a monomalate adsorption mode, while the band at $1429cm^{-1}$ represents ν_S^{OCO} for bimalate. Obviously, at a saturated monolayer MA is adsorbed as both monomalate and bimalate.

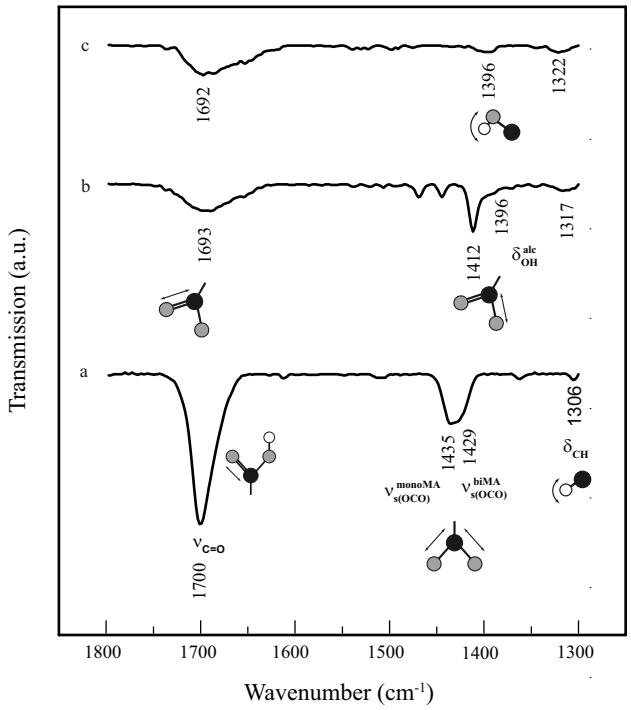

Figure 5.5: IR spectra of the enrichment experiment with (R)-MA. The transmission is represented as function of the wavenumber. a) Saturated monolayer of enantiopure MA ($\theta = 0.32$) deposited on Cu(110). b) Spectra after three enrichment cycles and heating to 521K. c) Vibrations corresponding to the residuals after annealing to 800K.

After three enrichment cycles a broad band appears in b) at $1693cm^{-1}$ and a narrow one at $1412cm^{-1}$. The $1412cm^{-1}$ signal could be identified as ν_S^{OCO} for bimalate and ν^{C-O} in CHO. The vibrations at $1693cm^{-1}$ might represent $\nu^{C=O}$. Heating to 800K results in the disappearance of the ν_S^{OCO} signal at $1412cm^{-1}$ in c). However, the broad band at $1692cm^{-1}$ ($\nu^{C=O}$) is still there, although according to XPS there is no oxygen left. Hence the signal at $1693cm^{-1}$ is probably an artefact. An unidente adsorption mode of MA would result in a $\nu^{C=O}$ at $1675 - 1575cm^{-1}$ and a ν^{C-O} at $1420 - 1260cm^{-1}$ and could therefore also explain the broad signal [125].

At $1396cm^{-1}$ a shoulder is visible in b) that could express a deformation mode of the alcohol δ^{OH}. But again, this mode is still visible after annealing to 800K (c) and therefore it might also be an artefact of the measurement. A δ^{CH} (or γ^{CH_2}) emerges at $1317cm^{-1}$. Compared to the saturated monolayer at RT this vibration is now stronger. Hence a re-orientation of the molecule or the CH groups might account for the increased adsorption of IR light.

Figure 5.6 shows the bands observed in the region $3060 - 2600cm^{-1}$. Three oscillations are

visible at $2864cm^{-1}$, $2929cm^{-1}$ and $2967cm^{-1}$ for a saturated monolayer at RT (a). After three enrichment cycles these bands are still there (b). Heating to 800K results in the disappearance of the $\sim 2860cm^{-1}$ band, while the other two oscillations are excited (c). Since XPS can not detect oxygen on the surface anymore after heating to 800K, the low-wavenumber bands at $\sim 2860cm^{-1}$ are probably related to oxygen. Hence they might represent ν_{CH} in the $CH(OH)/CHO$ group. This assignment is supported by CHO showing a ν_{CH} signal at $2900-2800cm^{-1}$ [125]. The bands at wavenumbers $> 2900cm^{-1}$ hence represent ν_{CH2}. In a succinic acid crystal two oscillations at $2980cm^{-1}$ and $2930cm^{-1}$ were identified as ν_{CH2}^{asym} and ν_{CH2}^{sym} [75]. Consequently, the band at $\sim 2967cm^{1-}$ might be due to ν_{CH2}^{asym} and the signal at $\sim 2930cm^{1-}$ due to ν_{CH2}^{sym}. However, the detection of ν_{CH2}^{asym} requires the CH_2 group to be oriented asymmetrically with respect to the surface normal. No shift of the CH bands is observed after annealing to 521K or 800K suggesting that no $C=C$ bond is created during the annealing procedure.

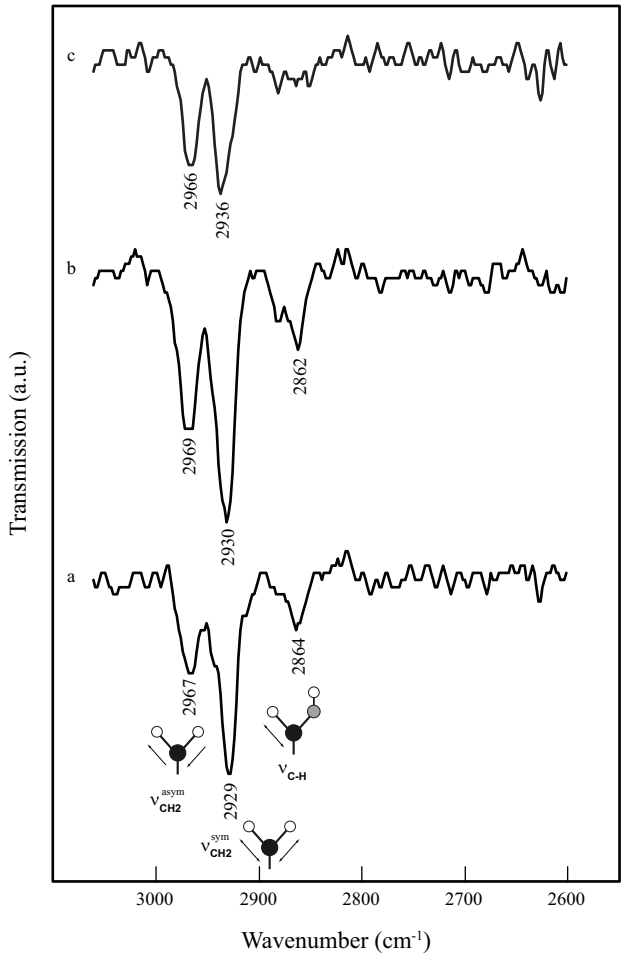

Figure 5.6: IR spectra of the enrichment experiment with (R)-MA in the region $3060-2600cm^{-1}$. The transmission is represented as function of the wavenumber. a) Saturated monolayer of enantiopure MA ($\theta = 0.32$) deposited on Cu(110). b) Spectra after three enrichment cycles and heating to 521K. c) Vibrations corresponding to the residuals after annealing to 800K.

Hence, from the RAIRS measurements follows:

- After enrichment and annealing to 521K carboxylate from bimalate is observed on Cu(110), as well as CH groups.

- Heating to 800K results in the disappearance of any ν_S^{OCO} vibration. The δ^{CH} vibration is excited with low intensity.
- There is no evidence for the formation of a double bonded $C = C$. A CH_2 group oriented asymmetrically with respect to the surface normal is expected.

5.3.4 Decomposition mechanism

As mentioned in section 5.1 the eye-catching difference between TPD experiments with TA and MA is the appearance of two peaks in the 44 amu spectrum of MA. This difference might be explained by the unequal positions that the hydroxyl group of MA may have with respect to the Cu surface. In the energetically favorable configuration the OH group is adsorbed at C3 near the surface. The energy is lower by $\Delta E = 0.54$eV when the alcohol group is attached at C2 (subsection 3.1.2). Hence at RT, the Boltzmann statistic would favor the energetically preferred configuration by a factor of $e^{+0.54/0.026} \approx 10^9$. Therefore, this energy difference can not explain the two peaks, unless intermolecular interactions direct adjacent molecules in configurations with OH groups at different carbon atoms. In this explanation it is supposed, that monomalate adsorbs with equal probability either with hydroxyl group at C2 or C3. For convenience monomalate with hydroxyl group at C2 is called MoMA-C2 and MoMA-C3 when the alcohol group is at C3. Figure 5.7 shows the proposed decomposition mechanism:

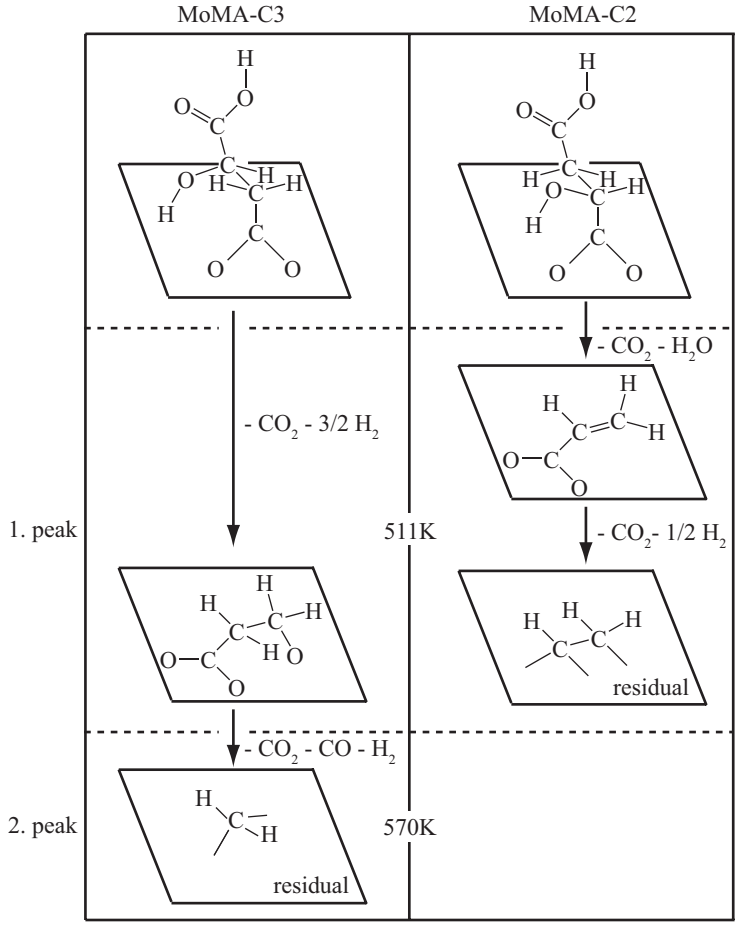

Figure 5.7: Proposed mechanism for the thermal decomposition of MA on Cu(110) based on XPS and RAIRS results. Starting point are monomalate species with hydroxyl group either at C3 (MoMA-C3) or C2 (MoMA-C2).

1. The decomposition of TA is assumed to start as soon as a $COOH$ group is brought in contact with the Cu(110) surface [71]. At 511K MoMA-C3 splits of CO_2 and H_2. The resulting product is bound to the surface by a carboxylate group and the remaining oxygen atom from the hydroxyl group. As in the case of bimalate, this three point bonding causes strain in the molecular backbone that results in a ν_S^{OCO} band at $1412cm^{-1}$. MoMA-C2 first releases CO_2, H_2O and H_2. The residual product is a carbon species bound to the surface. Hence in the first decomposition step 3 CO_2, 1 H_2O and 2 H_2 is produced. These products are also observable with the mass spectrometer. The ratio between COO^-, CHO and CH_2 in the products of the first decomposition step is 1 : 1 : 3. According to XPS it should be 1 : 1 : 2 (Table 5.4). As already mentioned above, the bonding of the remaining oxygen atom from the hydroxyl group in $CH(OH)$ to the surface (CHO group) could lead to a down-shift of the respective O1s binding energy and explain why only one peak is visible in figure 5.4b).

2. In the next step the MoMA-C3 product releases 1 CO_2, 1 CO and 1 H_2 at 570K, CH_2 is left on the surface. No H_2O is produced. Hence three times as much CO_2 and twice as much H_2 is produced in the first decomposition step than in the second one. The ratio should be 2 : 1 both for CO_2 and H_2 (Table 5.2). As observed with XPS there is no oxygen left on the surface within this model. The main residuals are carbon species.

The presented model can explain the experimentally observed results quite well both quantitatively and qualitatively. However, it is based on the assumption of two different monomalate species (MoMA-C2 and MoMA-C3) in the ratio 1 : 1 as starting point. In order to really validate this model calculations are needed to explain why monomalate should be adsorbed in both energetically unequal configurations.

5.4 TPD of symmetric $(1 \mp 1,\ 9 \pm 5)$ and c(2×4) structures

For *rac.*-MA a symmetric $(1 \mp 1,\ 9 \pm 5)$ has been observed. The corresponding XPS spectrum and LEED pattern are shown in section 4.4 and 4.2. Figure 5.8 shows TPD spectra of the achiral $(1 \mp 1,\ 9 \pm 5)$ (θ=0.20) and c(2×4) (θ=0.25) structures. The heating rate was again β=4.1K/s. The $(1 \mp 1,\ 9 \pm 5)$ overlayer results in three peaks at 481K, 567K and 642K. The third peak at 642K has even higher intensity than the second peak at 481K. When racemic TA is heated from RT to 800K without producing first an ordered layer, then only two peaks are observed in the TPD spectrum. At a coverage of $\theta \approx$0.20 these peaks appear at about 470K and 570K. Hence the wide difference is rather not given by the peak temperatures, but by the number of peaks. Obviously the heating procedure (30min at 348K) results in a situation that produces three peaks in TPD. In order to really exclude an influence of the heating procedures on the peak temperatures one would have to compare spectra at exactly the same coverage.

For comparison only two peaks are observed in the TPD of the c(2×4) with peak maxima at 510K and 567K. The TPD of 1ML *rac.*-MA deposited at RT on the Cu(110) crystal results also in two peaks at about the same temperatures. Therefore in this case the heating procedure to form the overlayer (one saturated monolayer adsorbed at RT, then 5min at 420K, thereby reduction form C1s/Cu3s=0.55 to 0.44) has no influence on the number of observed peaks. However, the discrepancy in the peak number can be explained by a reconstruction of the Cu surface as observed with STM for the $(1 \mp 1,\ 9 \pm 5)$ structure (section 4.3).

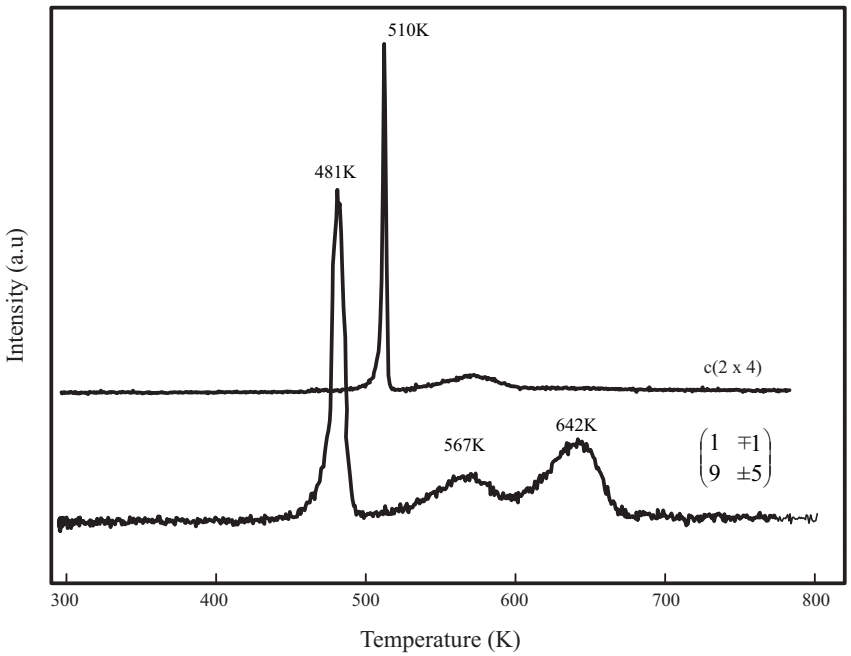

Figure 5.8: TPD spectra of the symmetric $(1\ \mp 1,\ 9\ \pm 5)$ and c(2×4) structures of *rac.*-MA. Peak maxima are indicated.

5.5 TPD of *rac.*-MA/(*R,R*)-TA mixtures

Figure 5.9 compares TPD spectra of different *rac.*-MA/(*R,R*)-TA mixtures with a pure *rac.*-MA spectrum. The percentage of (*R,R*)-TA is indicated as well as the observed LEED structure. The heating rate was again β=4.1K/s. Since the coverage in all spectra is within the region between θ=0.20 and θ=0.22, differences in TPD are expected to be due to the TA concentration.

At 17% (*R,R*)-TA concentration three peaks appear at 482K, 571K and 638K. The first peak shows the highest intensity and the third peak is more pronounced than the second one. Increasing the TA concentration to 32% has no strong influence on the spectra. There are still three peaks at almost the same temperatures (484K, 570K and 637K) and the sequence in peak intensity is still the same. But the second and third peak seem to be in general less pronounced. Further increasing the (*R,R*)-TA concentration to 72% results in four peaks at 493K, 511K, 569K and 637K. Obviously the first peak that appeares in the 17% and 32% TA spectra at ∼482K is now split into two peaks at 493K and 511K. The peak at 511K has the highest intensity in this spectrum. The high temperature peaks at 569K and 637K are quite weak. Hence, with increasing portion of TA the peaks at higher temperature show a small shift to lower values and become less intense. Therefore it can be stated that they originate from MA. This and also the fact that the first peak is split into two other peaks in the case of high TA concentration indicates, that TA shows its influence mainly in the first peak(s) at lower temperature.

As shown above, the achiral $(1\ \mp 1,\ 9\ \pm 5)$ structure of *rac.*-MA at θ=0.2 displays also three peaks in TPD at 481K, 567K and 642K. As in the case of low TA concentration the first peak has highest intensity and the third peak is stronger than the second one. The missing influence of TA is here probably seen in the different peak temperatures of the second and third peak as compared to the MA/TA mixtures. However, this distinction could also be explained by the

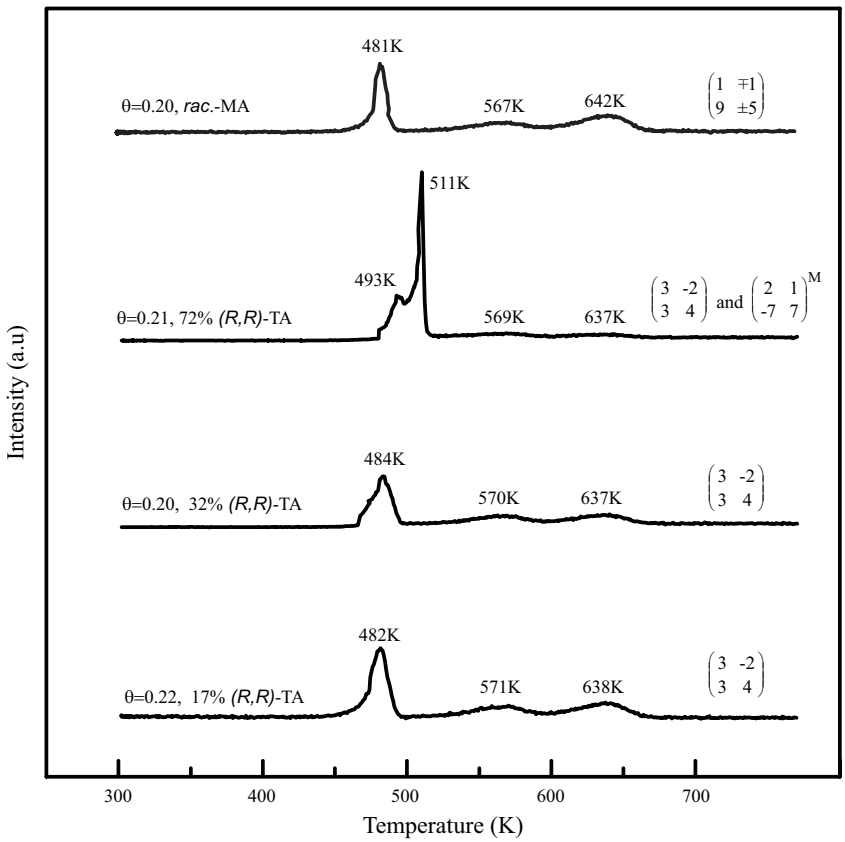

Figure 5.9: TPD spectra of *rac.*-MA/(*R,R*)-TA mixtures and pure *rac.*-MA. The absolute coverage and (*R,R*)-TA percentage are indicated as well as the underlying overlayer structure in LEED. The heating rate was β=4.1K/s.

observed overlayers ((1 $\mp$ 1, 9 $\pm$ 5) vs. (3 $-$ 2, 3 4)). The appearance of three peaks in the TPD of racemic MA was explained by a reconstruction of the Cu surface. This might also be the reason for three peaks in the *rac.*-MA/TA mixtures.

Chapter 6

Racemic tartaric acid mixed with malic acid

Doping SU with chiral TA allowed to introduce a single enantiomorphism in SU on the entire Cu(110) surface [78]. This effect is an example of the "sergeants-and-soldiers effect". Since SU is intrinsically achiral it has no preference and follows the "TA-sergeants". The question arises what happens if achiral SU is replaced by another chiral molecule, as for instance chiral MA. There might be something like a chiral conflict between TA and MA. In order to investigate such a potential conflict between chiral molecules, mixing experiments within the systems *rac.*-TA/MA and *rac.*-MA/TA have been conducted. During two-dimensional chiral conglomerate formation of tartaric acid on the Cu(110) surface in the system *rac.*-TA/MA, the growth of one enantiomorph is suppressed by the opposite chirality of a coadsorbed malic acid enantiomer, forming a quasi-racemic and semi-ordered solution. In the system *rac.*-MA/TA another mechanism is observed: A small chiral TA bias together with an energetically unfavorable situation imposed by the simultaneous existence of both MA enantiomers on the surface results in single enantiomorphism. These results will be presented in chapter 6 (*rac.*-TA/MA) and chapter 7 (*rac.*-MA/TA).

6.1 XPS of mixing experiment *rac.*-TA/MA

Figure 6.1 shows the C1s fits of 0.47ML racemic TA evaporated on a hot crystal at 383K (a) and of the mixture of 0.28ML *rac.*-TA and 0.29ML (*R*)-MA after 60min tempering at 358K (b). The spectrum in a) corresponds to an achiral (9 0, $\pm$1 2) structure in LEED and for the mixture in b) a (9 0, 1 2) was found. In both cases a doubly deprotonated adsorbate is expected in the fits. Hence the signal in a) has been fitted with two peaks with area ratio of 1 (COO^-) : 1 ($CH(OH)$). For the spectrum in b) three peaks with ratio 4 (COO^-) : 3 ($CH(OH)$) : 1(CH_2) have been used.

Table 6.1 lists the fits in figure 6.1. Peaks energies and FWHM's (in parentheses) are indicated in eV and compared to an enantiopure MA fit (θ=0.16, (1 2, $-$8 2) in LEED). All peaks are almost equal in binding energy, confirming the assumption that both TA- and MA-molecules are adsorbed in their doubly deprotonated bi-configuration (bitartrate, bimalate).

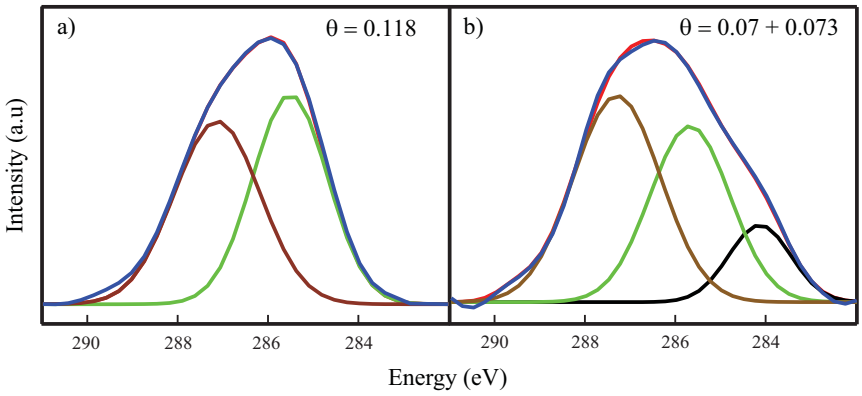

Figure 6.1: Fit (red) of the C1s signal (blue) of 0.47ML (θ=0.118) *rac.*-TA (a) and of the mixture of 0.28ML *rac.*-TA and 0.29ML (R)-MA (θ=0.07+0.073) (b). The racemic TA in a) was deposited on a hot crystal at 383K. The mixture in b) was annealed for 60min at 358K.

C1s fits of racemic TA and a 50% : 50% mixture of *rac.*-TA and (R)-MA					
Coverage	system	$CH(OH)$	COO^-	$COOH$	$-CH_2$
0.118	*rac.*-TA	286.1 (1.7)	287.6 (2.0)	-	-
0.143	*rac.*-TA + (R)-MA	285.7 (2.1)	287.3 (2.3)	-	284.2 (1.6)
0.16	(R)-MA	285.8 (2.1)	287.6 (2.2)	-	284.8 (1.7)

Table 6.1: Comparison of the C1s fits of racemic TA at a coverage of θ=0.118 adsorbed on a hot crystal at 383K, a 50 : 50 mixture of *rac.*-TA and (R)-MA (θ=0.143=0.07+0.073, 60min tempered at 358K) and enantiopure (R)-MA (θ=0.16, 5min at 343K). Full-width-at-half-maxima (FWHM's) are indicated in parentheses.

6.2 LEED results

The LEED pattern of 0.59ML *rac.*-TA adsorbed on a hot crystal at 373K and subsequently tempered for 60min at 353K is shown in figure 6.2a). An achiral (9 0, ±1 2) overlayer was observed. The influence of mixing racemic TA with enantiopure MA is shown in b) and c). After tempering 0.28ML *rac.*-TA and 0.29ML (*R*)-MA for 60min at 358K, LEED showed only a (9 0, 1 2) structure in b). Using approximately the same amount of opposite handed (*S*)-MA (0.27ML) instead of (*R*)-MA and 0.31ML *rac.*-TA resulted in a (9 0, −1 2) structure as shown in c). The spots corresponding to the TA compound with opposite handedness than MA are suppressed: (*R*)-MA suppresses the (9 0, −1 2) pattern of (*S,S*)-TA and (*S*)-MA the (9 0, 1 2) (*R,R*)-TA pattern. 25% of MA is enough to induce a single enantiomorphism. A lower MA concentration results in a (9 0, ±1 2) LEED pattern, where the spots corresponding to that TA compound with opposite chirality than the used MA are lower in intensity. A higher MA concentration than 75% leads to a pure MA structure.

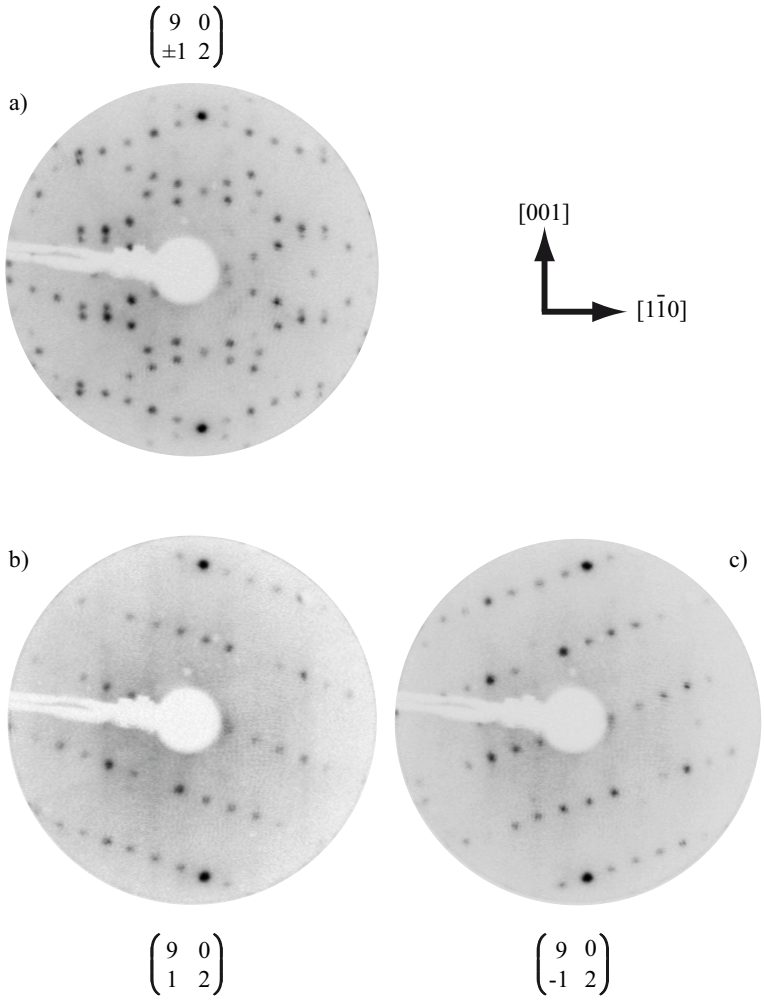

Figure 6.2: a) 0.59ML racemic TA adsorbed at 373K and further annealed for 60min at 353K. A (9 0, ±1 2) pattern is observed. b) 0.28ML *rac.*-TA and 0.29ML (*R*)-MA after 60min at 358K shows only a (9 0, 1 2) structure. c) 0.31ML *rac.*-TA and 0.27ML (*S*)-MA after 60min at 348K. A (9 0, −1 2) pattern is observed. Electron energies in eV: a) 25eV, b) 23eV, c) 23eV.

At a first glance, this effect is quite similar to that one observed in the sergeants and soldiers experiment with SU and TA. Doping with chiral TA eliminated one enantiomorph in the (9 0, ±1 1) SU layer [78]. Depending on the dopant either a (9 0, 1 1) ((*R,R*)-TA as dopant) or a (9 0, −1 1) (with (*S,S*)-TA) was observed. However, only 2% of TA was needed, while here it takes at least 25% of MA.

6.3 STM results

At a coverage of ∼0.6ML and after 45min heating at 373K racemic TA forms both structures on Cu(110) which are also observed for pure enantiomers (Figure 6.3a). Two domains with opposite handedness exist (marked in blue and red). The blue areas represent the (9 0, 1 2) (*R,R*)-TA domains. The red ones represent (*S,S*)-TA domains. In b) 0.22ML (*R*)-MA and 0.44ML *rac.*-TA had been annealed for 60min at 353K. No formation of large (9 0, −1 2) (*S,S*)-TA islands is observed, while large islands of the (9 0, 1 2) structure still exist. Hence MA suppresses the formation of large TA islands with opposite handedness. Apart from the ordered large (*R,R*)-TA domains and small (*S,S*)-TA islands, a large area is covered with molecules in low-ordered structures. This observation is very important in the explanation of the observed effect.

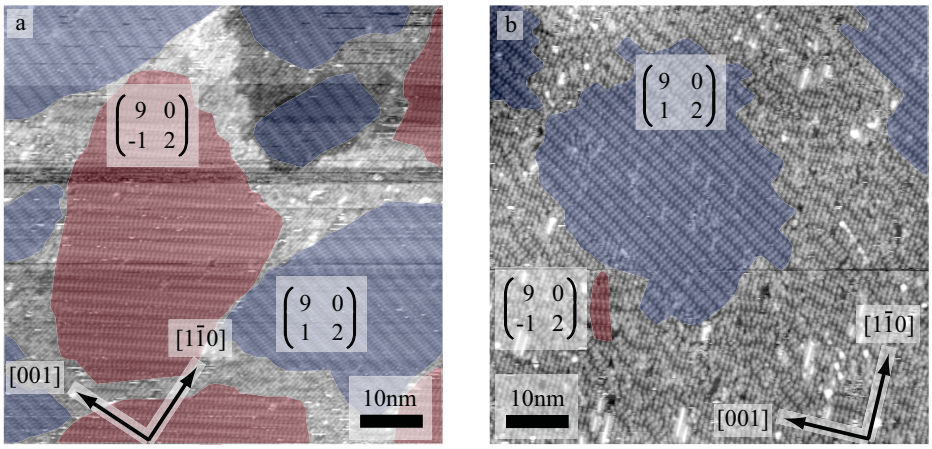

Figure 6.3: a) Racemic TA at a coverage of ∼0.6ML and after 45min heating at 373K. Two domains (blue and red) with opposite handedness are formed. (*R,R*)-TA builds the (9 0, 1 2) structure in the blue islands. The red domains represent the (*S,S*)-TA (9 0, −1 2) overlayer. b) 0.22ML (*R*)-MA and 0.44ML *rac.*-TA after 60min at 353K. (*R*)-MA suppresses the formation of large (9 0, −1 2) islands. Tunneling: a) U= -1.93V, I= 60pA, b) U= -1916mV, I= 65pA.

In figure 6.4 the coexistence of all phases is shown at a ratio of 90% *rac.*-TA and 10% (*R*)-MA. The red coloured (*S,S*)-TA domains are still of substantial size since the MA concentration is too low to suppress them. The green areas show examples where the molecules in the disorder are aligned along the [1$\bar{1}$0] direction (insets in figure 6.4). Quite often these molecules are adsorbed in triplets. The large inset shows a row of triplets intersecting a (9 0, 1 2) (*R,R*)-TA island.

The following other observations are in addition important for the origin of the proposed mechanism to explained the observed suppression effect:

1. Mixing experiments of (*R*)-MA either with only (*R,R*)- or (*S,S*)-TA reveal, that only at substantial excess of one species, ordered structures of the single species are observed. At equal ratio, however, no well-ordered structures have been seen. These mixing experiments

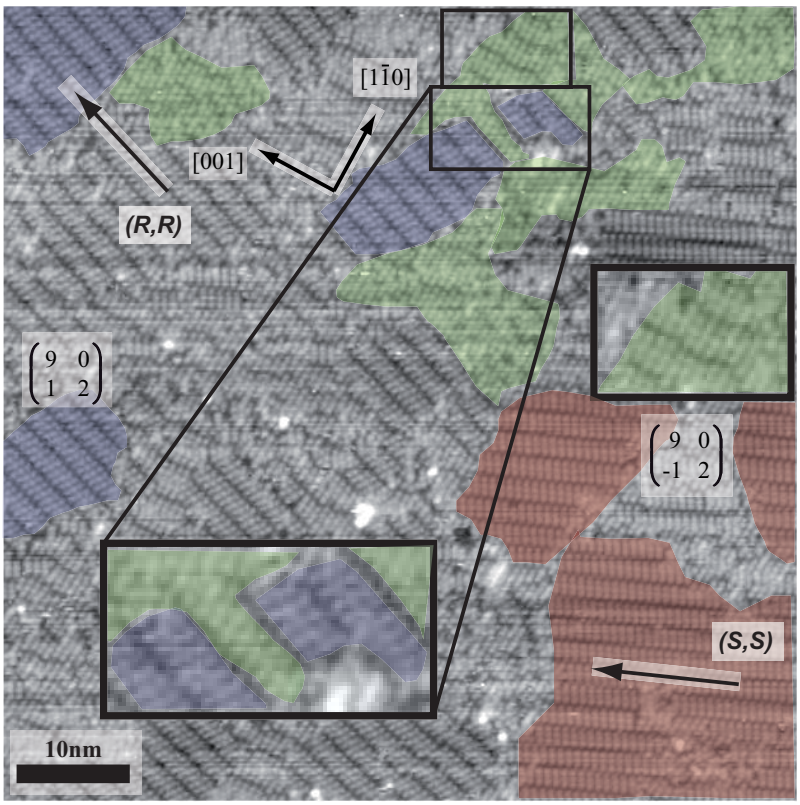

Figure 6.4: The coexistence of all phases is shown at 90% *rac.*-TA and 10% (*R*)-MA. Arrows indicate the growth direction of (*R,R*)- and (*S,S*)-TA islands respectively. Molecules in the low-ordered region are often adsorbed in triplets along [1$\bar{1}$0] direction (see insets). In the large inset a row of triplets directed along the growth direction of (*R,R*)-TA goes through a (9 0, 1 2) island. Tunneling: U= -2V, I= 50pA.

suggest that (*R*)-MA is not incorporated into any TA structure and that it rather forms a solid solution with (*S,S*)-TA instead of a well-ordered quasi-racemate with a 1:1 motif.

2. In the mixing experiment with a (*R,R*)-TA : (*S,S*)-TA : (*R*)-MA ratio of 1 : 1 : 1 the (9 0, 1 2) islands cover about 30% of the entire surface (Figure 6.5). This leads to the conclusion that only (*R,R*)-TA is adsorbed in the (9 0, 1 2) islands.

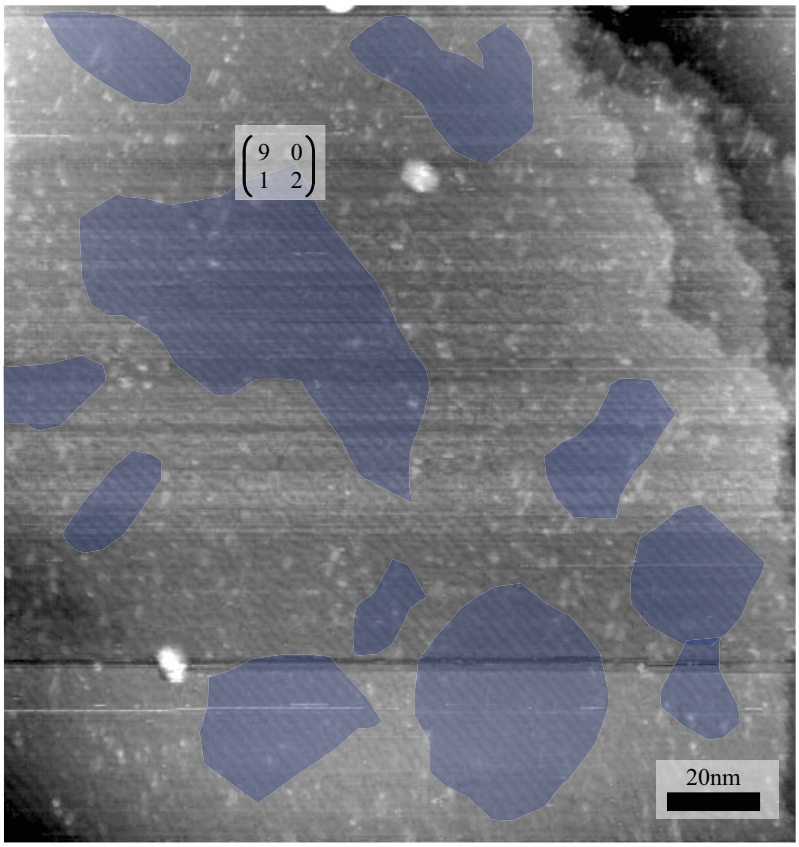

Figure 6.5: The (*R,R*)-TA (9 0, 1 2) islands (blue) cover 20-30% of the entire Cu-surface. Tunneling: U= -1.93V, I= 65pA.

3. An excess experiment with (*R,R*)- and (*S,S*)-TA resulted in the following situation [83]: Only the majority enantiomer could form large islands, while the minority enantiomer was adsorbed in only small domains. Molecules in the disordered region were often adsorbed in triplets. These observations were explained by a maximization of the mixing entropy. Since the findings in *rac.*-TA/MA are exactly the same, maximization of the mixing entropy was also considered to explain the observed effect. However, the mixing entropy calculated by determining the possibilities N in which (*R*)-MA and (*S,S*)-TA molecules can be adsorbed in triplets in the low-ordered region amounts to only ∼1.7kJ/mol (appendix E). Compared to the energy penalty of 10kJ/mol one would have to pay for the adsorption of (*S,S*)-TA in the (9 0, 1 2) structure of (*R,R*)-TA [56], this value seems to be much too small to explain the observed effect.

In order to identify the origin of the preference to form a quasi-racemic low-ordered mixture, DFT calculations have been performed by collaborators. Since these require intense computation, we focused on the above-mentioned triplet motifs. The interaction energies involved in triplets

formed from (*R*)-MA, (*R,R*)-TA and (*S,S*)-TA have been calculated by local density approximation (LDA). Again a slab of 24 × 4 Cu(110) layers was considered as in the case of the single adsorbates (section 3.1.2).

Figure 6.6a) depicts all calculated triplets. The most stable triplet is formed by two (*R*)-MA molecules with one (*S,S*)-TA molecule located in between (red ellipse). The energy penalty with respect to the most stable one is indicated, i.e. a difference of +0.2eV means that the energy gain due to formation of the respective triplet is 0.2eV lower than in the most stable case. The most stable triplet configuration is presented in detail in figure 6.6b). The distance between adjacent OH groups is only 1.67$\AA$ and the energy gain amounts to 0.5eV or 48kJ/mol. Comparison with the mixing entropy (∼1.7kJ/mol) identifies the strong lateral H-bonding interaction as driving force for formation of the quasi-racemic solution. This finding is different from the excess experiment with (*R,R*)- and (*S,S*)-TA, where the mixing entropy has been adduced to explain the observed amplification process.

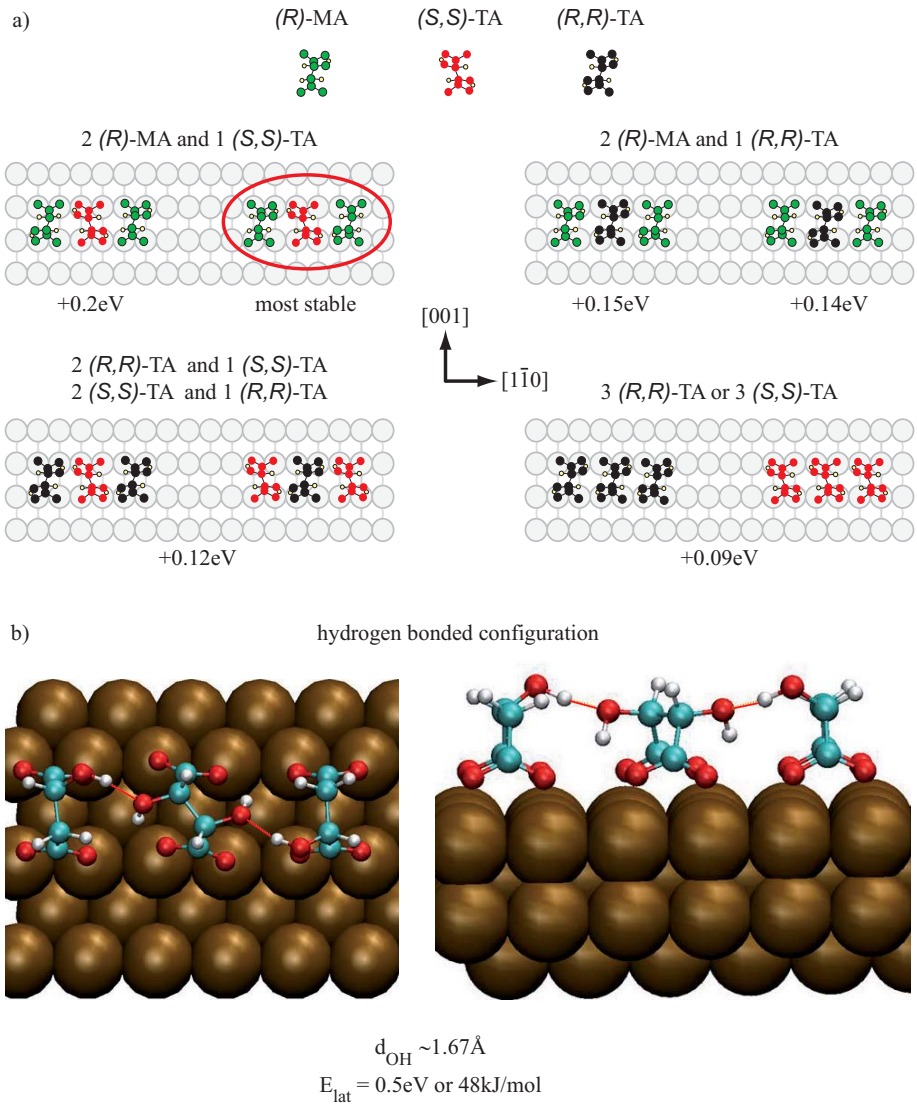

Figure 6.6: a) Calculated triplets formed by (*R*)-MA (green), (*R,R*)-TA (black) and (*S,S*)-TA (red) are shown. The energy differences in the lateral interactions compared with the most stable triplet ((*R*)-MA/(*S,S*)-TA/(*R*)-MA, red ellipse) are indicated. b) Strong hydrogen bonds are formed in the most stable triplet.

Figure 6.7 summarizes the observations that must be considered in an energy balance discussion:

- the formation of large (9 0, 1 2) islands of (*R,R*)-TA,
- the small (9 0, −1 2) (*S,S*)-TA islands
- and the formation of (*R*)-MA/(*S,S*)-TA/(*R*)-MA-triplets.

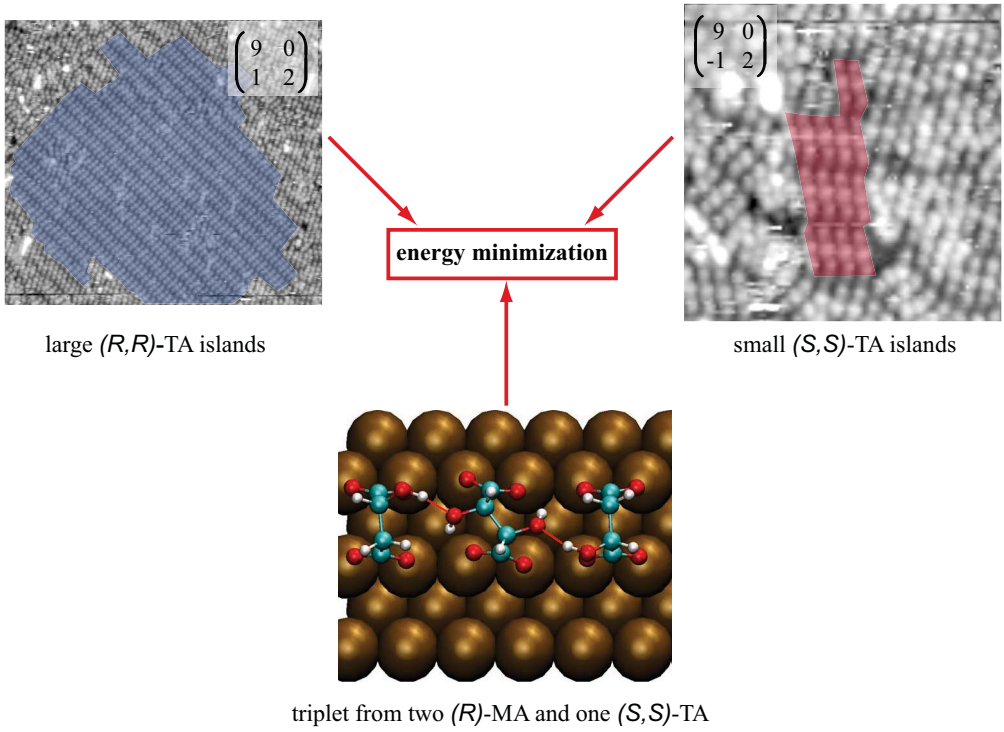

Figure 6.7: Energy balance in the system *rac.*-TA/MA. Energy minimization is suggested as driving force.

Since (*S,S*)-TA molecules bound in triplets are lost for the formation of (*S,S*)-TA islands, explaining the observed effect by energy minimization needs a comparison of the energy gain due to the formation of (9 0, −1 2) domains and (*R*)-MA/(*S,S*)-TA/(*R*)-MA-triplets. From our calculations it is clear that the homochiral triplets formed from (*R,R*)-TA or (*S,S*)-TA are by 0.09eV less favorable than the most stable (*R*)-MA/(*S,S*)-TA/(*R*)-MA-triplet (Figure 6.6). A closer look reveals that racemic TA does not only adsorb in the (9 0, 1 2) and (9 0, −1 2) domains on Cu(110), but there are also triplets aligned along $[1\bar{1}0]$, although no MA molecules are involved. These triplets might be constituted from (*R,R*)-TA or (*S,S*)-TA. Since they appear together with ordered TA islands it can be concluded that the energy involved in homochiral TA triplets is comparable to the energy of the ordered domains. Hence the energy difference between the most stable (*R*)-MA/(*S,S*)-TA/(*R*)-MA-triplets and (9 0, −1 2) islands is expected to be not too substantial.

Apart from energy minimization the reconstruction of the Cu surface could also be important. Fcc(110) surfaces are known to exhibit pronounced strain along $[1\bar{1}0]$ direction [133]. Its lowering in combination with the observed alignment along that direction might be another influence to

be considered. For alaninate on Cu(110), for example, it has been shown by theory that chiral footprints and hydrogen bonding networks lower the stress along [1$\bar{1}$0] [134].

6.4 MA excess experiments

The excess experiment using (*R,R*)-TA and (*S,S*)-TA shows a comparable result as the mixing experiment *rac.*-TA/MA. Only the majority enantiomer forms an ordered structure [83] (section 1.4). Since LEED shows the same suppression effect in both of these systems, the question arises what happens if one mixes *rac.*-MA with enantiopure MA, i.e. what happens in the MA excess experiment? Before showing the corresponding LEED results, it is useful to determine the meaning of enantiomeric excess.

6.4.1 Enantiomeric excess

The enantiomeric excess *e.e.* of a certain chiral compound is defined as ratio between the difference in coverages (ML) of the (*S*)- and (*R*)-compound and the sum of them:

$$e.e. = \frac{\theta_S(ML) - \theta_R(ML)}{\theta_S(ML) + \theta_R(ML)},$$

The e.e. in the MA excess experiments varied between 0 and -0.5. In the TA excess experiment an e.e. of 0.2 was enough to eliminate all spots corresponding to the minority enantiomer from the LEED pattern [83].

6.4.2 LEED results of *rac.*-MA/MA

Prolonged annealing (60min) of mixtures of (*R*)-MA and racemic MA (i.e. (*R*)-MA in excess) at an elevated temperature of 393K allowed to record (1 $\pm$1, $-$5 $\pm$2) LEED pattern, in which spots in one specific direction ((*S*)-direction) appeared fainter than the spots in the opposite direction ((*R*)-direction, Figure 6.8). XPS suggests a bimalate mode under these conditions. In a) the e.e. amounts to 0.24 (0.2ML (*R*)-MA and 0.63ML *rac.*-MA) and in b) to 0.50 (0.37ML (*R*)-MA and 0.38ML *rac.*-MA).

Figure 6.8 reveals that spots in (*S*)-direction are fainter the higher the enantiomeric excess of (*R*)-MA is. In order to characterize this effect mathematically the integrated spot intensities ($I_{(R)-MA}$ and $I_{(S)-MA}$) of the spots marked with red circles in a) were determined for LEED patterns with differing enantiomeric excess. From the integrated spot intensities the relative difference $\Delta I = (I_{(R)-MA} - I_{(S)-MA}/(I_{(R)-MA} + I_{(S)-MA})$ was calculated and represented as function of e.e. as shown in c). Obviously ΔI is linearly dependent on the enantiomeric excess. Hence the intensity effect observed in LEED is not amplified by the excess of (*R*)-MA. Thus this effect is not comparable to the amplification effect observed in excess experiments with (*R,R*)- and (*S,S*)-TA.

It must be assumed that the (1 $\pm$1, $-$5 $\pm$2) surface reconstruction observed with STM for *rac.*-MA (section 4.3) shows an unequal distribution of the (1 1, $-$5 2) and the (1 $-$1, $-$5 $-$2) structure as soon as one MA enantiomer is adsorbed in excess. This results in fainter LEED spots in one direction and brighter spots in the opposite one, but suppresses the cooperative majority effect, as described for TA.

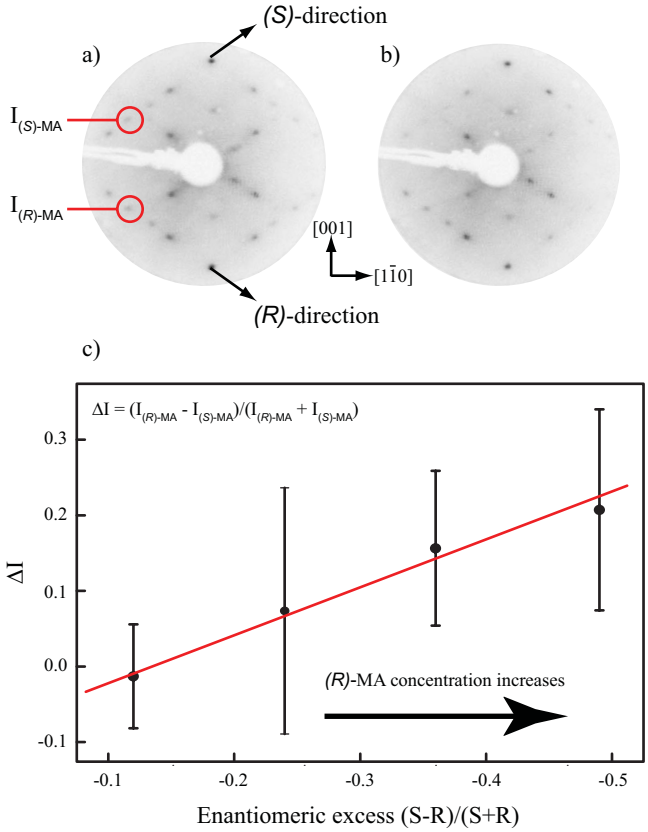

Figure 6.8: (1 $\pm$ 1, -5 $\pm$ 2) LEED pattern of two experiments with different e.e. are shown in a) and b). c) Relative difference of spot intensity ΔI as function of the e.e. Enantiomeric excess: a) 0.2ML (*R*)-MA and 0.63ML *rac.*-MA, e.e. =0.24; b) 0.37ML (*R*)-MA and 0.38ML *rac.*-MA, e.e. =0.50.

6.5 Conclusion

At a MA concentration above 25% the formation of large TA islands with opposite handedness is suppressed and, as in the case SU/TA, a single enantiomorphism is induced in LEED experiments. In the disordered region molecules are mainly aligned along $[1\bar{1}0]$, whereby often groups of triplets are identified. The most stable triplet is the combination (*R*)-MA/(*S*,*S*)-TA/(*R*)-MA along $[1\bar{1}0]$. They are formed due to strong hydrogen bonds and the energy gain with respect to three isolated molecules amounts to 48kJ/mol.

Chapter 7

Chiral conflict between racemic malic acid and tartaric acid enantiomers

Intermolecular chiral recognition between MA and TA is not only observable in the mixing experiment *rac.*-TA/MA, but also in the system *rac.*-MA/TA. In this chapter the results of mixing *rac.*-MA with TA are presented and compared to the experiment *rac.*-TA/MA.

7.1 XPS of *rac.*-MA/(*R,R*)-TA mixtures

Figure 7.1 compares the XP spectra of pure *rac.*-MA (a, θ=0.196), a *rac.*-MA/(*R,R*)-TA mixture (b, 32% (*R,R*)-TA, θ=0.19) and (*R,R*)-TA (c, θ=0.208). The spectrum in a) corresponds to a $(1\ \mp 1,\ 9\ \pm 5)$ overlayer created by heating 60min at 348K. For the spectrum in b) a $(3\ -2,\ 3\ 4)$ spectrum has been observed after 60min at 393K, while the XP spectrum in c) relates simultaneously to a $(9\ 0,\ 1\ 2)$ and $(2\ 1,\ -7\ 7)$ superstructure observed after 30min at 405K. For all the fits a bimalate/bitartrate adsorbate mode has been assumed. Thus the spectrum in a) has been fitted with basically three peaks in the ratio 2 (COO^-): 1 ($CH(OH)$) : 1 (CH_2). For the signal in b) again three peaks have been used, but this time in the ratio 3 (COO^-) : 2 ($CH(OH)$) : 1 (CH_2) (according to the ratio of MA and TA). Two peaks in the ratio 1 (COO^-) : 1 ($CH(OH)$) allowed to fit the peak in c). Figure 7.1 shows that good fits are possible under these assumptions. The small components at the low- and high-energy sides under the spectra are probably due to the limits of the background subtraction procedure.

In table 7.1 all fits are listed and compared. Peak energies and FWHM's (in parentheses) are indicated in eV.

C1s fits of racemic MA; 68% : 32% mixture of *rac.*-MA and (*R,R*)-TA; pure (*R,R*)-TA					
Coverage	system	$CH(OH)$	COO^-	$COOH$	$-CH_2$
0.196	*rac.*-MA	285.6 (1.8)	287.7 (2.2)	-	284.7 (1.4)
0.19	*rac.*-MA + (*R,R*)-TA	285.4 (2.2)	287.3 (2.3)	-	284.2 (1.5)
0.208	(*R*)-TA	285.7 (2.3)	287.4 (2.4)	-	-

Table 7.1: Comparison of the C1s fits of racemic MA at a coverage of θ=0.196 after 60min at 348K, a 68% : 32 % mixture of *rac.*-MA and (*R,R*)-TA (θ=0.19=0.13+0.06, 60min tempered at 393K) and enantiopure (*R,R*)-TA (θ=0.208, 30min at 405K). Full-width-at-half-maxima are indicated in parentheses.

The comparison of the fits shows neither significant differences in peak energy nor in FWHM. Only the CH_2 peaks of the racemic MA spectrum and the *rac.*-MA/TA mixture differ by a

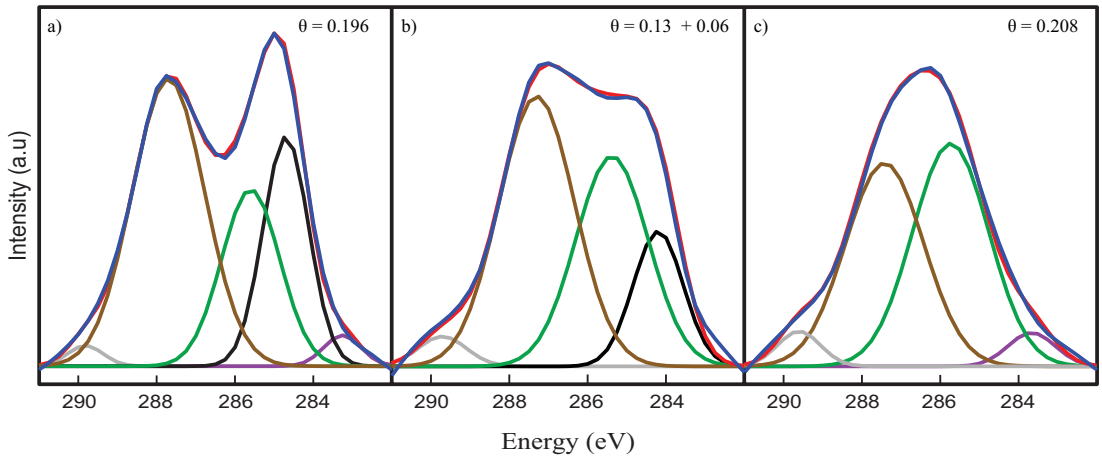

Figure 7.1: XP spectra of pure *rac.*-MA (a), a *rac.*-MA/(*R,R*)-TA mixture (b), 32% (*R,R*)-TA) and enantiopure (*R,R*)-TA in c). Coverages: a) θ=0.196, b) θ=0.13+0.06, c) θ=0.208. A bimalate/bitartrate adsorbate mode is expected in all spectra.

larger value of 0.5eV. According to XPS, a bimalate/bitartrate adsorbate mode seems to be quite reasonable for the *rac.*-MA/TA mixtures after an extended heating at elevated temperature.

7.2 LEED patterns observed in *rac.*-MA / TA experiments

An extended 60min heating of a 66% *rac.*-MA : 34% (*R,R*)-TA mixture (θ=0.20) at 393K allowed to observe a well ordered chiral (3 -2, 3 4) overlayer in LEED (Figure 7.2a)). Replacing (*R,R*)-TA by 31% (*S,S*)-TA induced the mirrored (3 $-$ 2, 3 4)^M structure as shown in b). The chiral bias, this time provided by TA enantiomers, suppresses formation of one enantiomorph in the racemic MA lattice and induces a single enantiomorphism. Prolonged annealing seems to be a crucial step as can be seen by comparison of the mirror structures shown in a) and b). The structure in b) was produced by a short 5min annealing at 393K. The quality of the LEED structure in a) is much better than the quality of the structure in b). The high temperature and long annealing time to create a good pattern suggest that a substantial mass transport is involed. The concentration of TA dopant is annother important factor. Already 3% of (*R,R*)-TA was sufficient to observe the (3 $-$ 2, 3 4) superstructure. The (3 $-$ 2, 3 4) is still induced when the (*R,R*)-TA portion is 72%. At even higher concentration of 98% (*R,R*)-TA (θ=0.19, 60min at 393K) no (3 -2, 3 4) structure is observed anymore. Instead LEED shows simultaneously a (9 0, 1 2) and (2 1, -7 7) (c). Both overlayers are ascribed to TA, since they are also observable for pure (*R,R*)-TA after 30min at 408K.

7.2.1 LEED: comparison of mixing experiments

As in the case of *rac.*-TA/MA LEED allows to observe the induction of a chiral structure also in the system *rac.*-MA/TA. In both cases the handedness of the produced overlayer depends on the handedness of the dopant. However, the required amount of dopant is quite different in both systems. A small TA concentration of 3% suffices to induce a chiral structure in *rac.*-MA. This is a strong indication of an amplified process. On the other hand at least 25% of MA is needed to induce a chiral structure in *rac.*-TA. Thus the mechanisms that allow to install homochirality in LEED patterns of *rac.*-TA and *rac.*-MA might be of different nature. This is also reflected by

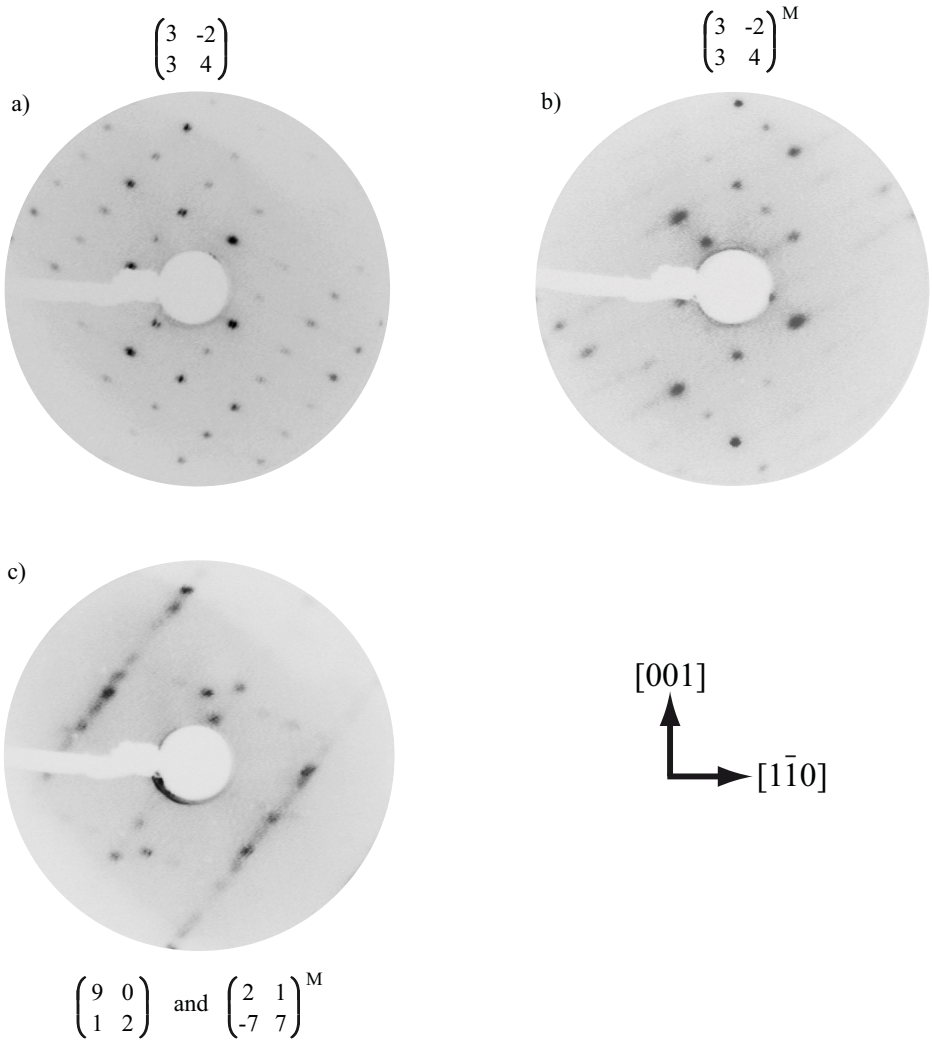

Figure 7.2: LEED patterns of *rac.*-MA/TA mixtures. a) 66% *rac.*-MA : 34% (*R,R*)-TA at θ=0.20, 60min tempered at 393K; b) 69% *rac.*-MA : 31% (*S,S*)-TA at θ=0.22, 5min heated at 393K; c) 2% *rac.*-MA : 98% (*R,R*)-TA at θ=0.19, 60min at 393K. Electron energies: a) 25eV, b) 25eV, c) 23eV.

the different temperatures needed in both experiments. With TA as dopant in *rac.*-MA a much higher temperature induces the single-enantiomorphsm effect.

7.3 RAIRS of *rac.*-MA/(*R,R*)-TA mixtures

The RAIR spectrum of a *rac.*-MA/(*R,R*)-TA mixture (35% (*R,R*)-TA, θ=0.21=0.14+0.07) after 10min heating at 403K is shown in figure 7.3a). For this mixture a chiral (3 $-$2, 3 4) overlayer was observed in LEED. The bands corresponding to the simultaneous existence of a (9 0, 2 1) and (2 1, $-$7 7) of (*R,R*)-TA (θ=0.206) induced by 10min heating at 405K are depicted in b).

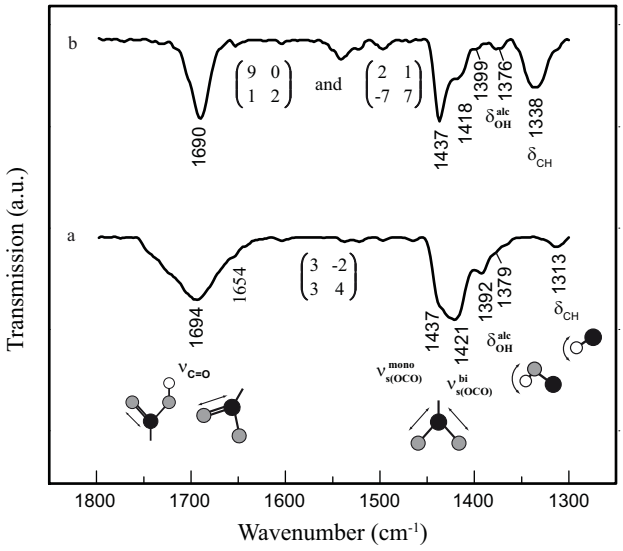

Figure 7.3: Comparison of RAIR spectra: a) 65% *rac.*-MA and 35% (*R,R*)-TA after 10min at 403K (θ=0.21, (3 $-$2, 3 4)); b) (*R,R*)-TA after 10min at 405K (θ=0.206, simultaneously (9 0, 2 1) and (2 1, $-$7 7)).

The spectrum in a) shows a band at 1421cm^{-1} that can be interpreted as ν_S^{OCO} of bimalate or bitartrate [45]. The shoulder at 1437cm^{-1} corresponds to the same oscillation for a single deprotonated mono-species. Accordingly, the band at 1694cm^{-1} might represent $\nu^{C=O}$. However, this band is quite broad and therefore other oscillations are expected to contribute as well. In figure 4.8d) in section 4.6 an unidente carboxylate species due to a reconstructed Cu surface was offered to explain the band at 1654cm^{-1}, which appears as shoulder also in spectrum a). The band at 1392cm^{-1} is due to δ^{OH} of MA, while the oscillation at 1379cm^{-1} corresponds probably to a TA δ^{OH}. In b) a pure TA spectrum is shown. Here two bands appear at 1399cm^{-1} and 1376cm^{-1}. According to ref. [45] these oscillations can be identified as δ^{OH} of monotartrate and bitartrate. Thus in the mixture *rac.*-MA /(*R,R*)-TA in a) also monotartrate could have a contribution to the band at 1392cm^{-1}. Summarized, in the *rac.*-MA/(*R,R*)-TA mixture resulting in a (3 $-$2, 3 4) overlayer after 10min at 403K, bimalate and bitartrate as well as monomalate and monotartrate are expected to co-exist. A surface reconstruction might in addition result in unidente carboxylate species.

Apart from the well known (9 0, 1 2), 10min heating of (*R,R*)-TA at 405K allowed to observe a (2 1, $-$7 7) overlayer. This structure has not been reported for TA before. The RAIR spectrum in b) shows a strong monotartrate ν_S^{OCO} band at 1437cm^{-1} and a corresponding $\nu^{C=O}$ at 1690cm^{-1}. But also bitartrate adsorbates exist, since a corresponding ν_S^{OCO} oscillation is visible

at $1418cm^{-1}$. As already mentioned above, the bands at $1399cm^{-1}$ and $1376cm^{-1}$ represent a deformation vibration of the hydroxyl group [45], whereas the band at higher frequency is due to monotartrate. The strong band at $1338cm^{-1}$ can be attributed to a δ^{CH} of bitartrate. Interestingly, this oscillation is very strong for TA, while the corresponding signal at $1313cm^{-1}$ in the mixture of *rac.*-MA and (*R,R*)-TA in a) is rather weak. Hence it might be concluded that the RAIR spectrum in a) is dominated by MA although the TA portion is 35%. RAIRS does not allow to determine if the molecules are adsorbed as montartrate in the (2 1, −7 7) superstructure, since the observed mono-features could also be due to monotartrate adsorbed in the disorder.

According to XPS in section 7.1 the spectra can be fitted nicely assuming a bimalate and bitartrate adsorbate mode. Here, RAIRS shows again that this simple picture might not be valid. There is always a contribution from single deprotonated adsorbates and surface reconstruction might also result in unidente carboxylate species.

7.4 STM of *rac.*-MA mixed with TA

Figure 7.4a) shows the (3 −2, 3 4) and $(3\ -2,\ 3\ 4)^M$ STM structures observed for *rac.*-MA after 120min tempering at 393K (chapter 4). In b) the (3 −2, 3 4) for a 66% *rac.*-MA : 34% (*R,R*)-TA mixture is represented (120min at 393K). This confirms the LEED result that mixing *rac.*-MA with (*R,R*)-TA induces a single enantiomorphism on the entire surface. A change at the tip is visible in c). The arrangement of molecules shown in the upper part resembles that one in the (3 −2, 3 4) overlayer in a). In d) a 30nm × 30nm scan of the induced superstructure is shown. Three dots are aligned along the $[1\bar{1}0]$ direction.

A tentative model for the arrangement of molecules in the (*R,R*)-TA induced (3 −2, 3 4) overlayer is represented in figure 4.2 in chapter 4. In the unit cell two (*S*)-MA (red) and one (*R*)-MA (green) are adsorbed along $[1\bar{1}0]$. In order to induce this structure, a substantial mass transport is needed, since the opposite handed $(3\ -2,\ 3\ 4)^M$ structure is formed from (*R*)-MA and (*S*)-MA in the ratio 2:1. Hence, under influence of (*R,R*)-TA as dopant, the $(3\ -2,\ 3\ 4)^M$ building blocks are split up to form (3 −2, 3 4) building blocks. In this process 25% of all molecules remain unbound in the disorder. This assumption is supported by the 100nm × 100nm scan depicted in figure 7.5. ∼50% of the entire surface is ordered. However, there are three times as much molecules in the ordered region than in the disorder. Consequently 75% of the molecules are bound in the ordered (3 −2, 3 4) structure and 25% are in the disorder.

The (3 −2, 3 4) and $(3\ -2,\ 3\ 4)^M$ structures found for *rac.*-MA appear only in small islands as shown in figure 7.4a). Hence, there are lots of domain boundaries. This situation might be energetically unfavourable. In addition, TA as dopant favours a specific overlayer. The TA molecules are not expected to be incorporated into the MA structure since the (3 −2, 3 4) and $(3\ -2,\ 3\ 4)^M$ are already observed for pure *rac.*-MA. Hence, the chiral TA bias and the energetically unfavorable situation of domain boundaries could result in the amplification effect: Only 3% of TA is enough to induce a single enantiomorphism in *rac.*-MA. A similar mechanism has been suggested in the sergeants and soldiers effect observed in SU/TA [78] as well as in the system heptahelicene/Cu(111) [79, 135].

A mechanism as proposed in the mixing experiment *rac.*-TA/MA seems to be unlikely in *rac.*MA/TA. Figure 7.5 shows that the disordered region is much more chaotic than in the case of *rac.*-TA/MA. Obviously there is no distinct adsorption direction of molecules and a triplet formation is also not observable. The low TA concentration needed to induce the suppression effect is another argument against the formation of energy-minimizing motifs in the disorder.

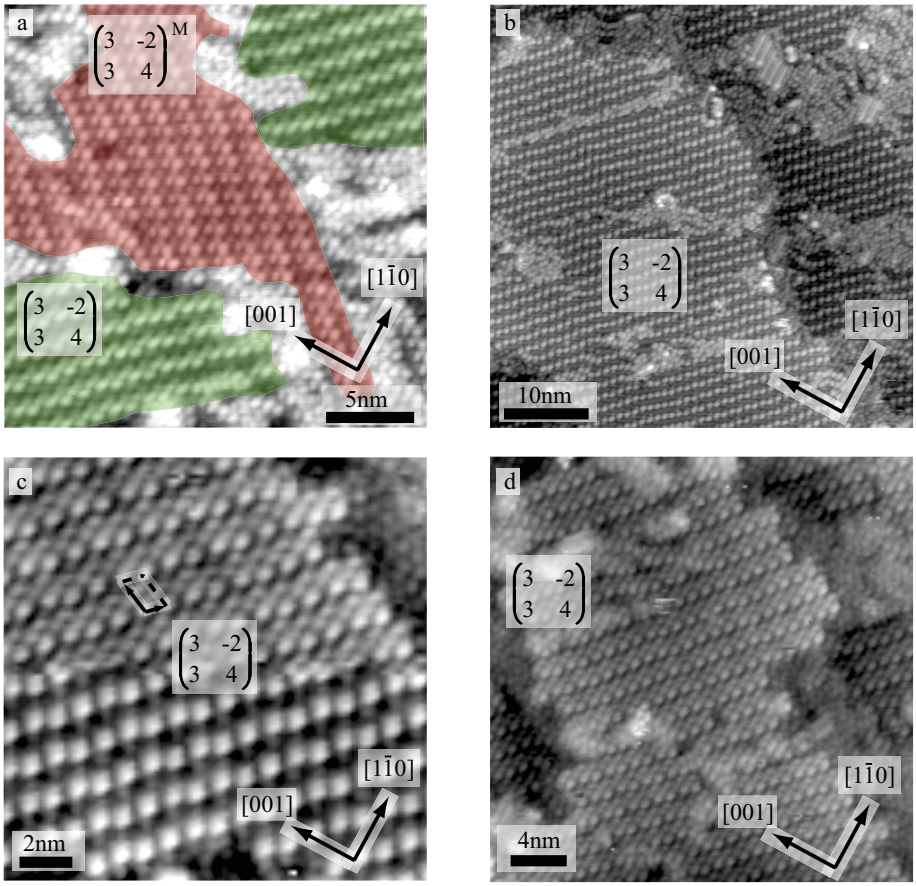

Figure 7.4: STM structures observed for pure *rac.*-MA and *rac.*-MA doped with (*R,R*)-TA. a) $(3\ -2,\ 3\ 4)$ and $(3\ -2,\ 3\ 4)^M$ structure induced in *rac.*-MA after 120min heating at 393K, θ^{local}=0.11 (U= -1.93V, I= 50pA). b) $(3\ -2,\ 3\ 4)$, 66% *rac.*-MA and 34% (*R,R*)-TA, 120min heated at 393K (U= -2.0V, I= 50pA). c) Example for a change in contrast due to a change at the tip, θ^{local}=0.16 (U= -1.54V, I= 50pA). d) 30nm × 30nm scan of the induced $(3\ -2,\ 3\ 4)$ superstructure, three dots are aligned along the [1$\bar{1}$0] direction (U= -1.54V, I= 50pA).

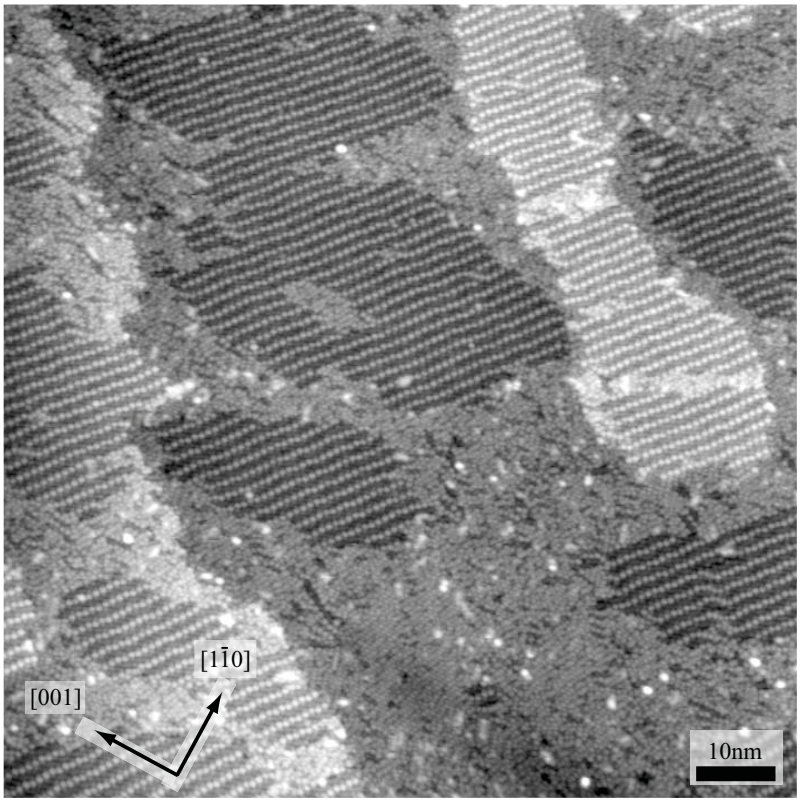

Figure 7.5: 100nm × 100nm scan of the $(3\ -2,\ 3\ 4)$ overlayer induced by doping 66% *rac.*-MA with 34% (*R,R*)-TA after 120min at 393K. 52% of the surface is covered by ordered islands. Three times as much molecules are in the ordered structure than in the disorder. Consequently, 75% of the molecules are bound in the $(3\ -2,\ 3\ 4)$ and 25% are in the disorder. U= -2.0V, I= 50pA.

7.4.1 STM: comparison of mixing experiments

STM revealed that in the system *rac.*-MA/TA only one ordered structure remains after doping. This is not true for *rac.*-TA doped with MA. In this system opposite handed TA islands are always present. Minimization of the energy is the driving force. This results in the formation of triplets in a low-ordered pseudoracemic region. The domains visible in LEED are exclusively formed from (*R,R*)-TA or (*S,S*)-TA. No real amplification process can be observed since at least 25% of MA dopant is necessary.

Amplification is on the other hand the protruding attribute in *rac.*-MA/TA. In this system TA acts as a chiral bias. The simultaneous existence of opposite handed domains in *rac.*-MA might be energetically unfavorable. In addition, TA favours either the heterochiral $(3\ -2,\ 3\ 4)$ or $(3\ -2,\ 3\ 4)^M$ structure. Consequently the system minimizes its energy by means of single enantiomorphism.

7.5 Conclusion

A single enantiomorphism can be induced by doping racemic MA with TA. According to XPS the molecules in the MA/TA mixtures are adsorbed as bimalate and bitartrate. However, RAIRS suggests that reconstruction induced unidente species as well as monomalate and monotartrate might also be present on the surface. A prolonged annealing time at high temperature is needed to install the single enantiomorphism. The amplification effect observed can be explained by a small chiral TA bias and an energetically unfavorable coexistance of the $(3\ -2,\ 3\ 4)$ and $(3\ -2,\ 3\ 4)^M$ structures in *rac.*-MA. However, in order to elucidate the proper mechanism DFT calculations are proposed.

Outlook

Chirality transfer from single molecules into two-dimensional chiral arrays has been studied for malic acid (MA) on Cu(110). For enantiopure MA a variety of structures could be observed on Cu(110) either with LEED or STM, indicating that the missing C_2 symmetry (only one OH group) in MA results in an increased variation of possible structures. In areas between ordered structures, STM revealed a reconstruction of the underlying Cu surface, suggesting a pronounced chirality transfer via the substrate, rather than by intermolecular hydrogen bonding. For *rac.*-MA an ordered reconstruction of the Cu surface was oberved in LEED. Chiral conflict leads to single enantiomorphism, either when TA is mixed into *rac.*-MA or vice versa.

Replacing the hydroxyl group in MA by an apolar functional group as for instance CH_3 (,i.e. 2,3-dimethyl succinic acid) would permit to explore the influence of the kind of functional group on the self-assembly in ordered 2D structures as well as the effect on reconstruction and etching of the surface. Doping experiments would in addition make it possible to investigate chiral recognition between molecules with different functional groups and different degrees of symmetry. Comparison with *rac.*-TA/MA could help to determine the influence of the symmetry and functional groups in the recognition process. Theoretical calculations are an important tool that could help to better understand for example the observed adsorbat-induced reconstructions and the observed unidente species.

Appendix

A TPD of racemic MA

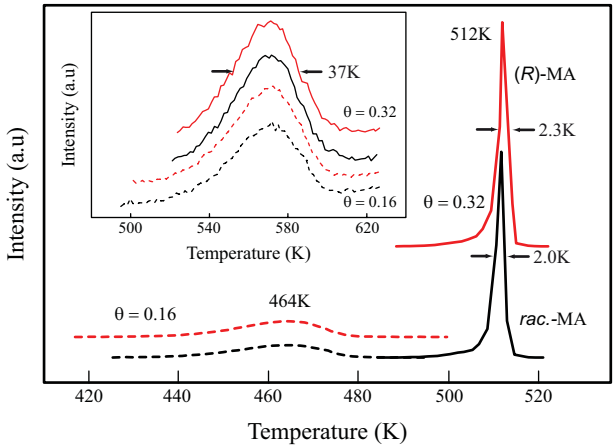

Figure A: 44 amu TPD spectra of *rac.*-MA and enantiopure (*S*)-MA at low coverage (θ=0.16 at RT, dashed lines) and saturated coverage (θ=0.32 at RT). The heating rate was β=4.1K/s. At saturation both *rac.*-MA and (*R*)-MA show a surface explosion with a FWHM of 2K or 2.3K respectively. The peaks at lower coverage display the same shape and have the same peak temperature of 464K. All high-temperature peaks (inset) are rather broad (FWHM ∼37K) and appear at ∼571K.

TPD of *rac.*-MA: Peak intensities (I_1 and I_2) and temperatures (T_1 and T_2) of 44 amu					
Deposition time	I_1 (a.u.)	T_1 (K)	I_2 (a.u.)	$T_2(K)$	R
1min	1.0	454	1.6	578	1.6
5min	4.9	457	4.3	574	0.9
10min	8.9	464	6.1	572	0.7
15min	18.3	492	8.9	569	0.5
20min	19.4	513	6.1	574	0.3
35min	17.8	512	8.3	569	0.5
45min	18.9	512	8.9	572	0.5

Table A: Integrated peak intensities (a.u., 44 amu) and peak temperatures in K of the first and second peak in *rac.*-MA TPD spectra are indicated for various deposition times. The intensity ratios $R = I_2/I_1$ of first and second peak are also calculated.

B UPS spectra of *rac.*-MA

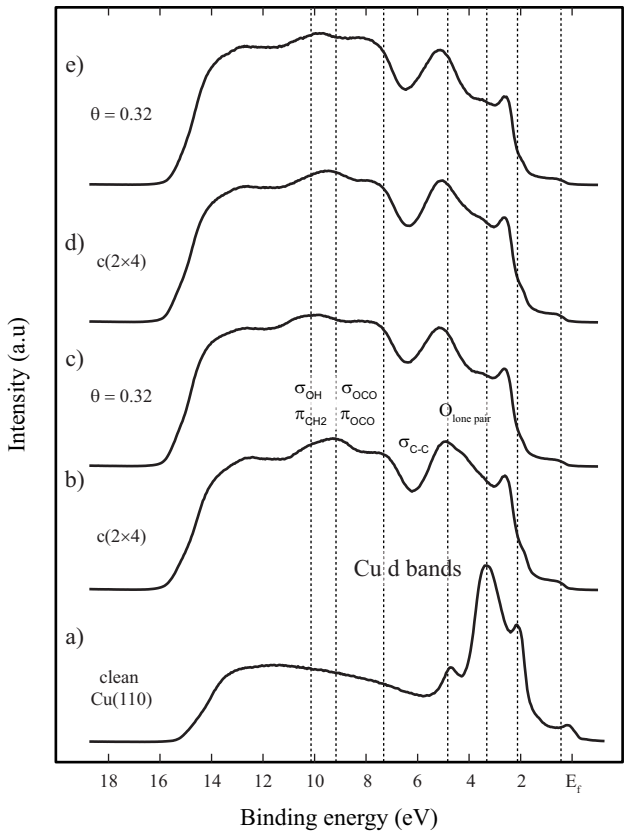

Figure B: UP spectra of clean Cu(110), c(2×4) overlayers and one saturated monolayer of racemic and enantiopure MA are compared. a) Contribution of the Cu 3d bands. b) Spectrum corresponding to the c(2×4) of *rac.*-MA. c) Saturated racemic monolayer. d) c(2×4) spectrum of enantiopure MA. e) Saturated monolayer of (*R*)-MA. The assignment of orbitals is based on handbooks [120, 121] and measured spectra of similar compounds (formic and acetic acid) on Cu(110) [116, 122].

C XPS of *rac.*-MA and (*R*)-MA

Comparison of *rac.*-MA and (*R*)-MA XP spectra						
Coverage	system	adsorption mode	$CH(OH)$	COO^-	$COOH$	$-CH_2$
0.16	(*R*)-MA	bi	285.8 (2.1)	287.6 (2.2)	-	284.8 (1.7)
0.15	*rac.*-MA	bi	285.3 (2.2)	287.5 (2.2)	-	284.5 (1.6)
0.25	(*R*)-MA	mono	286.2 (2.1)	287.5 (1.8)	288.4 (2.25)	284.9 (1.6)
0.25	*rac.*-MA	mono	285.7 (1.9)	287.0 (1.7)	288.0 (2.1)	284.4 (1.7)

Table C: Comparison of peak fits for (*R*)-MA and *rac.*-MA XP spectra at θ ~0.16 and 0.25. At lower coverage MA is assumed to be adsorb as bimalate due to moderate annealing, while a monomalate adsorption mode is expected in the c(2×4) at $\theta = 0.25$. Adsorption mode: bi stands for bimalate and mono for monomalate. FWHM's are indicated in parentheses.

D XPS of enrichment experiments with *rac.*- and enantiopure MA

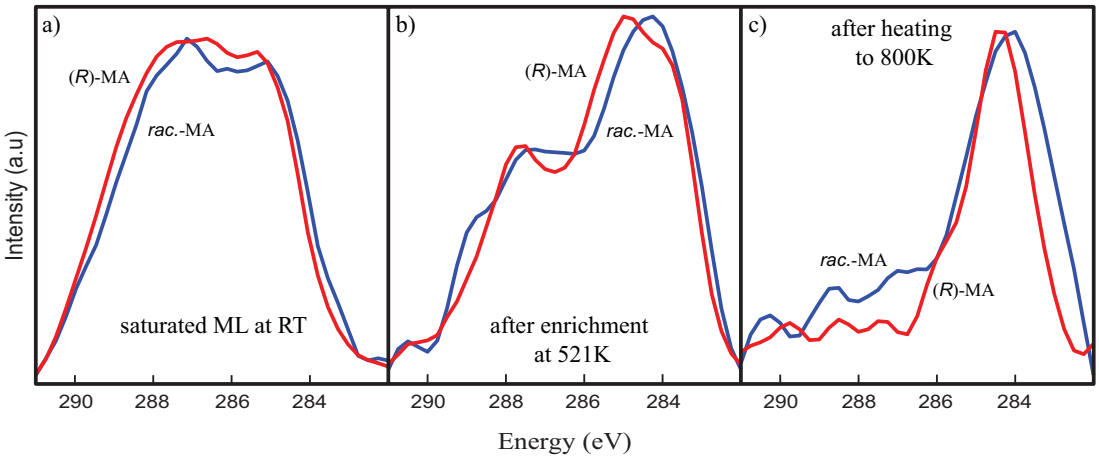

Figure D: C1s XP spectra of enrichment experiments with (*R*)-MA (red) and *rac.*-MA (blue). a) represents the spectra of a saturated monolayer at RT. b) C1s signals from the residuals after annealing to 521K (three enrichment cycles, heating rate β=4.1K/s). c) Residuals on the Cu(110) crystal after full desorption of the second 44 amu peak, i.e. after desorption of the enriched fragments in b) by heating to 800K.

E Mixing entropy

The entropy S of a system with a certain number of possible states N is given by [136]

$$S = k_B ln(N).$$

All the states N have the same energy, k_B is the Boltzmann constant. In the mixing experiment *rac.*-TA/(*R*)-MA the (*R,R*)-TA molecules are assumed to be adsorbed in ordered (9 0, 1 2) islands. Hence, only (*S,S*)-TA and (*R*)-MA molecules are found in the triplets in the low-ordered region. The unit cell of the (9 0, 1 2) structure has an area of $\sim 169 \mathring{A}^2$. A triplet in the low-ordered region takes up the same room. Hence in the 66% *rac.*-TA / 33% (*R*)-MA mixing experiment, the (9 0, 1 2) (*R,R*)-TA islands should occupy 33% of the entire Cu surface. Thus, it will be assumed that $\sim 66\%$ of the surface is covered by a low-ordered structure of triplets, which amounts on the respective Cu(110) single crystal ($\sim$7mm diameter) to an area of $\sim 1.02 \cdot 10^{16} \mathring{A}^2$. This corresponds to $6.0 \cdot 10^{13}$ triplets or $Z = 1.8 \cdot 10^{14}$ molecules or places. Adsorbing only one kind of molecules in triplets results in only one discriminable state, i.e. $N = 1$ and $S = 0$ if only (*R*)-MA or (*S,S*)-MA molecules are adsorbed in triplets. Therefore, the mixing entropy ΔS is simply given by $\Delta S = k_B ln(N)$ with N the number of discriminable possibilities to adsorb (*R*)-MA and (*S,S*)-TA molecules on $Z = 1.8 \cdot 10^{14}$ places.

With Z the number of places and K_1 the number of (*R*)-MA molecules, K_2 the number of (*S,S*)-TA molecules and $Z = K_1 + K_2$ the number of discriminable realizations N is given by

$$N = Z!/K_1! \cdot K_2!.$$

Hence the mixing entropy is

$$\Delta S = k_B ln(N) = ln(Z!) - ln(K_1!) - ln(K_2!).$$

Since Z, K_1 and K_2 are large numbers the Stirling formula $n! = \sqrt{2\pi n} n^n e^{-n}$ has to be used in order to calculate ΔS. It follows:

$$\Delta S = ln(\sqrt{2\pi Z}) + Z ln(Z) - Z - ln(\sqrt{2\pi K_1}) - K_1 ln(K_1) + K_1 - ln(\sqrt{2\pi K_2}) - K_2 ln(K_2) + K_2.$$

In the considered experiment $K_1 = K_2 = Z/2 = 9.0 \cdot 10^{13}$ holds. The calculated mixing entropy amounts thus to 1.69kJ/mol. In this example all the molecules were placed separately in the triplets. What happens, if we assume homochiral triplets of (*R*)-MA and (*S,S*)-TA to be adsorbed? In this case Z^{tri} represents the number of triplets, i.e. $Z^{tri} = 6.0 \cdot 10^{13}$. The number of (*R*)-MA and (*S,S*)-TA triplets is now $K_1^{tri} = K_2^{tri} = Z^{tri}/2 = 3.0 \cdot 10^{13}$. However, not surprisingly the calculated mixing entropy ΔS^{tri} equals the above calculated mixing entropy of single molecules: $\Delta S = \Delta S^{tri} = 1.69 kJ/mol$.

List of publications and conference contributions

Publications

As of October 2010 the following publications evolve from this work. The corresponding chapters are indicated in brackets.

- Two-dimensional self-assembly of chiral malic acid on Cu(110).
  C. Roth, D. Passerone, L. Merz, M. Parschau and K.-H. Ernst
  Journal of Physical Chemistry C (in press: doi: 10.1021/jp106575g)
  (chapter 3)

- Pasteur's quasiracemates in 2D: chiral conflict between structurally different enantiomers induces single-handed enantiomorphism.
  C. Roth, D. Passerone and K.-H. Ernst
  Chem. Comm. (in press: doi: 10.1039/C0CC03060K)
  (chapter 6)

- Surface explosion chemistry of chiral malic acid on Cu(110).
  C. Roth and K.-H. Ernst
  Top. Catal.
  (chapter 5, in preparation)

- Chiral conflict in mixed layers of racemic malic acid and enantiopure tartaric acid.
  C. Roth, D. Passerone, L. Merz, M. Parschau and K.-H. Ernst
  ChemPhysChem
  (chapter 4 and 7, in preparation)

- DFT study of malic acid on Cu(110).
  D. Passerone, C. Roth and K.-H. Ernst
  (chapter 6, in preparation)

Conference contributions

- Adsorption and two-dimensional self-assembly of malic acid on Cu(110).
  C. Roth, L. Merz, M. Parschau and K.-H. Ernst
  *ECOSS 25, Liverpool, July **2008** (Oral presentation)*

- Single enantiomorphism and chiral conflict in 2D crystals.
  C. Roth, L. Merz, M. Parschau and K.-H. Ernst
  *DPG, Regensburg, March **2010** (Oral presentation)*

- Vibrational spectroscopy of the system malic acid/Cu(110).
  C. Roth, D. Ferri and K.-H. Ernst
  *CCMX annual meeting, Bern, April **2010** (Oral presentation)*

- Single enantiomorphism and chiral conflict in 2D crystals.
  C. Roth, L. Merz, M. Parschau and K.-H. Ernst
  *MolCHsurf, Bern, June **2010** (Invited Oral presentation)*

- Single enantiomorphism due to chiral conflict in 2D crystals.
  C. Roth, L. Merz, M. Parschau and K.-H. Ernst
  *ECOSS 27, Groningen, September **2010** (Oral presentation)*

- Chiral and achiral butanedioic acids on Cu(110): 2D enantiomorphism and surface explosion.
  C. Roth, M. Parschau, B. Behzadi, S. Romer, K.-H. Ernst
  *SAOG 07, Fribourg, February **2007** (Poster presentation)*

- Adsorption and two-dimensional self-assembly of malic acid on Cu(110).
  C. Roth, L. Merz, M. Parschau and K.-H. Ernst
  *SAOG 09, Fribourg, February **2009** (Poster presentation)*

Curriculum Vitae

Name	Christian Alexander Roth
Date of birth	25th of April 1976
City	Schlieren ZH
Nationality	Swiss

Education

1993-1996	Apprenticeship as laboratory assistant in Chemistry
1997-2001	General qualification for university entrance for adults
2001-2006	Studies of physics at ETH Zürich
2006-2010	Dissertation under the supervision of Prof. Dr. Karl-Heinz Ernst

References

[1] Lord Kelvin. Baltimore Lectures on Molecular Dynamics and Wave Theory of Light. The MIT Press, 1904.

[2] L. Pasteur. Sur les relations qui peuvent exister entre la forme cristalline, la composition chimique et le sens de la polarisation rotatoire. Ann. Chim. Phys., 24:442–459, 1848.

[3] J. H. van 't Hoff. Bull. Soc. Chim., 1875.

[4] J. A. Le Bel. Bull. Soc. Chim. 2, 1874.

[5] R. S. Cahn, C. Ingold, and V. Prelog. Specification of Molecular Chirality. Angew. Chem. Int. Ed., 5:385–415, 1966.

[6] C. J. Baddeley. Giving surfaces a hand. Nature Chemistry, 1:345–346, 2009.

[7] S. F. Mason. Origin of biomolecular handedness. NATURE, 311:19–23, 1984.

[8] A. Salam. The Role of Chirality in the Origin of Life. J. Mol. Evol., 33:105–113, 1991.

[9] C. A. Orme, A. Noy, A. Wierzbicki, M. T. McBride, M. Grantham, H. H. Teng, P. M. Dove, and J. J. DeYoreo. Formation of chiral morphologies through selective binding of amino acids to calcite surface steps. NATURE, 411:775–779, 2001.

[10] L. Addadi and S. Weiner. Crystals, asymmetry and life. NATURE, 411:753–755, 2001.

[11] M. Goldhaber, L. Grodzins, and A. W. Sunyar. Helicity of Neutrinos. Phys. Rev., 109:1015–1017, 1958.

[12] http://nobelprize.org/nobel_prizes/chemistry/laureates/2001/.

[13] http://nobelprize.org/nobel_prizes/chemistry/laureates/2007/.

[14] J. M. Thomas, T. Maschmeyer, B. F. G. Johnson, and D. S. Shephard. Constrained chiral catalysts. J. Mol. Catal. A, 141:139–144, 1999.

[15] H.-U. Blaser. Enantioselective Synthesis Using Chiral Heterogeneous Catalysts. Tetrahedron: Asymm., 9:843–866, 1991.

[16] G. Webb and P. B. Wells. Asymmetric Hydrogenation. Catal. Today, 12:319–337, 1992.

[17] H.-U. Blaser, H.-P. Jalett, M. Müller, and M. Studer. Enatioselective hydrogenation of α-ketoester using cinchona modified platinum catalysts and related systems: A review. Catal. Today, 37:441–463, 1997.

[18] C. Baddeley. Fundamental investigations of enantioselective heterogeneous catalysis. Topics Catal., 25:17–27, 2003.

[19] Y. Orito, S. Imai, and S. Niwa. Asymmetric Hydrogenation of Methyl Pyruvate Using Pt-C Catalyst Modified with Cinchonidine. Nippon Kagaku Kaishi, 8:1118–1120, 1979.

[20] P. B. Wells and A. G. Wilkinson. Platinum group metals as heterogeneous enantioselective catalysts. Topics Catal., 5:39–50, 1998.

[21] I. M. Sutherland, A. Ibbotson, R. B. Moyes, and P. B. Wells. Enantioselective Hydrogenation. J. Catal., 125:77–88, 1990.

[22] A. Hoek and W. M. Sachtler. Enantioselectivity of Nickel Catalysts Modified with Tartaric Acid or Nickel Tartrate Complexes. J. Catal., 58:276–286, 1979.

[23] M. Studer, H.-U. Blaser, and C. Exner. Enantioselective Hydrogenation Using Heterogeneous Modified Catalysts: An Update. Adv. Synth. Catal., 345:45–65, 2003.

[24] O. Schwalm, B. Minder, J. Weber, and A. Baiker. Enantioselective hydrogenation of α-ketoester over Pt/alumina modified with cinchonidine: theoretical investigation of the substrate-modifier interaction. Catal. Lett., 23:271–279, 1994.

[25] G. A. Attard. Electrochemical Studies of Enantioselectivity at Chiral Metal Surfaces. J. Phys. Chem. B, 105:3158–3167, 2001.

[26] R. M. Hazen and D. S. Sholl. Chiral selection on inorganic crystalline surfaces. Nature Mat., 2:367–374, 2003.

[27] W. A. Bonner, P. R. Kavasmaneck, F. S. Martin, and J. T. Flores. Asymmetric Adsorption of Alanine by Quartz. Science, 186:143–144, 1974.

[28] G.-M. Schwab, F. Rost, and L. Rudolph. Optisch asymmetrische katalyse an quarzkristallen. Kolloid-Zeitschrift, 68:157–165, 1934.

[29] A. Baiker. Reflections on chiral metal surfaces and their potential for catalysis. Catal. Today, 100:159–170, 2005.

[30] M.-Y. Yin, G.-L. Yuan, M.-Y. Huang, and Y.-Y. Jiang. Catalytic behaviour of a Wool-Pd complex in asymmetric hydrogenation of diacetone alcohol and 3-methyl-2-butanone. J. Mol. Catal. A, 147:89–92, 1999.

[31] C. F. McFadden, P. S. Cremer, and A. J. Gellman. Adsorption of Chiral Alcohols on Chiral Metal Surfaces. Langmuir, 12:2483–2487, 1996.

[32] D. S. Sholl, A. Asthagiri, and T. D. Power. Naturally Chiral Metal Surfaces as Enantiospecific Adsorbents. J. Phys. Chem. B, 105:4771–4782, 2001.

[33] J. D. Horvath and A. J. Gellman. Enantiospecific Desorption of *R*- and *S*-Propylene Oxide from a Chiral Cu(643) Surface. J. Am. Chem. Soc., 123:7953–7954, 2001.

[34] J. D. Horvath and A. J. Gellman. Enantiospecific Desorption of Chiral Compounds from Chiral Cu(643) and Achiral Cu(111) Surface. J. Am. Chem. Soc., 124:2384–2392, 2002.

[35] J. D. Horvath and A. J. Gellman. Naturally chiral surfaces. Topics Catal., 25:9–15, 2003.

[36] A. Ahmadi and G. Attard. Surface Reactivity at Chiral Platinum Surfaces. Langmuir, 15:2420–2424, 1999.

[37] R. Raval, C. J. Baddeley, S. Haq, S. Louafi, P. Murray, C. Muryn, M. Ortega Lorenzo, and J. Williams. Complexities and Dynamics of the Enantioselective Active Site in Heterogeneous Catalysis. Reaction Kinetics and the Developement of Catalytic Processes, pages 11–21, 1999.

[38] K.-H. Ernst. Aspects of Molecular Chirality at Metal Surfaces. Z. Phys. Chem., 223:37–51, 2009.

[39] K.-H. Ernst. Supramolecular Surface Chirality. Top. Curr. Chem., 265:209–252, 2006.

[40] S. M. Barlow and R. Raval. Complex organic molecules at metal surfaces: bonding, organisation and chirality. Surf. Sci. Rep., 50:201–341, 2003.

[41] R. Raval. Chiral expression at metal surfaces. Current Opinion in Solid State and Materials Science, 7:67–74, 2003.

[42] V. Humblot, S. M. Barlow, and R. Raval. Two-dimensional organisational chirality through supramolecular assembly of molecules at metal surfaces. Progress in Surface Science, 76:1–19, 2004.

[43] G. Ertl and J. Küppers. Low Energy Electrons and Surface Chemistry. VCH Verlagsgesellschaft, 1985.

[44] L. Merz and K.-H. Ernst. Unification of the matrix notation in molecular surface science. Surf. Sci., 604(15):1049–1054, 2010.

[45] M. Ortega Lorenzo, S. Haq, T. Bertrams, P. Murray, R. Raval, and C. J. Baddeley. Creating Chiral Surfaces for Enantioselective Heterogeneous Catalysis: *R,R*-Tartaric Acid on Cu(110). J. Phys. Chem. B, 103:10661–10669, 1999.

[46] R. Raval. Creating chiral architectures at metal surfaces. J. Phys.: Condens. Matter, 14:4119–4132, 2002.

[47] M. Ortega Lorenzo, V. Humblot, P. Murray, C. J. Baddeley, S. Haq, and R. Raval. Chemical Transformations, Molecular Transport, and Kinetic Barriers in Creating the Chiral Phase of (*R,R*)-Tartaric Acid on Cu(110). J. Catal., 205:123–134, 2002.

[48] M. Ortega Lorenzo, C. J. Baddeley, C. Muryn, and R. Raval. Extended surface chirality from supramolecular assemblies of adsorbed chiral molecules. NATURE, 404:376–379, 2000.

[49] T. E. Jones and C. J. Baddeley. A RAIRS, STM and TPD study of the Ni(111) / *R,R*-tartaric acid system: Modelling the chiral modification of Ni nanoparticles. Surf. Sci., 513:453–467, 2002.

[50] A. M. Lakhani, D. J. DeWitt, N. M. Sant'Agata, and T. P. Pearl. Persistence of Chirality for a Weakly Bound Adsorbate: (*R,R*)- and (*S,S*)-Tartaric Acid/Ag(111). J. Phys. Chem. C, 111:5750–5755, 2007.

[51] V. H. Humblot, S. Haq, C. Muryn, W. A. Hofer, and R. Raval. From Local Adsorption Stresses to Chiral Surfaces: *R,R*-Tartaric Acid on Ni(110). J. Am. Chem. Soc., 124:503–510, 2002.

[52] W. A. Hofer, V. Humblot, and R. Raval. Conveying chirality onto the electronic structure of achiral metals: (*R,R*)-tartaric acid on nickel. Surf. Sci., 554:141–149, 2004.

[53] T. E. Jones, T. C. Noakes, P. Bailey, and C. J. Baddeley. Adsorbate-Induced Segregation in the Ni(111)/Au/(*R,R*)-Tartaric Acid System. J. Phys. Chem. B, 108:4759–4766, 2004.

[54] T. E. Jones and C. J. Baddeley. An investigation of the adsorption of (*R,R*)-tartaric acid on oxidised Ni(111) surfaces. J. Mol. Catal. A: Chemical, 216:223–231, 2004.

[55] R. Fasel, J. Wider, C. Quitmann, K.-H. Ernst, and T. Greber. Determination of the Absolute Chirality of Adsorbed Molecules. Angew. Chem. Int. Ed., 43:2853–2856, 2004.

[56] L. A. M. M. Barbosa and P. Sautet. Stability of Chiral Domains Produced by Adsorption of Tartaric Acid Isomers on the Cu(110) Surface: A Periodic Density Functional Theory Study. J. Am. Chem. Soc., 123:6639–6648, 2001.

[57] C. G. M. Hermse, A. P. van Bavel, A. P. J. Jansen, L. A. M. M. Barbosa, P. Sautet, and R. A. van Santen. Formation of Chiral Domains for Tartaric Acid on Cu(110): A Combined DFT and Kinetic Monte Carlo Study. J. Phys. Chem. B, 108:11035–11043, 2004.

[58] T. B. Grimley. The indirect interaction between adatoms or molecules adsorbed on metals. Proc. Phys. Soc., 90:751–764, 1967.

[59] T. B. Grimley. The electron density in a metal near a chemisorbed atom or molecule. Proc. Phys. Soc., 92:776–782, 1967.

[60] G. Jones, L. B. Jones, F. Thibault-Starzyk, E. A. Seddon, R. Raval, S. J. Jenkins, and G. Held. The local adsorption geometry and electronic structure of alanine on Cu(110). Surf. Sci., 600:1924–1935, 2006.

[61] S. Barlow, S. Louafi, D. Le Roux, J. Williams, C. Muryn, S. Haq, and R. Raval. Polymorphism in supramolecular chiral structures of *R*- and *S*-alanine on Cu(110). Surf. Sci., 590:243–263, 2005.

[62] N. A. Booth, D. P. Woodruff, O. Schaff, T. Giessel, R. Lindsay, P. Baumgärtel, and A. M. Bradshaw. Determination of the local structure of glycine adsorbed on Cu(110). Surf. Sci., 397:258–269, 1998.

[63] S. Blankenburg and W. G. Schmidt. Steric effects and chirality in the adsorption of glycine and phenylglycine on Cu(110). Nanotechnology, 18:1–5, 2007.

[64] D. P. Woodruff, C. F. McConville, and A. L. D. Kilcoyne. The Structure Of The Formate Species On Copper Surfaces: New Photoelectron Diffraction Results And SEXAFS Data Reassessed. Surf. Sci., 201:228–244, 1988.

[65] S. Poulston, R. A. Bennett, A. H. Jones, and M. Bowker. STM study of formic acid adsorption on Cu(110). Phys. Rev. B, 55:12888–12891, 1997.

[66] J. R. B. Gomes and J. A. N. F. Gomes. Adsorption of the formate species on copper surfaces: a DFT study. Surf. Sci., 432:279–290, 1999.

[67] O. Karis, J. Hasselström, N. Wassdahl, M. Weinelt, A. Nilsson, M. Nyberg, L. G. M. Petterson, J. Stöhr, and M. G. Samant. The bonding of simple carboxylic acids on Cu(110). J. Chem. Phys., 112:8146–8155, 2000.

[68] S. M. York, S. Haq, K. V. Kilway, J. M. Phillips, and F. M. Leibsle. STM, FTIR and quantum chemical calculation studies of acetate structures on Cu(110) surfaces. Surf. Sci., 522:34–46, 2003.

[69] M. Forster, M. S. Dyer, M. Persson, and R. Raval. Probing Conformers and Adsorption Footprints at the Single-Molecule Level in a Highly Organized Amino Acid Assembly of (*S*)-Proline on Cu(110). J. Am. Chem. Soc., 131:10173–10181, 2009.

[70] M. Forster, M. S. Dyer, M. Persson, and R. Raval. 2D Random Organization of Racemic Amino Acid Monolayers Driven by Nanoscale Adsorption Footprints: Proline on Cu(110). Angew. Chem. Int. Ed., 49:2344–2348, 2010.

[71] B. Behzadi, S. Romer, R. Fasel, and K.-H. Ernst. Chiral Recognition in Surface Explosion. J. Am. Chem. Soc., 126:9176–9177, 2004.

[72] S. Romer, B. Behzadi, R. Fasel, and K.-H. Ernst. Homochiral Conglomerates and Racemic Crystals in Two Dimensions: Tartaric Acid on Cu(110). Chem. Eur. J., 11:4149–4154, 2005.

[73] M. Parschau, B. Behzadi, S. Romer, and K.-H. Ernst. Stereoisomeric influence on 2D lattice structure: achiral *meso*-tartaric acid *versus* chiral tartaric acid. Surf. Interface Anal., 38:1607–1610, 2006.

[74] M. Parschau, T. Kampen, and K.-H. Ernst. Homochirality in monolayers of achiral meso tartaric acid. Chem. Phys. Lett., 407:433–437, 2005.

[75] V. Humblot, M. Ortega Lorenzo, C. J. Baddeley, S. Haq, and R. Raval. Local and Global Chirality at Surfaces: Succinic Acid versus Tartaric Acid on Cu(110). J. Am. Chem. Soc., 126:6460–6469, 2004.

[76] V. Humblot and R. Raval. Chiral metal surfaces from the adsorption of chiral and achiral molecules. Applied Surface Science, 241:150–156, 2005.

[77] N. Liu, S. Haq, G. R. Darling, and R. Raval. Direct Visualization of Enantiospecific Substitution of Chiral Guest Molecules into Heterochiral Molecular Assemblies at Surfaces. Angew. Chem. Int. Ed., 46:7613–7616, 2007.

[78] M. Parschau, S. Romer, and K.-H. Ernst. Induction of Homochirality in Achiral Enantimorphous Monolayers. J. Am. Chem. Soc., 126:15398–15399, 2004.

[79] K.-H. Ernst. Amplification of chirality in two-dimensional molecular lattices. Current Opinion in Colloid & Interface Science, 13:54–59, 2008.

[80] M. M. Green and M. P. Reidy. Macromolecular Stereochemistry: The Out-of-Proportion Influence of Optically Active Comonomers on the Conformational Characteristics of Polyisocyanates. The Sergeants and Soldiers Experiment. J. Am. Chem. Soc., 111:6452–6454, 1989.

[81] M. M. Green, J.-W. Park, T. Sato, A. Teramoto, S. Lifson, R. L. B. Selinger, and J. V. Selinger. The Macromolecular Route to Chiral Amplification. Angew. Chem. Int. Ed., 38:3138–3154, 1999.

[82] J. V. Selinger and R. L. B. Selinger. Cooperative chiral order in copolymers of chiral and achiral units. Phys. Rev. E, 55:1728–1731, 1997.

[83] S. Haq, N. Liu, V. Humblot, A. P. J. Jansen, and R. Raval. Drastic symmetry breaking in supramolecular organization of enantiomerically unbalanced monolayers at surfaces. Nature Chemistry, 1:409–414, 2009.

[84] W. B. Jensen. The Origin of the Names Malic Acid, Maleic, and Malonic Acid. J. Chem. Ed., 84:924, 2007.

[85] G. J. Bremer. Vorläufige Mitteilung über eine neue Äpfelsäure, welche die Polarisationsebene rechts dreht. Ber. d. Deutsch. Chem. Ges., 8:861–863, 1875.

[86] http://en.wikipedia.org/wiki/malic_acid.

[87] T. Fliessbach. Quantummechanik. Spektrum Akademischer Verlag, 2000.

[88] K.Christmann. Introduction to Surface Physical Chemistry. Steinkopff Verlag, 1991.

[89] A. Zangwill. Physics at Surfaces. Cambridge University Press, 1988.

[90] C. D. Wagner, W. M. Riggs, L. E. Davis, J. F. Moulder, and G. E. Muilenberg. Handbook of X-Ray Photoelectron Spectroscopy. Perkin-Elmer Corporation, 1979.

[91] A. Klein, T. Mayer, A. Thissen, and W. Jaegermann. Photoelectron Spectroscopy in Materials Science and Physical Chemistry. BUNSEN-MAGAZIN, 4:124–139, 2008.

[92] C. Davisson and L. H. Germer. Diffraction of Electrons by a Crystal of Nickel. Phys. Rev., 30(6):705–740, 1927.

[93] L. R. Apker. Surface Phenomena Useful in Vacuum Technique. Ind. Eng. Chem., 40(5):846–847, 1948.

[94] P. A. Redhead. Thermal Desorption of Gases. Vacuum, 12:203–211, 1962.

[95] F. M. Lord and J. S. Kittelberger. On the Determination of Activation Energies in Thermal Desorption Experiments. Surf. Sci., 43:173–182, 1974.

[96] D. A. King. Thermal Desorption From Metal Surfaces: A Review. Surf. Sci., 47:384–402, 1975.

[97] D. L. Adams. Consequences of Adsorbate-Adsorbate Interactions For Thermal Desorption And LEED Measurements. Surf. Sci., 42:12–36, 1974.

[98] C. G. Goymour and D. A. King. Chemisorption of Carbon Monoxide on Tungsten. J. Chem. Soc., Faraday Trans. 1, 69:749–760, 1973.

[99] R. G. Sharpe and M. Bowker. Kinetic models of surface explosion. J. Phys.: Condens. Matter, 7:6379–6392, 1995.

[100] G. Binning, H. Rohrer, Ch. Gerber, and E. Weibel. Tunneling through a controllable vacuum gap. Appl. Phys. Lett., 40(2):178–180, 1982.

[101] G. Binning, H. Rohrer, Ch. Gerber, and E. Weibel. Surface Studies by Scanning Tunneling Microscopy. Phys. Rev. Lett., 49(1):57–61, 1982.

[102] J. H. Davies. The Physics of Low-Dimensional Semiconductors. Cambridge University Press, 1998.

[103] J. Tersoff and D. R. Hamann. Theory of the scanning tunneling microscope. Phys. Rev. B, 31(2):805–813, 1985.

[104] W. Demtröder. Experimentalphysik 3. Springer Verlag, 2004.

[105] J. Weidlein, U. Müller, and K. Dehnicke. Schwingungsspektroskopie. Thieme, 1988.

[106] R. G. Greenler. Infrared Study of Adsorbed Molecules on Metal Surfaces by Reflection Techniques. J. Chem. Phys., 44(1):310–315, 1966.

[107] F. M. Hoffmann. Infrared Reflection-Absorption Spectroscopy of Adsorbed Molecules. Surf. Sci. Rep., 3:107–192, 1983.

[108] R. G. Greenler, D. R. Snider, D. Witt, and R. S. Sorbello. The Metal-Surface Selection Rule For Infrared Spectra Of Molecules Adsorbed On Small Metal Particles. Surf. Sci., 118:415–428, 1982.

[109] H. Pearce and N. Sheppard. Possible Importance of A Metal-Surface Selection Rule in The Interpretation of The Infrared Spectra of Molecules Adsorbed on Particulate Metals. Surf. Sci., 59:205–217, 1976.

[110] G. Rupprechter. Sum Frequency Generation and Polarization-Modulation Infrared Reflection Absorption Spectroscopy of Functioning Model Catalysts from Ultrahigh Vacuum to Ambient Pressure. Adv. Catal., 51:133–263, 2007.

[111] E. L. Wislon and W. A. Brown. Low Pressure RAIRS Studies of Model Catalytic Systems. J. Phys. Chem. C, 114:6879–6893, 2010.

[112] J. VandeVondele, M. Krack, F. Mohamed, M. Parinello, T. Chassaing, and J. Hutter. Fast and accurate density functional calculations using a mixed gaussian and plane waves approach. Compt. Phys. Commun., 167:103–128, 2005.

[113] S. Godecker, M. Teter, and J. Hutter. Separable dual-space gaussian pseudopotentials. Phys. Rev. B, 54:1703–1710, 1996.

[114] J. VandeVondele and J. Hutter. Gaussian basis sets for accurate calculations on molecular systems in gas and condensed phases. J. Chem. Phys., 127:114105–1–114105–10, 2007.

[115] C. Roth, D. Passerone, L. Merz, M. Parschau, and K.-H. Ernst. Two-dimensional self-assembly of chiral malic acid on Cu(110). J. Phys. Chem. C (in press: doi: 10.1021/jp106575g).

[116] M. Bowker and R. Madix. XPS, UPS and thermal desorption studies of the reactions of formaldehyde and formic acid with the Cu(110) surface. Surf. Sci., 102:542–565, 1981.

[117] M. Bowker and R. Madix. XPS, UPS and thermal desorption studies of the adsorption and reactions of $CH_3CHO$and CH_3COOH with the Cu(110) surface. Vacuum, 31:711–714, 1981.

[118] K. Uvdahl, P. Bodö, A. Ihs, B. Liedberg, and W. Salaneck. X-Ray Photoelectron and Infrared Spectroscopy of Glycin Adsorbed upon Copper. Journal of Colloid and Interface Science, 140:207–215, 1990.

[119] K. Uvdahl, P. Bodö, and B. Liedberg. L-cystein adsorbed on gold and copper: An x-ray photoelectron spectroscopy study. Journal of Colloid and Interface Science, 149:162–173, 1992.

[120] K. Kimura, S. Katsumata, Y. Achiba, T. Yamazaki, and S. Iwata. Handbook of HeI Photoelectron Spectra of Fundamental Organic Molecules. Halsted Press, 1981.

[121] W. L. Jorgensen and L. Salem. The Organic Chemists's Book of Orbitals. Academic Press, 1973.

[122] M. Bowker and R. Madix. The adsorption and oxidation of acetic acid and acetaldehyde on Cu(110). Appl. Surf. Sci., 8:299–317, 1981.

[123] J. V. Barth. Molecular Architectonic on Metal Surfaces. Annu. Rev. Phys. Chem., 58:375–407, 2007.

[124] Xueying Zhao. Fabricating Homochiral Facets on Cu(001) with *L*-lysine. J. Am. Chem. Soc., 122:12584–12585, 2000.

[125] G. Socrates. Infrared Characteristic Group Frequencies. John Wiley & Sons Ltd., 1994.

[126] J. McCarty, J. Falconer, and R. J. Madix. Decomposition of Formic Acid on Ni(110). J. Catal., 30:235–249, 1973.

[127] J. Falconer and R. J. Madix. The Kinetics and Mechanism of the Autocatalytic Decomposition of HCOOH on Clean Ni(110). Surf. Sci., 46:473–504, 1974.

[128] R. J. Madix, J. L. Falconer, and A. M. Suszko. The Autocatalytic Decomposition of Acetic Acid on Ni(110). Surf. Sci., 54:6–20, 1976.

[129] Y. Li and M. Bowker. Acetate formation, stabilisation and surface explosion on Rh(111). Surf. Sci., 285:219–226, 1993.

[130] Y. Li and M. Bowker. Acetic Acid on Rh(110): The Stabilisation and Autocatalytic Decomposition of Acetate. J. Catal., 142:630–640, 1993.

[131] N. Aas and M. Bowker. Adsorption and Autocatalytic Decomposition of Acetic Acid on Pd(110). J. Chem. Soc., Faraday Trans. 1, 89:1249–1255, 1993.

[132] M. Bowker, C. Morgan, and J. Couves. Acetic acid adsorption and decomposition on Pd(110). Surf. Sci., 555:145–156, 2004.

[133] P. J. Feibelman. Anisotropy of the stress on fcc(110) surfaces. Phys. Rev. B, 51:17867–17875, 1995.

[134] M. Blanco-Rey and G. Jones. Asymmetric relief of surface stress induced by a chiral adsorbate: Alaninate adsorption on Cu(110). Phys. Rev. B, 81:205428–1–205428–7, 2010.

[135] R. Fasel, M. Parschau, and K.-H. Ernst. Amplification of chirality in two-dimensional enantiomorphous lattices. NATURE, 439:449–452, 2006.

[136] G. Wedler. Lehrbuch der Physikalischen Chemie. Verlag Chemie, 1982.